

DarkSide-20k Intermediate Design Report

C. E. Aalseth,¹ S. Abdelhakim,² F. Acerbi,^{3,4} P. Agnes,⁵ I. F. M. Albuquerque,⁶
 T. Alexander,¹ A. Alici,^{7,8} A. K. Alton,⁹ P. Amaudruz,¹⁰ F. Ameli,¹¹ P. Antonioli,⁸
 S. Arcelli,^{7,8} R. Ardito,^{12,13} I. J. Arnquist,¹ P. Arpaia,^{14,15} D. M. Asner,¹⁶ A. Asunskis,¹⁷
 M. Ave,⁶ H. O. Back,¹ A. Barrado Olmedo,¹⁸ G. Batignani,^{19,20} M. G. Bisogni,^{19,20} V. Bocci,¹¹
 A. Bondar,^{21,22} G. Bonfini,²³ W. Bonivento,²⁴ B. Bottino,^{25,26} M. G. Boulay,²⁷ R. Bunker,¹
 S. Bussino,^{28,29} A. Buzulutskov,^{21,22} M. Cadeddu,^{30,24} M. Cadoni,^{30,24} A. Caminata,²⁶
 N. Canci,^{5,23} A. Candela,²³ C. Cantini,³¹ M. Caravati,²⁴ M. Cariello,²⁶ M. Carpinelli,^{32,33}
 A. Castellani,^{12,13} P. Castello,^{34,24} S. Catalanotti,^{35,15} V. Cataudella,^{35,15} P. Cavalcante,^{36,23}
 S. Cavuoti,^{35,15} S. Cebrian,³⁷ B. Celano,¹⁵ R. Cereseto,²⁶ W. Cheng,^{38,39} A. Chepurnov,⁴⁰
 C. Ciccalò,²⁴ L. Cifarelli,^{7,8} M. Citterio,¹³ A. G. Cocco,¹⁵ M. Colocci,^{7,8} L. Consiglio,⁴¹
 F. Cossio,^{38,39} G. Covone,^{35,15} P. Crivelli,³¹ I. D'Antone,⁸ M. D'Incecco,²³ D. D'Urso,^{32,33}
 M. D. Da Rocha Rolo,³⁸ M. Daniel,¹⁸ S. Davini,²⁶ A. De Candia,^{35,15} S. De Cecco,^{11,42}
 M. De Deo,²³ A. De Falco,^{24,30} G. De Filippis,^{35,15} D. De Gruttola,⁴³ G. De Guido,^{44,13}
 G. De Rosa,^{35,15} G. Dellacasa,³⁸ P. Demontis,^{32,33,45} S. DePaquale,⁴³ A. V. Derbin,⁴⁶
 A. Devoto,^{30,24} F. Di Eusanio,^{47,23} G. Di Pietro,^{23,13} P. Di Stefano,⁴⁸ C. Dionisi,^{11,42}
 F. Dordei,²⁴ M. Downing,⁴⁹ F. Edalatfar,¹⁰ A. Empl,⁵ M. Fernandez Diaz,¹⁸ A. Ferri,^{3,4}
 C. Filip,⁵⁰ G. Fiorillo,^{35,15} K. Fomenko,⁵¹ A. Franceschi,⁵² D. Franco,⁵³ G. E. Froudakis,⁵⁴
 F. Gabriele,²³ A. Gabrieli,^{32,33} C. Galbiati,^{47,41} P. Garcia Abia,¹⁸ D. Gascón Fora,⁵⁵
 A. Gendotti,³¹ C. Ghiano,²³ A. Ghisi,^{12,13} S. Giagu,^{11,42} P. Giampa,¹⁰ R. A. Giampaolo,³⁸
 C. Giganti,⁵⁶ M. A. Giorgi,^{20,19} G. K. Giovanetti,⁴⁷ M. L. Gligan,⁵⁰ A. Gola,^{3,4} O. Gorchakov,⁵¹
 M. Grab,⁵⁷ R. Graciani Diaz,⁵⁵ F. Granato,⁵⁸ M. Grassi,¹⁹ J. W. Grate,¹ G. Y. Grigoriev,⁵⁹
 A. Grobov,⁵⁹ M. Gromov,⁴⁰ M. Guan,⁶⁰ M. B. B. Guerra,¹⁷ M. Guerzoni,⁸ M. Gulino,^{61,33}
 R. K. Haaland,⁶² B. R. Hackett,⁶³ A. Hallin,⁶⁴ B. Harrop,⁴⁷ E. W. Hoppe,¹ S. Horikawa,^{41,23}
 B. Hosseini,²⁴ F. Hubaut,⁶⁵ P. Humble,¹ E. V. Hungerford,⁵ An. Ianni,^{47,23} V. Ippolito,¹¹
 C. Jillings,^{66,67} S. Jimenez Cabre,¹⁸ K. Keeter,¹⁷ C. L. Kendziora,⁶⁸ S. Kim,⁵⁸ I. Kochanek,²³
 K. Kondo,⁴¹ G. Kopp,⁴⁷ D. Korablev,⁵¹ G. Korga,^{5,23} A. Kubankin,⁶⁹ R. Kugathasan,^{38,39}
 M. Kuss,¹⁹ M. Kuzniak,²⁷ M. La Commara,^{70,15} M. Lai,^{30,24} S. Langrock,^{66,67} M. Lebois,²
 B. Lehnert,⁶⁴ X. Li,⁴⁷ Q. Liqiang,² M. Lissia,²⁴ G. U. Lodi,^{44,13} G. Longo,^{35,15} R. Lussana,^{71,13}
 L. Luzzi,^{72,13} A. A. Machado,⁷³ I. N. Machulin,^{59,74} A. Mandarano,^{41,23} L. Mapelli,⁴⁷
 M. Marcante,^{75,4,3} A. Margotti,⁸ S. M. Mari,^{28,29} M. Mariani,^{72,13} J. Maricic,⁶³ M. Marinelli,^{25,26}
 D. Marras,²⁴ A. D. Martinez Rojas,^{38,39} C. J. Martoff,⁵⁸ M. Mascia,^{76,24} A. Masoni,²⁴
 A. Mazzi,^{3,4} A. B. McDonald,⁴⁸ A. Messina,^{11,42} P. D. Meyers,⁴⁷ T. Miletic,⁶³ R. Milincic,⁶³
 A. Moggi,¹⁹ S. Moioli,^{44,13} J. Monroe,⁷⁷ M. Morrocchi,¹⁹ T. Mroz,⁵⁷ W. Mu,³¹ V. N. Muratova,⁴⁶
 S. Murphy,³¹ C. Muscas,^{34,24} P. Musico,²⁶ R. Nania,⁸ T. Napolitano,⁵² A. Navrer Agasson,⁵⁶
 M. Nessi,⁷⁸ I. Nikulin,⁶⁹ A. O. Nozdrina,^{59,74} N. N. Nurakhov,⁵⁹ A. Oleinik,⁶⁹ V. Oleynikov,^{21,22}
 M. Orsini,²³ F. Ortica,^{79,80} L. Pagani,⁸¹ M. Pallavicini,^{25,26} S. Palmas,^{76,24} L. Pandola,³³
 E. Pantic,⁸¹ E. Paoloni,^{19,20} G. Paternoster,^{3,4} V. Pavletcov,⁴⁰ F. Pazzona,^{32,33} S. Peeters,⁸²
 P. A. Pegoraro,^{34,24} K. Pelczar,²³ L. A. Pellegrini,^{44,13} N. Pelliccia,^{79,80} F. Perotti,^{12,13}
 V. Pesudo,¹⁸ E. Picciau,^{30,24} C. Piemonte,^{3,4} F. Pietropaolo,⁷⁸ A. Pocar,⁴⁹ T. Pollman,⁸³
 D. Portaluppi,^{71,13} S. S. Poudel,⁵ P. Pralavorio,⁶⁵ D. Price,⁸⁴ D. A. Pugachev,⁵⁹ B. Radics,³¹
 F. Raffaelli,¹⁹ F. Ragusa,^{85,13} M. Razeti,²⁴ A. Razeto,²³ V. Regazzoni,^{75,4,3} C. Regenfus,³¹
 A. L. Renshaw,⁵ S. Rescia,¹⁶ M. Rescigno,¹¹ F. Retiere,¹⁰ Q. Riffard,⁵³ A. Rivetti,³⁸
 A. Romani,^{79,80} L. Romero,¹⁸ N. Rossi,^{11,23} A. Rubbia,³¹ D. Sablone,^{58,23} P. Sala,⁷⁸
 P. Salatino,^{86,15} O. Samoylov,⁵¹ E. Sánchez García,¹⁸ S. Sanfilippo,^{29,28} M. Sant,^{32,33}
 D. Santone,⁷⁷ R. Santorelli,¹⁸ C. Savarese,⁴⁷ E. Scapparone,⁸ B. Schlitzer,⁸¹ G. Scioli,^{7,8}
 E. Segreto,⁷³ A. Seifert,¹ D. A. Semenov,⁴⁶ A. Shchagin,⁶⁹ E. Shemyakina,^{21,22} A. Sheshukov,⁵¹
 S. Siddhanta,²⁴ M. Simeone,^{86,15} P. N. Singh,⁵ P. Skensved,⁴⁸ M. D. Skorokhvatov,^{59,74}

- 52 O. Smirnov,⁵¹ G. Sobrero,²⁶ A. Sokolov,^{21,22} A. Sotnikov,⁵¹ R. Stainforth,²⁷ S. Stracka,¹⁹
 53 G. B. Suffritti,^{32,33,45} S. Sulis,^{34,24} Y. Suvorov,^{35,15,59} A.M. Szlc,⁸⁴ R. Tartaglia,²³
 54 G. Testera,²⁶ T. Thorpe,^{41,23} A. Tonazzo,⁵³ A. Tosi,^{71,13} E. V. Unzhakov,⁴⁶ G. Usai,^{24,30}
 55 A. Vacca,^{76,24} E. Vázquez-Jáuregui,⁸⁷ M. Verducci,^{11,42} T. Viant,³¹ S. Viel,²⁷
 56 F. Villa,^{71,13} A. Vishneva,⁵¹ R. B. Vogelaar,³⁶ M. Wada,²⁴ J. Wahl,¹ J. J. Walding,⁷⁷
 57 H. Wang,⁸⁸ Y. Wang,⁸⁸ S. Westerdale,²⁷ R. J. Wheadon,³⁸ R. Williams,¹ J. Wilson,²
 58 Marcin Wojcik,⁵⁷ Mariusz Wojcik,⁸⁹ S. Wu,³¹ X. Xiao,⁸⁸ C. Yang,⁶⁰ Z. Ye,⁵ and G. Zuzel⁵⁷
 59
 60 ¹Pacific Northwest National Laboratory, Richland, WA 99352, USA
 61 ²Institut de Physique Nucléaire d'Orsay, 91406, Orsay, France
 62 ³Fondazione Bruno Kessler, Povo 38123, Italy
 63 ⁴Trento Institute for Fundamental Physics and Applications, Povo 38123, Italy
 64 ⁵Department of Physics, University of Houston, Houston, TX 77204, USA
 65 ⁶Instituto de Física, Universidade de São Paulo, São Paulo 05508-090, Brazil
 66 ⁷Physics Department, Università degli Studi di Bologna, Bologna 40126, Italy
 67 ⁸INFN Bologna, Bologna 40126, Italy
 68 ⁹Physics Department, Augustana University, Sioux Falls, SD 57197, USA
 69 ¹⁰TRIUMF, 4004 Wesbrook Mall, Vancouver, BC V6T 2A3, Canada
 70 ¹¹INFN Sezione di Roma, Roma 00185, Italy
 71 ¹²Civil and Environmental Engineering Department, Politecnico di Milano, Milano 20133, Italy
 72 ¹³INFN Milano, Milano 20133, Italy
 73 ¹⁴Department of Electrical Engineering and Information Technology,
 74 Università degli Studi "Federico II" di Napoli, Napoli 80125, Italy
 75 ¹⁵INFN Napoli, Napoli 80126, Italy
 76 ¹⁶Brookhaven National Laboratory, Upton, NY 11973, USA
 77 ¹⁷School of Natural Sciences, Black Hills State University, Spearfish, SD 57799, USA
 78 ¹⁸CIEMAT, Centro de Investigaciones Energéticas, Medioambientales y Tecnológicas, Madrid 28040, Spain
 79 ¹⁹INFN Pisa, Pisa 56127, Italy
 80 ²⁰Physics Department, Università degli Studi di Pisa, Pisa 56127, Italy
 81 ²¹Budker Institute of Nuclear Physics, Novosibirsk 630090, Russia
 82 ²²Novosibirsk State University, Novosibirsk 630090, Russia
 83 ²³INFN Laboratori Nazionali del Gran Sasso, Assergi (AQ) 67100, Italy
 84 ²⁴INFN Cagliari, Cagliari 09042, Italy
 85 ²⁵Physics Department, Università degli Studi di Genova, Genova 16146, Italy
 86 ²⁶INFN Genova, Genova 16146, Italy
 87 ²⁷Department of Physics, Carleton University, Ottawa, ON K1S 5B6, Canada
 88 ²⁸INFN Roma Tre, Roma 00146, Italy
 89 ²⁹Mathematics and Physics Department, Università degli Studi Roma Tre, Roma 00146, Italy
 90 ³⁰Physics Department, Università degli Studi di Cagliari, Cagliari 09042, Italy
 91 ³¹Institute for Particle Physics, ETH Zürich, Zürich 8093, Switzerland
 92 ³²Chemistry and Pharmacy Department, Università degli Studi di Sassari, Sassari 07100, Italy
 93 ³³INFN Laboratori Nazionali del Sud, Catania 95123, Italy
 94 ³⁴Department of Electrical and Electronic Engineering
 95 Engineering, Università degli Studi, Cagliari 09042, Italy
 96 ³⁵Physics Department, Università degli Studi "Federico II" di Napoli, Napoli 80126, Italy
 97 ³⁶Virginia Tech, Blacksburg, VA 24061, USA
 98 ³⁷Laboratorio de Física Nuclear y Astropartículas, Universidad de Zaragoza, Zaragoza 50009, Spain
 99 ³⁸INFN Torino, Torino 10125, Italy
 100 ³⁹Department of Electronics and Communications, Politecnico di Torino, Torino 10129, Italy
 101 ⁴⁰Skobeltsyn Institute of Nuclear Physics, Lomonosov Moscow State University, Moscow 119234, Russia
 102 ⁴¹Gran Sasso Science Institute, L'Aquila 67100, Italy
 103 ⁴²Physics Department, Sapienza Università di Roma, Roma 00185, Italy
 104 ⁴³INFN Salerno, Salerno 84084, Italy
 105 ⁴⁴Chemistry, Materials and Chemical Engineering Department
 106 "G. Natta", Politecnico di Milano, Milano 20133, Italy
 107 ⁴⁵Interuniversity Consortium for Science and Technology of Materials, Firenze 50121, Italy
 108 ⁴⁶Saint Petersburg Nuclear Physics Institute, Gatchina 188350, Russia
⁴⁷Physics Department, Princeton University, Princeton, NJ 08544, USA

- 109 ⁴⁸*Department of Physics, Engineering Physics and Astronomy,
 110 Queen's University, Kingston, ON K7L 3N6, Canada*
 111 ⁴⁹*Amherst Center for Fundamental Interactions and Physics
 112 Department, University of Massachusetts, Amherst, MA 01003, USA*
 113 ⁵⁰*National Institute for R&D of Isotopic and Molecular Technologies, Cluj-Napoca, 400293, Romania*
 114 ⁵¹*Joint Institute for Nuclear Research, Dubna 141980, Russia*
 115 ⁵²*INFN Laboratori Nazionali di Frascati, Frascati 00044, Italy*
 116 ⁵³*APC, Université Paris Diderot, CNRS/IN2P3, CEA/Irfu, Obs de Paris, USPC, Paris 75205, France*
 117 ⁵⁴*Department of Chemistry, University of Crete, P.O. Box 2208, 71003 Heraklion, Crete, Greece*
 118 ⁵⁵*Universitat de Barcelona, Barcelona E-08028, Catalonia, Spain*
 119 ⁵⁶*LPNHE, CNRS/IN2P3, Sorbonne Université, Université Paris Diderot, Paris 75252, France*
 120 ⁵⁷*M. Smoluchowski Institute of Physics, Jagiellonian University, 30-348 Krakow, Poland*
 121 ⁵⁸*Physics Department, Temple University, Philadelphia, PA 19122, USA*
 122 ⁵⁹*National Research Centre Kurchatov Institute, Moscow 123182, Russia*
 123 ⁶⁰*Institute of High Energy Physics, Beijing 100049, China*
 124 ⁶¹*Engineering and Architecture Faculty, Università di Enna Kore, Enna 94100, Italy*
 125 ⁶²*Department of Physics and Engineering, Fort Lewis College, Durango, CO 81301, USA*
 126 ⁶³*Department of Physics and Astronomy, University of Hawai'i, Honolulu, HI 96822, USA*
 127 ⁶⁴*Department of Physics, University of Alberta, Edmonton, AB T6G 2R3, Canada*
 128 ⁶⁵*Centre de Physique des Particules de Marseille, Aix
 129 Marseille Univ, CNRS/IN2P3, CPPM, Marseille, France*
 130 ⁶⁶*Department of Physics and Astronomy, Laurentian University, Sudbury, ON P3E 2C6, Canada*
 131 ⁶⁷*SNOLAB, Lively, ON P3Y 1N2, Canada*
 132 ⁶⁸*Fermi National Accelerator Laboratory, Batavia, IL 60510, USA*
 133 ⁶⁹*Radiation Physics Laboratory, Belgorod National Research University, Belgorod 308007, Russia*
 134 ⁷⁰*Pharmacy Department, Università degli Studi "Federico II" di Napoli, Napoli 80131, Italy*
 135 ⁷¹*Electronics, Information, and Bioengineering Department, Politecnico di Milano, Milano 20133, Italy*
 136 ⁷²*Energy Department, Politecnico di Milano, Milano 20133, Italy*
 137 ⁷³*Physics Institute, Universidade Estadual de Campinas, Campinas 13083, Brazil*
 138 ⁷⁴*National Research Nuclear University MEPhI, Moscow 115409, Russia*
 139 ⁷⁵*Physics Department, Università degli Studi di Trento, Povo 38123, Italy*
 140 ⁷⁶*Department of Mechanical, Chemical, and Materials
 141 Engineering, Università degli Studi, Cagliari 09042, Italy*
 142 ⁷⁷*Department of Physics, Royal Holloway University of London, Egham TW20 0EX, UK*
 143 ⁷⁸*CERN, European Organization for Nuclear Research 1211 Geneve 23, Switzerland, CERN*
 144 ⁷⁹*Chemistry, Biology and Biotechnology Department, Università degli Studi di Perugia, Perugia 06123, Italy*
 145 ⁸⁰*INFN Perugia, Perugia 06123, Italy*
 146 ⁸¹*Department of Physics, University of California, Davis, CA 95616, USA*
 147 ⁸²*Physics and Astronomy, University of Sussex, Brighton BN1 9QH, UK*
 148 ⁸³*Physik Department, Technische Universität München, Munich 80333, Germany*
 149 ⁸⁴*The University of Manchester, Manchester M13 9PL, United Kingdom*
 150 ⁸⁵*Physics Department, Università degli Studi di Milano, Milano 20133, Italy*
 151 ⁸⁶*Chemical, Materials, and Industrial Production Engineering Department,
 152 Università degli Studi "Federico II" di Napoli, Napoli 80126, Italy*
 153 ⁸⁷*Instituto de Física, Universidad Nacional Autónoma de México (UNAM), México 01000, Mexico*
 154 ⁸⁸*Physics and Astronomy Department, University of California, Los Angeles, CA 90095, USA*
 155 ⁸⁹*Institute of Applied Radiation Chemistry, Lodz University of Technology, 93-590 Lodz, Poland*

CONTENTS

157	List of Figures	vi
158	List of Tables	vii
159	1. Organization	1
160	2. Physics Case	1
161	2.1. DarkSide-20k: The High-Mass Search Program	2
162	2.2. DarkSide-LowMass: The Low-Mass Search Program	4
163	2.3. Argo	5
164	2.4. Comparison with Xenon-Based Experiments and the “Neutrino Floor”	5
165	2.5. Completed R&D for DS-20kProgram	6
166	2.6. Ongoing R&D for DS-20kProgram	7
167	3. Organization	7
168	3.1. Specific Roles and Responsibilities	10
169	4. Project Overview	10
170	5. Photoelectronics	14
171	5.1. PhotoDetector Modules (PDM)	14
172	5.2. Signal Transmission	16
173	5.3. PDM Fabrication and Characterization	16
174	5.4. Motherboard Assembly	18
175	5.5. Mass Production	18
176	6. Inner Detector and Cryogenics System	19
177	6.1. DS-20k LAr TPC	19
178	6.2. Cryogenics	25
179	7. Material Assays	31
180	7.1. Radio-purity database	32
181	7.2. Managing Assay Capabilities	32
182	7.3. Radioactive budget	33
183	8. Calibration	34
184	8.1. Distributed Gas Sources	34
185	8.2. Gamma Sources	35
186	8.3. Neutron Sources	35
187	8.4. Guide Tube System	36
188	9. Veto Detector	37
189	9.1. Overall Design	37
190	9.2. Assembly	39
191	9.3. Background Rejection	39
192	10. Data Acquisition	42
193	10.1. General DAQ scheme	42
194	10.2. Digitizers	43
195	10.3. DAQ software	43
196	11. Computing	44

197	11.1. Computing systems and data workflow	44
198	11.2. Software Environment	45
199	11.3. Simulation	46
200	12. The ReD Experiment	46
201	13. DarkSide-Proto	49
202	13.1. Prototype Overview and Status	49
203	13.2. The DS-Proto TPC	51
204	13.3. Materials for DarkSide-Proto	53
205	13.4. Validation tests and operation	53
206	14. AAr Cryostat	53
207	15. Argon Procurement and Purification	57
208	15.1. Urania	57
209	15.2. Aria	61
210	15.3. DArT	65
211	16. Technical Design	65
212	16.1. Installation Space and Services Needed	66
213	16.2. Electrical Power for DS-20kOperation	66
214	16.3. Nitrogen Argon and Water Services for DS-20kOperation	67
215	16.4. Underground Argon Storage and Transport	67
216	16.5. IT Infrastructure	67
217	17. Validation	67
218	18. Installation and Commissioning	67
219	18.1. Cryostat Description and Construction	68
220	18.2. Metallic Structure	69
221	18.3. Cryogenic System	69
222	18.4. The Radon Free Clean Room	69
223	18.5. TPC and Veto Detector Assembly and Installation	70
224	18.6. DS-20kProposed Installation Sequence	70
225	19. Health, Safety and Environmental Issues	71
226	20. Radiation Protection Issues	72
227	21. Project Management	72
228	References	72

LIST OF FIGURES

230 1	Artist rendering of the DS-20k detectors	2
231 2	Current DM limits and sensitivities for future experiments.....	3
232 3	5 σ discovery potential of the leading future noble liquid dark matter searches.....	6
233 4	The organization structure of the GADMC and of the DarkSide project	8
234 5	Artist rendering of the DS-20k experiment in Hall C of LNGS	12
235 6	The first PDM and first motherboard resulting from the assembly of PDMs.....	15
236 7	Schematic of the transimpedance amplified and summing circuits	15
237 8	Variance of impedance of SiPMs quenching resistors	16
238 9	SiPM <i>I-V</i> curves and SNR	17
239 10	SNR of the SiPMs tiles of the first motherboard	19
240 11	Artist rendering of the PMMA vessel and the TPC	21
241 12	PDM patterning scheme	22
242 13	DS-20k PDM motherboard designs	22
243 14	3D model of the full DS-20k LAr TPC reflector panels system	23
244 15	DS-20k LAr TPC anode and cathode regions	24
245 16	Simulated electric field mapping of the DS-20k LAr TPC	27
246 17	DS-20k cryogenics system P&ID	28
247 18	DS-20k condenser box	29
248 19	DS-20k materials database structure	32
249 20	Web interface of DS-20k materials database	33
250 21	Schematic of the sources insertion system	36
251 22	Pictures of the miniature $^{241}\text{AmBe}$ neutron source	37
252 23	Schematic and 3D cut-away view of the DS-20k veto detector	38
253 24	3D drawings of the DS-20k Veto detector	40
254 25	Picture of the LNS beamline in use for ReD	48
255 26	Preliminary data from the ReD experiment	49
256 27	The DS-Proto cryostat and components delivered at CERN	50
257 28	Conceptual design of the DS-Proto detector	52
258 29	Schematics of the setup for the optimization of the S2 signals	54
259 30	Details of the AAr cryostat	55
260 31	3D view of the large AAr cryostat	55
261 32	Cross-sectional view of the large AAr cryostat	56
262 33	Process Flow Diagram for the Urania UAr extraction plant	59
263 34	Screening test plant for the Urania PSA sorbent	60
264 35	Schematic view of UAr cryogenic shipping vessel	61
265 36	Block diagram of Aria	63
266 37	The Seruci-0 cryogenic distillation column	64
267 38	Preliminary Risk Registry Table	73

LIST OF TABLES

269 I	Radiogenic neutrons sourced by the detector construction materials and background 270 before and after cuts.	4
271 II	Managerial roles of the project	11
272 III	DS-20k LAr TPC detector parameters	20
273 IV	DarkSide-20k cryogenics system parameters.....	26
274 V	Summary of DS-20k assays performed.....	34
275 VI	Summary of the assay capabilities available for DS-20k	34
276 VII	Radiogenic neutrons from detector materials and background before and after cuts. .	41
277 VIII	Inlet argon purity required for operation of the DarkSide-20k getter	57

1. ORGANIZATION

279 **La parte iniziale del TDR riassume le motivazioni scientifiche e/o tecnologiche che
 280 hanno portato alla proposta per la realizzazione del progetto in questione, un'overview
 281 della soluzione proposta e l'evoluzione del progetto nel tempo. Si tratta di un som-
 282 mario esecutivo dalla lunghezza di 1-2 pagine, che include anche una descrizione som-
 283 maria dei contenuti del documento.**

2. PHYSICS CASE

285 **In questa parte viene riassunto inizialmente il lavoro svolto durante la fase di R&D
 286 del progetto, finanziata nella fase di CDR. Vengono descritti i risultati degli R&D ma
 287 anche i problemi trovati in questa fase, e le soluzioni proposte per risolverli o soluzioni
 288 alternative. Vengono anche elencati ulteriori R&D che si pensa di dover svolgere
 289 per finalizzare eventuali scelte tecniche Inoltre viene descritto il progetto nelle sue
 290 generalità e nel suo contesto. Vengono discusse le motivazioni scientifiche che hanno
 291 portato alla proposta in questione, con una chiara indicazione degli obiettivi e dei
 292 risultati attesi.**

293 There is strong evidence from astronomical and cosmological observations for the existence of
 294 dark matter in our Universe. Weakly Interacting Massive Particles (WIMPs) are a well-motivated
 295 dark matter candidate that may have been produced in the early Universe but are so massive and
 296 weakly interacting that they have yet to be observed in a terrestrial experiment. The observation
 297 of WIMPs with masses up to about $1 \text{ TeV}/c^2$ is a major objective of the experimental program at
 298 the High Luminosity Large Hadron Collider. Future high energy colliders like the FCC-*hh* (Future
 299 Circular Collider) will be able to extend these searches up to the $10 \text{ TeV}/c^2$ mass range [1]. Direct
 300 and indirect dark matter detection techniques allow for a search program complementary to future
 301 colliders. For example, the direct detection of dark matter via elastic scattering of galactic WIMPs
 302 from a liquid argon target is a demonstrated technique capable of probing masses well above the
 303 reach of the LHC.

304 Liquid argon (LAr) is a particularly favorable target for the detection of WIMPs thanks to its
 305 excellent event discrimination capabilities. Scintillation light initiated by particles recoiling from
 306 atomic electrons (ERs), the primary source of background in a WIMP direct detection experiment,
 307 has a time constant of approximately a microsecond. This is in stark contrast to the nanosecond
 308 time constant of scintillation light emitted during an expected WIMP-nuclear recoil event (NR).
 309 The DEAP-3600 experiment has exploited this effect via pulse shape discrimination (PSD) to
 310 achieve ER background rejection of 2.4×10^8 [2, 3]. Additional event discrimination in an argon-
 311 based detector was demonstrated by the DarkSide-50 (DS-50) experiment, which uses a two-phase
 312 time projection chamber to measure both the prompt argon scintillation light and the ionized
 313 electrons resulting from a particle interaction in the detector. This technique provides excellent
 314 position resolution and efficient detector fiducialization while maintaining PSD capabilities [4, 5].
 315 DS-50 has performed a blind analysis of their data and observed no background events over a run
 316 period in excess of two years [6]. In addition to sensitivity to WIMPs with masses above $30 \text{ GeV}/c^2$,
 317 the two-phase DS-50 detector has extended its reach to WIMP masses below $10 \text{ GeV}/c^2$ by detecting
 318 single ionizaton electrons extracted from the liquid argon volume [7, 8]. With careful control of ER
 319 background from local radioactivity and a reduction of the ^{39}Ar background, a 1 t LAr detector
 320 has the potential to reach the “neutrino floor” of solar neutrinos in this low-mass parameter space.

321 Given the potential reach of an argon-based detector, scientists from all of the major groups cur-
 322 rently using LAr to search for dark matter, including ArDM, DS-50, DEAP-3600, and MiniCLEAN,
 323 have joined to form the Global Argon Dark Matter Collaboration (GADMC) with a goal of building
 324 a series of future experiments that maximally exploit the advantages of LAr as a detector target.

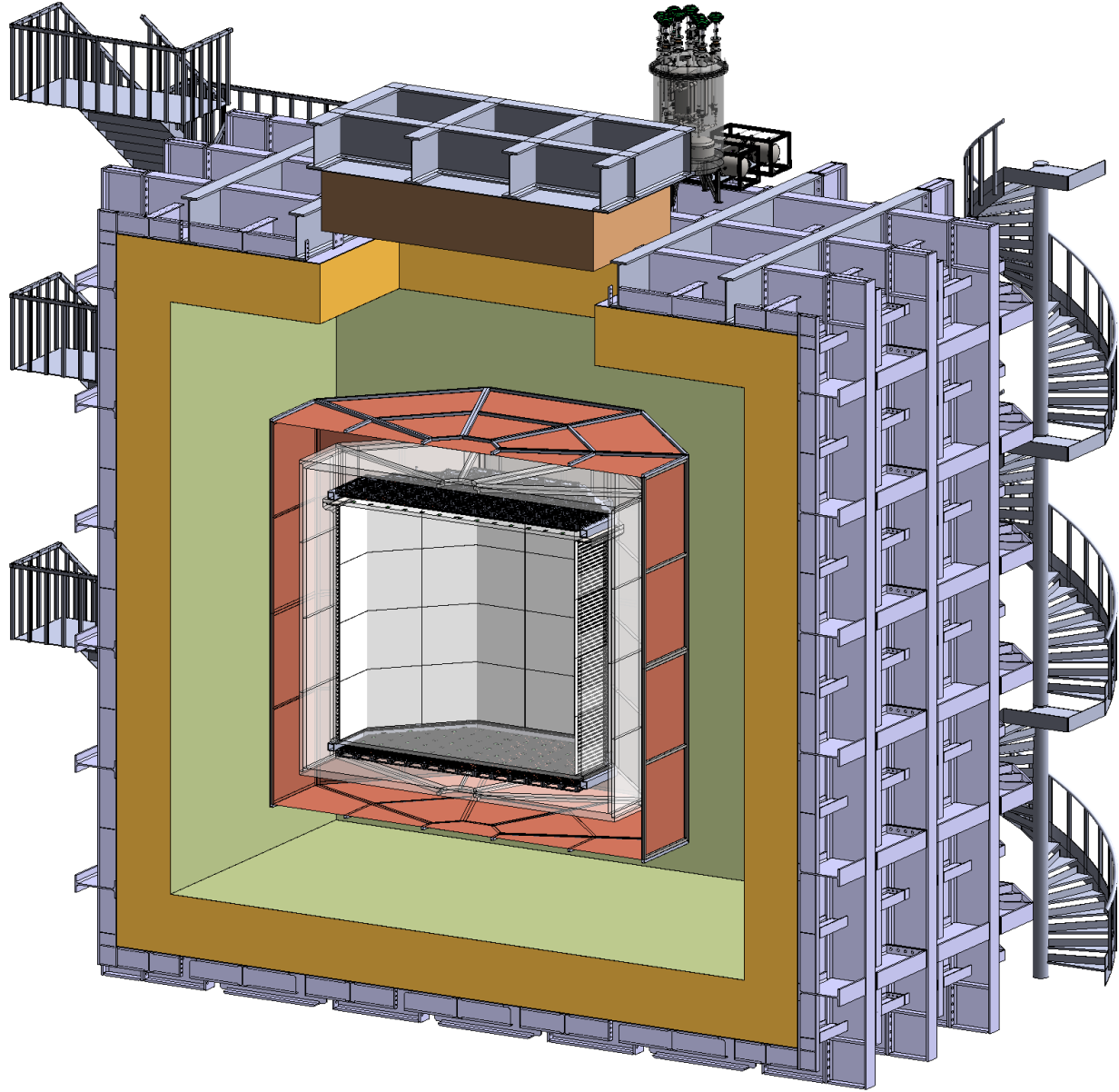


FIG. 1. Artist rendering of the DS-20k detectors, with many components omitted for clarity of presentation. The drawing shows the acrylic (PMMA) sealed TPC filled with UAr, surrounded by the veto detector consisting of a Gd-loaded acrylic Shell (GdAS) sandwiched between two atmospheric argon (AAr) active layers (the Inner Active Buffer, IAB and the Outer Active Buffer, OAB), all contained in the ProtoDUNE-like cryostat. The OAB is optically separated from the rest of the AAr by a copper vessel. Technical designs of the support structure of the TPC are already available, and intentionally omitted for clarity of presentation of the main elements.

325

2.1. DarkSide-20k: The High-Mass Search Program

326 The immediate objective of the GADMC is construction of the DS-20k two-phase LAr detector,
 327 which will operate in Hall-C of the Gran Sasso National Laboratory (LNGS). Fig. 1 shows a 3D
 328 schematic of the DS-20k detector. DS-20k detector consists of two nested detectors housed within
 329 a ProtoDUNE-style membrane cryostat [9, 10].

330 The inner detector is a dual-phase argon time projection chamber (LAr TPC) contained within
 331 a vessel made from ultra-pure acrylic (PMMA) and filled with UAr. The central active volume of

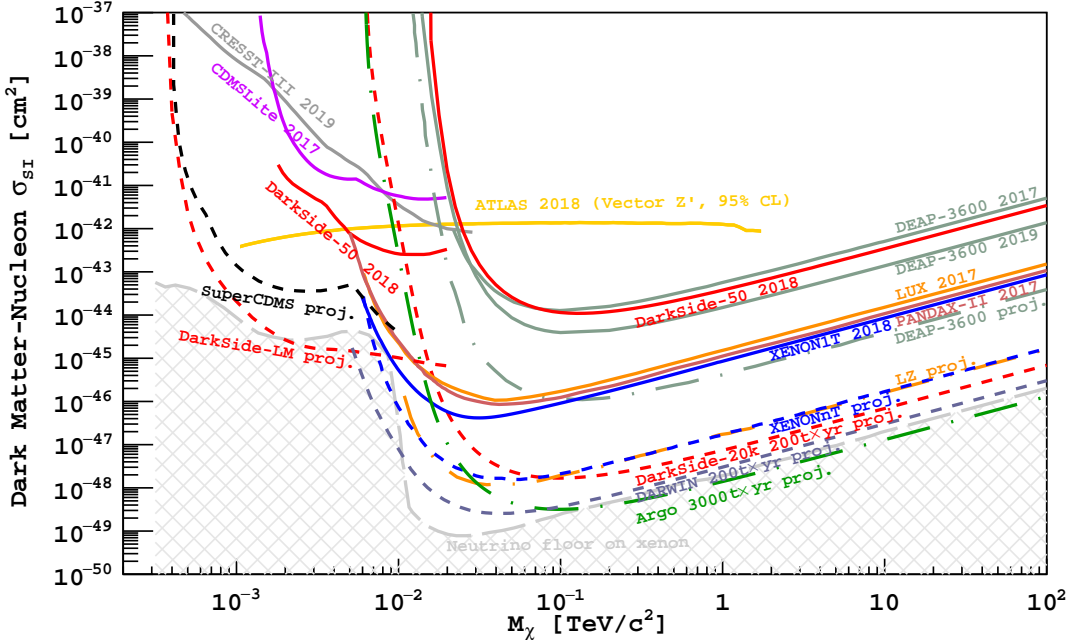


FIG. 2. 90 % C.L. exclusion limits showing leading results from direct (continuous lines, Ref. [6, 7, 12–15]) and accelerator-based dark matter searches (region above the yellow line [16]) compared with sensitivities of future germanium-, xenon-, and argon-based direct searches (dashed lines, Ref. [17–21] and this work). The “neutrino floor” curve follows the definition of Ref. [22]. The 95% C.L. limit from the ATLAS Experiment is shown for a benchmark model in which Dirac-fermion WIMPs interact with ordinary matter via a vector mediator with coupling strengths to quarks, leptons and WIMPs of 0.25, 0.01, and 1, respectively [23].

332 the TPC is defined by eight vertical reflector panels and the top and bottom windows of the acrylic
 333 vessel. Instead of the traditional copper field cage rings and Indium-Tin-Oxide (ITO) cathode
 334 and anode, DS-20k will use poly(3,4-ethylenedioxothiophene) polystyrene sulfonate (also known
 335 as PEDOT:PSS and commercialized under the name Clevios™ [11]). All the TPC surfaces in
 336 contact with the active argon volume will be coated with wavelength shifter tetraphenylbutadiene
 337 (TPB) to convert LAr scintillation light to a wavelength detectable by SiPMs. 8280 SiPM-based
 338 PhotoDetector Modules (PDM) arrays will view the argon volume through the top and bottom
 339 windows of the acrylic vessel. The height of the TPC is 350 cm. The total mass of LAr in the
 340 active volume is 49.7 t.

341 The outer veto detector is made of a passive Gd-loaded PMMA shell surrounding the inner
 342 detector and between two active AAr layers. The Gd-loaded PMMA shell moderates
 343 neutrons emitted from the LAr TPC until they capture on Gd, resulting in the emission of multiple
 344 γ -rays. The γ -rays interact in the AAr layers and cause scintillation light that is detected by
 345 photodetectors, thereby providing an efficient veto of radiogenic neutrons that could result in a
 346 NR in the TPC. The ProtoDUNE-like cryostat will be surrounded by layers of plastic to moderate
 347 cosmogenic and radiogenic neutrons from the rocks surrounding Hall C.

348 The DS-20k detector will have ultra-low backgrounds and the ability to measure its backgrounds
 349 *in situ*, resulting in an expected sensitivity to WIMP-nucleon cross sections of $1.2 \times 10^{-47} \text{ cm}^2$
 350 ($1.1 \times 10^{-46} \text{ cm}^2$) for $1 \text{ TeV}/c^2$ ($10 \text{ TeV}/c^2$) WIMPs following a five years run. This projected
 351 sensitivity is a factor of >50 better than currently-published results above $1 \text{ TeV}/c^2$ and covers a
 352 large fraction of the parameter space currently preferred by supersymmetric models.

353 The sensitivity would further improve to $7.4 \times 10^{-48} \text{ cm}^2$ ($6.9 \times 10^{-47} \text{ cm}^2$) for $1 \text{ TeV}/c^2$ ($10 \text{ TeV}/c^2$)
 354 WIMPs for a ten years run with a 200 t yr exposure, see Fig. 2. During the 200 t yr exposure, 3.2
 355 NRs events are expected from the coherent scattering of atmospheric neutrinos, making DS-20k the

Material	Mass [tonne]	^{238}U [mBq/kg]	^{226}Ra [mBq/kg]	^{232}Th [mBq/kg]	Neutrons $[10 \text{ yr}]^{-1}$	+TPC $[200 \text{ t yr}]^{-1}$	+TPC+veto $[200 \text{ t yr}]^{-1}$
TPC Vessel	2.7	1.2×10^{-2}	10	4.1×10^{-3}	5.7×10^2	0.17	1.7×10^{-2}
TPC SiPMs	0.12	-	-	-	5.4×10^3	0.16	1.6×10^{-2}
TPC Electronics	1.0	-	-	-	1.2×10^4	0.36	3.6×10^{-2}
TPC Mechanics	1.1	3.9	3.9	1.9	9.0×10^2	1.8×10^{-2}	2.0×10^{-3}
Veto SiPMs+elec.	0.40	-	-	-	6.4×10^3	0.10	1.0×10^{-2}
Veto Acrylic	13	1.2×10^{-2}	10	4.1×10^{-3}	2.6×10^3	4.2×10^{-2}	4.0×10^{-3}
Veto Reflectors	1.0	1.2×10^{-2}	1.0	4.1×10^{-3}	2.0×10^2	2.4×10^{-2}	2.0×10^{-3}
Veto Steel	1.1	3.9	3.9	1.9	9.0×10^2	1.4×10^{-2}	1.0×10^{-3}
$\text{Gd}_2(\text{SO}_4)_3$ α 's on self	0.26	7.0	7.0	0.2	1.1×10^2	2.0×10^{-3}	$<1.0 \times 10^{-3}$
$\text{Gd}_2(\text{SO}_4)_3$ α 's on PMMA	0.26	7.0	7.0	0.2	3.6×10^2	6.0×10^{-3}	1.0×10^{-3}
Copper Cage	1.0	0.30	0.30	2.0×10^{-2}	6.0	$<1.0 \times 10^{-3}$	$<1.0 \times 10^{-3}$
Cryostat Steel	250	50	1.0×10^3	3.9	1.0×10^6	-	$<1.0 \times 10^{-3}$
Cryostat Insulation	40	3×10^3	8.0×10^3	3.0×10^3	8.0×10^7	-	$<1.0 \times 10^{-3}$
Total						0.9	0.09

TABLE I. Radiogenic neutrons sourced by the LAr TPC construction materials, veto and cryostat materials, with details of expected contamination levels, background after TPC cuts, and residual background after combined TPC and veto cuts, all relative to the full 10 yr run time and the full fiducial 200 t yr exposure. The number of neutrons source is calculated from the expected contamination levels and material composition. Note that no specific activity is reported for the TPC SiPMs and associated electronics: in this case the predicted neutron yield is the results of an extremely detailed calculation, accounting for the cumulative contribution of several tens of components, individually assayed. The same consideration holds for the veto SiPMs and electronics, whose contribution is reported in combination. For neutrons due to (α, n) reactions from α 's from impurities in $\text{Gd}_2(\text{SO}_4)_3$, the contribution is broken down between those due reactions on Gd sulfate itself and those due to reactions in the PMMA matrix containing the Gd sulfate; the mass fraction of Gd in the GdAS 1%, for the anticipated 2% concentration by mass of $\text{Gd}_2(\text{SO}_4)_3$. (For ease of conversion: 1 ppt(^{238}U) $\simeq 1.2 \times 10^{-2}$ mBq/kg; 1 ppt(^{232}Th) $\simeq 4.1 \times 10^{-3}$ mBq/kg.)

356 first ever direct dark matter detection experiment to reach this milestone. The DS-20k experiment
 357 is foreseen to begin operating in 2022 and will either detect WIMP dark matter or exclude a large
 358 fraction of favored WIMP parameter space.

359 DS-20k is designed to operate with zero backgrounds, meaning that all sources of instrumental
 360 background are reduced to <0.1 events over a 200 t yr exposure. All background from minimum-
 361 ionizing radiation sources will be completely removed thanks to the combined action of PSD of the
 362 primary scintillation pulse and comparison of the primary and secondary scintillation (see Sec. 22.4
 363 for details on the suppression of background from pp scatters on electrons and Ref. [24] for that
 364 from ^{222}Rn , ^{220}Rn , and progenies). Table VII shows the expected radiogenic neutron background
 365 contributions of the various detector components following all TPC and veto cuts for the full DS-20k
 366 exposure. The only remaining background for WIMP searches will be the signal from the coherent
 367 scattering of atmospheric neutrinos on argon nuclei, with an expected 3.2 events over the 200 t yr
 368 exposure. DS-20k will thus be the first experiment in a position to detect this important signal.

369 This outstanding sensitivity to coherent nuclear recoils will enable DS-20k to detect a supernova
 370 neutrino burst coming from anywhere in the Milky Way Galaxy and, for a majority of the galaxy,
 371 clearly identify the neutronization burst. DS-20k would perform a flavor-blind measurement of
 372 the total neutrino flux and average energy, setting an overall normalization that is not affected
 373 by neutrino oscillations. When combined with a flavor-specific measurement from a detector like
 374 Super-Kamiokande or DUNE, this observation could have sensitivity to the neutrino mass hierarchy.

375 **2.2. DarkSide-LowMass: The Low-Mass Search Program**

376 In parallel to DS-20k detector, the GADMC will pursue the development of an approximately
 377 1 t detector specifically optimized for the detection of low-mass dark matter, DarkSide-LowMass
 378 (DS-LM). DS-LM will achieve a lower energy threshold than DS-20k by triggering on the electro-

379 luminescence signal from ionization electrons, thereby adding sensitivity to WIMP masses below
380 $10 \text{ GeV}/c^2$ at the expense of the PSD power afforded by argon prompt scintillation light. Without
381 PSD, contributors to the ER background in DS-LM must be reduced beyond the requirements of
382 DS-20k through careful detector design and material selection. While the DS-LM experiment is
383 outside the scope of this proposal, the implementation of DarkSide-20k project will have direct
384 impacts on the technological advancements required to enable DS-LM and the goal of reaching the
385 neutrino floor for WIMP masses between $1 \text{ GeV}/c^2$ and $10 \text{ GeV}/c^2$, see Fig. 2. Among these are the
386 development of low-background PDMs [25, 26] and the construction of the Aria cryogenic distilla-
387 tion column, which will completely remove ^{85}Kr and reduce ^{39}Ar levels to the level of $1 \mu\text{Bq}/\text{kg}$.
388 The development of DS-LM may exploit components of the DS-Proto detector under development
389 at CERN. Funding for the development, construction, commissioning, and operation of DS-LM
390 will be separately requested via alternative funding programs.

391

2.3. Argo

392 The ultimate objective of the GADMC is the construction of the Argo detector, which will have
393 a 300 t fiducial mass and will push the experimental sensitivity to the point at which the coherent
394 scattering of atmospheric neutrinos becomes a limiting background. The excellent ER rejection
395 possible in argon will eliminate backgrounds from solar neutrinos, which will extend the sensitivity
396 of Argo beyond that of technologies with more limited ER discrimination. The throughput of the
397 Urania plant and Aria facility will enable 400 t of UAr to be extracted and purified over a period
398 of about 6 yr. In addition to dark matter detection, such a large detector would also have excellent
399 sensitivity to a neutrino burst associated with a galactic supernova. If located at SNOLAB or at
400 similar depth, Argo will also have the potential to observe CNO neutrinos for the first time and
401 solve the Solar Metallicity Problem [27]. While the construction of Argo is not within the scope of
402 this proposal, the implementation of DarkSide-20k project will pave the way for the development
403 of Argo towards the end of the next decade.

404 Combined DS-20k, DS-LM, and Argo, will completely cover the spin-independent WIMP hy-
405 pothesis parameter space down to the neutrino floor for WIMP masses from $1 \text{ GeV}/c^2$ to several
406 hundreds of TeV/c^2 .

407

2.4. Comparison with Xenon-Based Experiments and the “Neutrino Floor”

408 Next generation dark matter experiments will be sensitive to several sources of neutrinos via $\nu - e$
409 elastic scattering and coherent elastic neutrino scattering ($\text{CE}\nu\text{NS}$) on nuclei (NR). Atmospheric
410 and diffuse supernovae neutrinos, which due to their high energies can produce NRs in excess of
411 $20 \text{ keV}_{\text{nr}}$, will be the dominant $\text{CE}\nu\text{NS}$ background contributor for WIMP masses above $30 \text{ GeV}/c^2$.
412 Solar neutrinos are the main $\text{CE}\nu\text{NS}$ background for dark matter masses below $10 \text{ GeV}/c^2$. With
413 argon’s ability to discriminate ER from NR to better than a part in 2.4×10^8 , $\text{CE}\nu\text{NS}$ represents
414 the only irreducible background for a large exposure argon dark matter search. The neutrino
415 background is exacerbated in liquid xenon detectors, which, due to their limited ER rejection
416 power, accept a non-negligible number of $\nu - e$ elastic scatters as signal.

417 When calculating the discovery sensitivity of a large dark matter search experiment, one must
418 fully account for the presence of neutrino-induced backgrounds. We note that the position of the
419 “neutrino floor”, initially conceived as indicative of the maximum sensitivity attainable by an ex-
420 periment in the presence of $\text{CE}\nu\text{NS}$ background, is critically dependent on the target, experimental
421 technique, statistical analysis, neutrino flux uncertainty and theoretical cross section uncertainty.
422 We therefore include a detailed accounting of the $\text{CE}\nu\text{NS}$ and $\nu - e$ backgrounds in the sensitivity
423 and discovery potential curves shown in Fig. 2 and Fig. 3. We conservatively estimate a 20 % un-
424 certainty on the neutrino background for high-mass ($30 \text{ GeV}/c^2$) searches with Argo. This accounts
425 for a 15 % uncertainty on the atmospheric neutrino flux at mid-latitude locations, such as SNOLAB

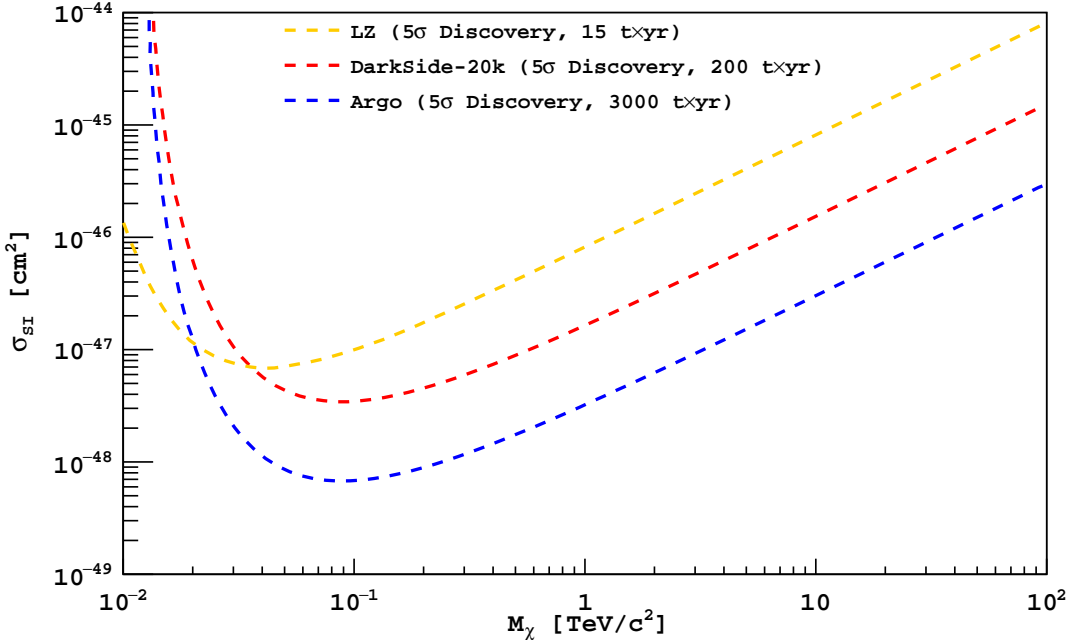


FIG. 3. 5σ discovery potential of the leading future noble liquid dark matter searches.

426 or LNGS, based on the latest data-driven models of cosmic primaries [28] as well as models of solar
 427 cycle, seasonal, geographic, and geomagnetic dependence of the neutrino flux [29, 30]. Additionally,
 428 we account for a 5 % theoretical uncertainty on the Standard Model interaction cross-section, driven
 429 by uncertainties on the nuclear form factor and the expected constraints that the COHERENT col-
 430 laboration will place on non-Standard Model contributions using a LAr target [31], which in turn
 431 is driven by their current 10 % uncertainty on neutrino flux [32] and a 6 % uncertainty on the LAr
 432 response as measured by SCENE [33, 34] and ARIS [35]. Planned improvements of COHERENT,
 433 including a sharper characterization of the neutrino flux and a measurement with a LAr target,
 434 would further reduce the uncertainty on the neutrino background below 10 %, strongly benefiting
 435 the DS-20k, and Argo experiments.

436 Within this framework, we calculate the 5σ discovery potential for DS-20k and Argo and compare
 437 it with that of the near-future LXe experiment LZ [36]. As seen from Fig. 3, DS-20k has significantly
 438 greater discovery potential than that of LZ.

439 2.5. Completed R&D for DS-20k Program

440 The following technologies are key to the success of DarkSide-20k project and the long term
 441 scientific goals of the GADM. Their development will also have potentially wide-reaching effects
 442 within the physics community.

443 **Low-Radioactivity Underground Argon with Urania** [24]: The DS-50 experiment estab-
 444 lished that UAr is depleted of ^{39}Ar by a factor of approximately 1400, a sufficiently low rate to be
 445 deployed in a detector the size of DS-20k. However, constructing DS-20k will require that large
 446 amounts of UAr be procured in a timely fashion. This will be accomplished by Urania, an argon
 447 extraction and purification plant capable of extracting 250 kg/d of UAr. The Urania plant is fully
 448 funded by the INFN and will be built by a contracted vendor following specifications established
 449 by the Urania Project team. The tender process for the plant's final design, construction, and
 450 shipment to the installation site in Cortez, Colorado, is underway and will conclude by the end

451 of July 2019 with the selection of a contractor. The preparation of the extraction site, as well
452 as the installation and commissioning of the plant, falls under the responsibility of the U.S. NSF-
453 supported groups. The Urania UAr extraction plant is projected to collect approximately 60 t of
454 argon for use in DS-20k detector by 2022 and could continue to produce underground argon for
455 Argo and other interested particle physics experiments that require UAr to achieve their scientific
456 objectives.

457 **Purification and Active Depletion with Aria [24]:** The Aria plant is a 350 m tall cryogenic
458 distillation column that was designed to explore the possibility of chemically separating argon iso-
459 topes. The construction of Aria is fully supported by INFN and Regione Autonoma della Sardegna.

460 **SiPM-based Cryogenic Photosensors [24–26]:** The development of low-background, large-
461 area, cryogenic silicon photomultiplier (SiPM) detectors capable of replacing conventional photo-
462 multiplier tubes is critically important for achieving the desired sensitivity of DS-20k and other
463 large-scale LAr-based experiments, including DUNE, and LXe-based detectors, such as nEXO [37]
464 and NEXT [38–40]. The DS-20k photodetector modules will be assembled at the Nuova Offi-
465 cina Assergi (NOA), a dedicated cleanroom packaging facility that will have future utility for any
466 experiment needing large volume silicon detector production.

467 **ProtoDUNE Liquid Argon Cryostat [9, 10]:** DS-20k detector will operate within a mem-
468 brane cryostat filled with liquefied atmospheric argon, a technology initially developed at CERN
469 for ProtoDUNE. Eliminating the organic liquid scintillator veto used in DS-50 for the AAr veto
470 has several advantages. With the the DS-20k LAr TPC directly immersed in AAr, the massive
471 stainless steel vacuum cryostat necessary for DS-50, and its correspondingly large contribution of
472 background events, can be replaced with a transparent, radio-pure PMMA vessel. Photodetector
473 modules can then be mounted outside of the PMMA vessel, reducing their contribution to the
474 background rate and simplifying their assembly strategy. The ProtoDUNE cryostat has the added
475 advantage that it is scalable, making it a technology appropriate for Argo.

476 **Sealed PMMA TPC [2, 41, 42]:** The DEAP-3600 collaboration has extensive experience
477 developing large, radio-pure sealed PMMA vessels. This technology will be used to build the vessel
478 for the DS-20k LAr TPC, eliminating the need for some of the most problematic radiogenic neutron
479 contributors in DS-50, most notably the stainless steel cryostat. The PMMA vessel will also reduce
480 the complexity of the TPC assembly.

481 2.6. Ongoing R&D for DS-20kProgram

482 All the major technologies needed for the design and construction are proven and do not neces-
483 sitate further R&D by the collaboration as discussed in the preceding paragraph. Some limited
484 developments are only needed in order to finalize the mass production for SiPM and the production
485 of the Gd loaded acrylic panels for the construction of the neutron veto. In both cases the R&D is
486 actively on-going and will be finalized by 2020.

487 3. ORGANIZATION

488 Definire la struttura organizzativa dell'esperimento:

- 489 • Spokesperson,
- 490 • Technical Coordinator,
- 491 • Local Responsible,
- 492 • Site Manager,
- 493 • Funds Responsible,
- 494 • GLIMO-S&E.

495 The organization structure of the GADMC and of the DarkSide project is defined in Fig. 4. The
496 governance of the GADMC is carried out by two distinct branches: the policy-making branch and
497 the executive branch.

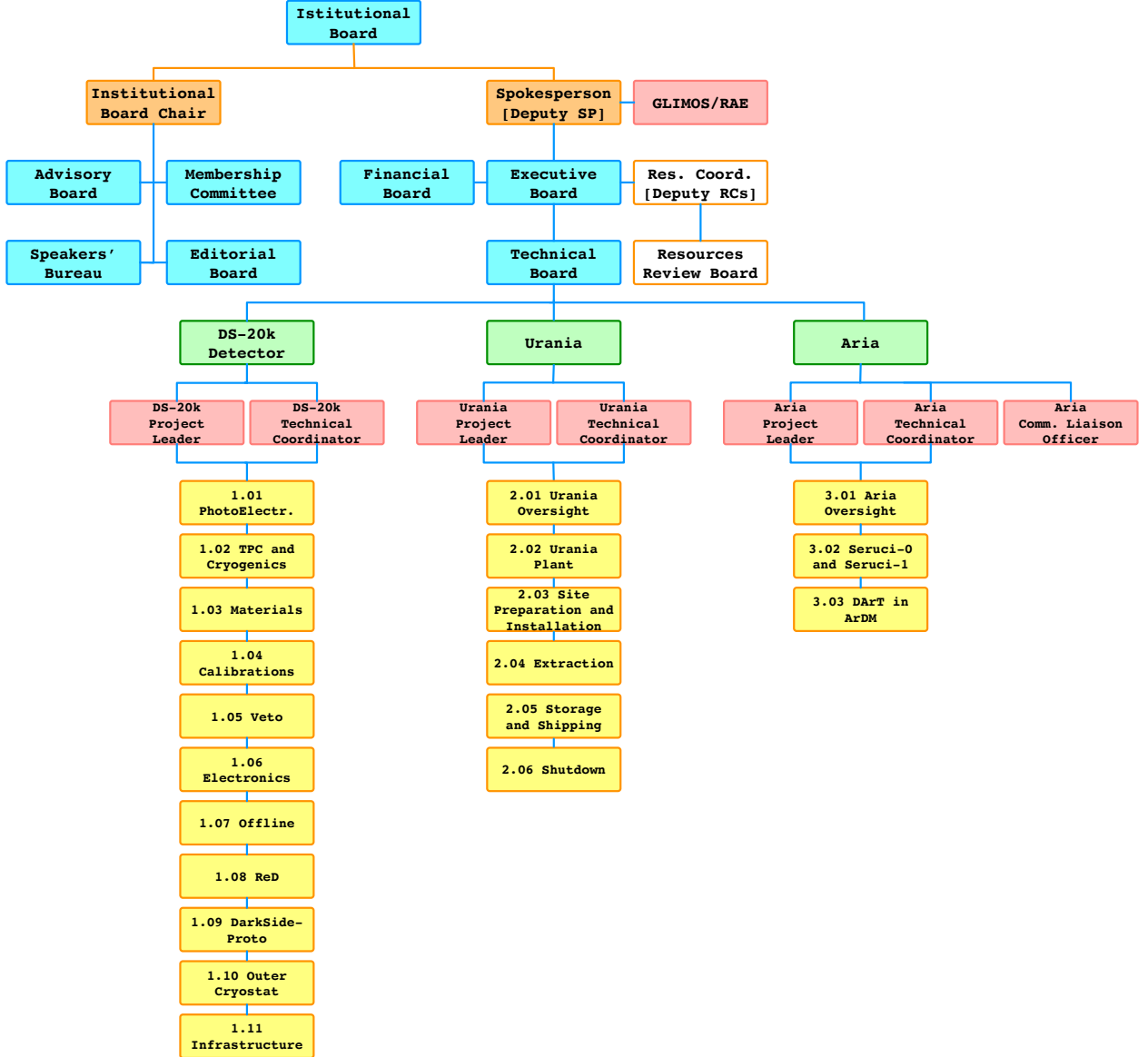


FIG. 4. The organization structure of the GADMC and of the DarkSide project.

498 The organization structure of the DarkSide project is defined in Fig. 4. The governance is carried
 499 out by two distinct branches: the policy-making branch and the executive branch.

500 Policy-making is done by the **Institutional Board (IB)**. Each institution is represented within
 501 the IB by its PI. The IB is guided by an elected **IB Chair** with a renewable 2 year mandate. The
 502 IB is responsible for the definition of rules and the governance of the Collaboration, the overall
 503 organization of the Collaboration, the appointment of all managers belonging to the policy-making
 504 and executive branches; the final approval of major design changes proposed by the executive
 505 branch; and the control of financial and human resources. The current IB Chair is G. Batignani
 506 (Pisa), elected in November 2016 and re-confirmed in November 2018.

507 Within the policy-making branch there are three committees charged with providing recommen-
 508 dations to the IB and its Chair. The members of the three committees are appointed by the IB
 509 upon proposal of the IB Chair, taking into account the composition of the Collaboration and the
 510 need to represent its diverse composition. These three committees are:

511 **The Advisory Board**, consisting of the IB Chair and 6 senior IB members nominated by the
 512 IB Chair, of which 2 members are from Italian institutions, 1 member is from a US institution,

513 1 member is from a Canadian institution, and 2 members are from institutions outside the
514 three countries already listed. This committee is mandated with advising the IB Chair on IB
515 management issues.

516 **The Membership Committee**, consisting of 6 members nominated by the Advisory Board and
517 confirmed by the IB, as well as 2 *ex officio* Advisory Board members. This committee addresses
518 requests from new groups wishing to join the Collaboration, helps define the commitments of
519 new groups, and maintains the database and mailing lists of the collaboration.

520 There are two additional committees within the policy-making branch charged with providing
521 recommendations to the IB on the communication of scientific and technological results. The
522 members of the two committees are appointed by the IB upon proposal of the IB Chair, taking into
523 account the composition of the Collaboration and the need to represent its diverse composition.

524 The two committees are:

525 **The Speakers' Bureau**, consisting of 5 members nominated by the Advisory Board and con-
526 firmed by the IB, 1 *ex officio* Advisory Board member, and the SP and Deputy SP. This commit-
527 tee appoints speakers at conferences and workshops and approves material that will be presented
528 on behalf of the Collaboration.

529 **The Editorial Board**, consisting of 6 members nominated by the Advisory Board and confirmed
530 by the IB. This committee approves the start of paper preparation, guides the internal paper
531 review process, and issues final approval of papers before publication.

532 The executive branch of the GADMC is led by an elected **Spokesperson (SP)**. The primary
533 responsibility of the SP is to oversee the DS-20k experiment, oversee any other scientific efforts
534 pursued by the Collaboration, and act as the Collaboration's primary public face. The SP is
535 assisted by an elected **Deputy SP (dSP)**. The mandates of the SP and dSP are 3 years, renewable.
536 C. Galbiati and G. Fiorillo were elected as SP and Deputy SP respectively in December 2016.

537 The DarkSide-20k project is organized into 3 sub-projects: the **DS-20k detector**, **Urania**,
538 and **Aria**. Each of the sub-projects is managed by two **Project Coordinators (PCs)**, *i.e.*,
539 a **Project Leader (PL)** and a **Technical Coordinator (TC)**. The PL manages the overall
540 progress of the sub-project and is responsible for and coordinates the **Level-1 (L1) Work Groups**
541 (**WGs**) in which the sub-project tasks and objectives are subdivided and organized, ensuring
542 that the design and construction of the sub-project is carried out on schedule, within the cost
543 ceiling, and in a way that meets the performance and reliability requirements determined within
544 the framework of GADMC resource planning. The PL plans the schedule and budget, sets deadlines,
545 and monitors quality and progress of the sub-project under their oversight. The TC is responsible
546 for the sub-project construction and the technical integration of all its components. The TC ensures
547 the implementation of engineering standards and procedures, monitors the overall construction of
548 detectors and infrastructure, and is responsible for the sub-project's integration and safety. The
549 Aria sub-project, due to its complex nature, has an additional PC, a **Community Liaison Officer**
550 charged to act as a link with the local authorities in Sardinia.

551 In addition to the PCs defined above, three **Project Scientists (PSs)** are charged with the
552 scientific oversight of the detector design and construction to ensure that all technical decisions are
553 fully compliant with the requirements of the project and compatible across all sub-systems.

554 The management of each sub-project is divided between **Level-1 (L1) Managers** and **Level-
555 2 (L2) Managers**, who are responsible for the direction of the **L1** and **L2 WGs** in which the
556 sub-project are organized and structured.

557 The **Executive Board (EB)**, which is chaired by the SP and includes as members the dSP, the
558 PSs, all PCs, and all L1 Managers, manages the executive branch of the GADMC. The IB Chair
559 is an *ex officio* member of the EB. The SP regularly invites senior PIs charged with significant
560 organization and funding responsibilities but without a formal PC role to the EB meetings.

561 The PSs and the PCs of DS-20k and Urania report to the EB. The PCs of Aria report to the
562 **Scientific Responsible (SR) of Aria**, which is jointly appointed by INFN and the Regione
563 Autonoma della Sardegna. The SR of Aria is C. Galbiati, the inventor and founder of the Aria
564 program. The SR of Aria reports to the EB.

565 All PCs and PSs are nominated by the SP to the EB, proposed by the EB to the IB, and

566 appointed by the IB. PCs are required to pledge that DS-20k will be their top scientific priority
567 and that they will dedicate a dominant fraction of their research time to their effort within the
568 GADMC. The EB and by the IB monitor closely the effectiveness of the PCs.

569 The L1 Managers are proposed by the PCs, confirmed by the EB, and appointed by the IB.
570 The L1 Managers report to the PCs. The L2 Managers are proposed by the L1 coordinators in
571 concurrence with the PCs, confirmed by the EB, and appointed by the IB. The L2 Managers report
572 to the L1 Managers.

573 The **Technical Board (TB)**, chaired by the SP and with a membership of the dSP, the PSs,
574 all PCs, and all L1 and L2 Managers, is responsible for the execution of the project. The IB Chair
575 is an *ex officio* member of the TB. All TB meetings and calls are open to the entire Collaboration.
576 The TB is the forum where all major and minor decisions affecting the project are debated and
577 finalized. In its decision making process, the TB typically operates by building consensus. The TB
578 also monitors the execution of the individual sub-projects and discusses matters at the interface
579 between different sub-projects. All TB meetings are prepared and chaired by the DS-20k TC.

580 The DarkSide resource coordination is delegated to a **Resources Coordinator (RC)**, who has
581 responsibility for the administration of the common fund. The RC is appointed by the IB upon
582 proposal of the EB.

583 The **Resources Review Board (RRB)** is made up of representatives from the funding agencies
584 providing major contributions to the project, the IB Chair, the SP, the dSP, the RC, and the
585 **Country Representatives (CRs)**, who are appointed by the assembly of PIs supported by any
586 given funding agency and is in charge of the relationship with said agency. The RRB responsibilities
587 include the monitoring and management of the financial instruments that constitute the GADMC
588 resources, defining the national and regional contributions to the project, developing the MoU, and
589 approving in-kind contributions. The **Financial Board (FB)** is composed of the CRs and advises
590 the SP on the specific allocation of tasks and funding requests.

591 A requirement of the LNGS Safety Management System is the appointment of a collaborator as a
592 **Group Leader in Matters of Safety (GLIMOS)**. The GLIMOS has the primary responsibility
593 for health and safety within the Collaboration, providing an interface with LNGS. The GLIMOS
594 is appointed by the LNGS Director upon recommendation by the Collaboration. An additional
595 requirement of the LNGS Environmental Management System is the appointment of a collabora-
596 tor as contact person for environmental issues or **Referente Ambientale dell'Esperimento**
597 (**RAE**). The RAE acts as the link between the experimental collaboration and LNGS for all mat-
598 ters concerning environmental protection. The RAE is appointed by the LNGS Director upon
599 recommendation by the Collaboration management

600 3.1. Specific Roles and Responsibilities

601 Table II offers a brief summary of the most significant executive responsibilities within the 3
602 sub-projects.

603 4. PROJECT OVERVIEW

604 **Sulla base del disegno concettuale e dei risultati della fase di ricerca e sviluppo**
605 **identificati nel paragrafo 2 del CDR si illustra la configurazione finale dell'apparato**
606 **proposto. Le caratteristiche dell'esperimento, quelle dei sistemi e dei sottosistemi**
607 **principali devono essere descritte e riassunte tramite tavole e schema del PBS (Product**
608 **Breakdown Structure), un esempio mostrato in figura 1. Vengono altresì mostrati i**
609 **requisiti del progetto nella presente configurazione.**

610 Many fundamental design parameters for the DarkSide-20k (DS-20k) experiment are based on
611 the successful experience of the DarkSide Collaboration in constructing, commissioning, and oper-
612 ating the DarkSide-50 (DS-50) detector in a background-free mode. The many technical details of

Project Scientists		P. Meyers W. Bonivento A. Razeto	Princeton INFN Cagliari INFN LNGS
DS-20k Project Coordinators	Project Leader Technical Coordinator	E. Scapparone An. Ianni	INFN Bologna Princeton
	DarkSide-Proto Managers	G. Fiorillo	INFN Napoli
	Technical Integration Manager	T. Napolitano	INFN LNF
	Materials Manager	R. Santorelli	CIEMAT
	ArDM Manager	C. Regenfus	ETH Zürich
	Inner Detector Manager	H. Wang	UCLA
	Deputy Inner Detector Manager	E. Pantic	UC Davis
	Outer Detector Manager	G. Testera	INFN Genova
DS-20k L1 Managers	Deputy Outer Detector Manager	J. Monroe	RHUL
	PhotoElectronics Manager	A. Razeto	INFN LNGS
	Electronics Manager	M. Rescigno	INFN Roma 1
	Calibration Manager	J. Maricic	Hawai'i
	Offline Manager	D. Franco	CNRS/IN2P3
	ReD Manager	L. Pandola	INFN LNS
	Outer Cryostat Manager	M. Nessi	CERN
Urania Project Coordinators	Project Leader Technical Coordinator	M. Simeone A. Renshaw	INFN Napoli University of Houston
Urania L1 Managers	Plant Manager Site Preparation and Installation Extraction	M. Simeone A. Renshaw H. Back	INFN Napoli Houston PNNL
Aria Project Coordinators	Project Leader Deputy Project Leader Technical Coordinator Deputy Technical Coordinator Community Liason Officer	W. Bonivento F. Gabriele R. Tartaglia M. Razeti A. Devoto	INFN Cagliari INFN LNGS INFN LNGS INFN Cagliari INFN Cagliari
Aria L1 Managers	Seruci-I Manager DArT Manager	F. Gabriele W. Bonivento	INFN LNGS INFN Cagliari

TABLE II. Overview of the most significant managerial roles within the DarkSide sub-projects.

613 DarkSide-50 can be found in [4–8, 35, 43–50]. The DS-20k liquid argon time projection chamber
 614 (LAr TPC) will, too, be deployed at LNGS in the underground Hall C, at the center of a newly
 615 constructed active veto system. Fig. 5 shows the rendering of the future installation of DS-20k in
 616 the underground Hall C of LNGSand Fig. 1 shows an overview of the detailed arrangement of the
 617 LAr TPC and its anti-coincidence veto detector. The DS-20k experiment is designed to operate for
 618 a minimum of 10 yr while maintaining an irreducible background level in the WIMP search region
 619 of less than <0.1 events for the total exposure. To achieve this goal, the design parameters of the
 620 DS-20k experiment have been taken directly from DS-50, where possible. Design changes have been
 621 made where needed in order to accommodate for the much larger size of DS-20k and to allow the
 622 experimental design to be scalable to a detector at the multi-hundred tonne scale. In building this
 623 preliminary design, issues that have arisen because of design choices or materials selections have
 624 been dealt with by limited design modifications, and further optimization will continue as the final
 625 development work is completed and a full technical design is made.

626 DS-20k will be built by the Global Argon Dark Matter Collaboration (GADM) and will consist
 627 of two detectors: the inner detector and the veto detector, both hosted in a ProtoDUNE-like
 628 cryostat [9, 10]. The inner detector is a LAr TPC filled with underground argon (UAr). The veto
 629 detector is made of a plastic shell, loaded with Gd, surrounding the inner detector, sandwiched
 630 between two active atmospheric argon (AAr) layers.

631 The decision to abandon an organic liquid scintillator veto and to host DS-20k within a
 632 ProtoDUNE-like cryostat was originally motivated by the need of minimizing the environmen-
 633 tal impact on underground LNGS operations, but carries significant performance advantages.
 634 Indeed, operating the TPC directly in the ProtoDUNE-like cryostat eliminates the need of a cryo-

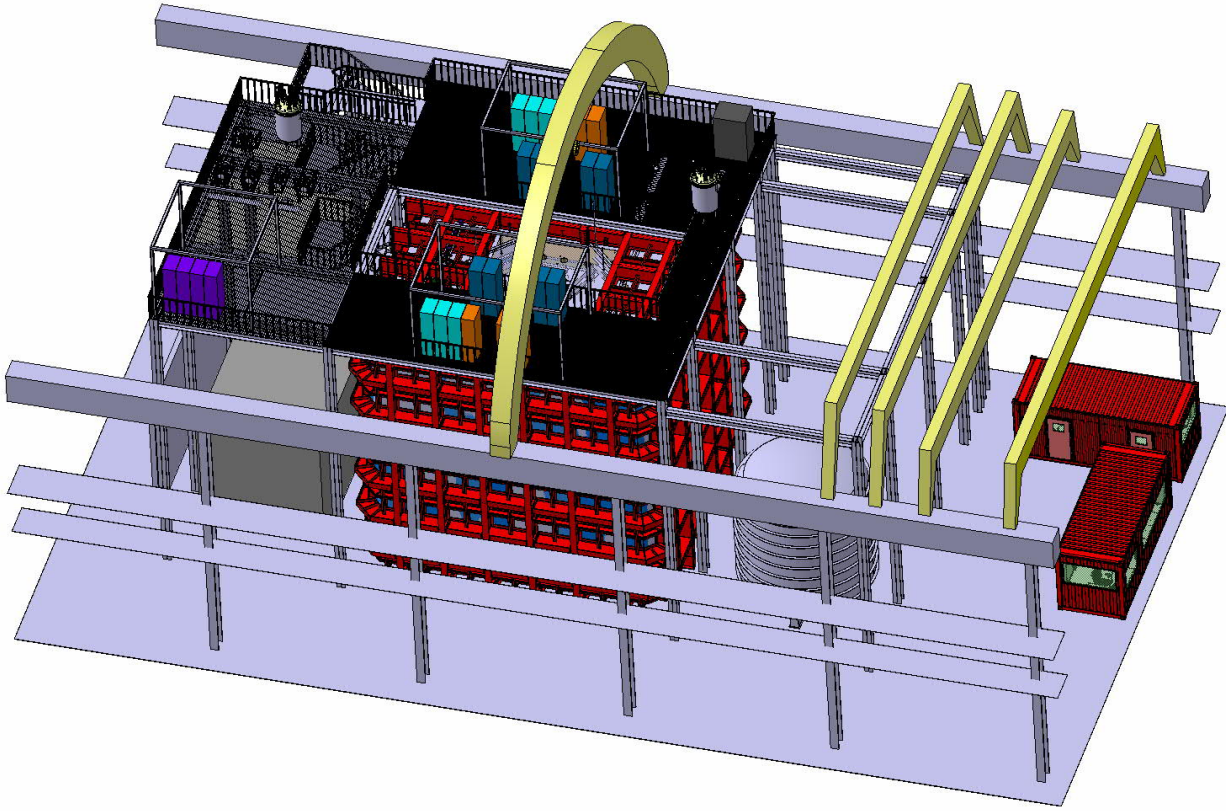


FIG. 5. Artist rendering of the DS-20k experiment in Hall C of LNGS.

stat in the immediate proximity of the UAr target, which would significantly contribute to the residual background. We therefore adopted a new design, with the UAr-filled TPC immersed in a bath of liquefied AAr held at the same temperature and pressure. This then allows for the use of a TPC vessel fabricated from the same ultra-pure poly(methyl methacrylate) (acrylic or PMMA) developed for the DEAP-3600 experiment, and thus eliminating the need for a dedicated cryostat or UAr containment vessel. The outer walls of the TPC will sit approximately 2 m away from inner wall of the cryostat. The ProtoDUNE-like cryostat may be surrounded by layers of plastic for moderation of cosmogenic and radiogenic neutrons from the rocks surrounding the LNGS Hall C, this option is being investigated.

While this overview section gives a general outline of the project and introduces the major features of the experiment as they stand in the current preliminary design, the real details are given in the subsequent sections. The development of the SiPM photosensors, the LAr TPC and its cryogenics and gas handling system, and the materials screening plan that will ensure the radio purity of the experiment, are detailed in Sec. 5, Sec. 6 and Sec. 7, respectively. The plan for the calibration of the experiment is given in Sec. 8, the design of the veto detector is presented in Sec. 9, and the details about the data acquisition system and the plan for offline computing are given in Sec. 10 and Sec. 11, respectively. The two ancillary detectors, ReD and DarkSide-Proto, are described in Sec. 12 and Sec. 13. Finally, the design and use of the atmospheric argon cryostat, modeled after the ones deployed for ProtoDUNE, are given in Sec. 14, while the procurement of the underground argon (UAr) target is detailed in the final section, Sec. 15. Note that the following forms a preliminary design for an experiment capable of the stated physics goals, but may change as the technical details evolve in the final engineering stages. DS-20k will be built to operate for a minimum of 10 yr, providing the best sensitivity to high-mass WIMP dark matter.

Energy deposits in the LAr target result in the production of excited and ionized argon atoms, according to the underlying process for recoiling electrons or nuclei. Excited argon atoms, which

can also be produced by recombining ionization charge, lead to an efficient formation of argon excimers decaying via the emission of scintillation light characterized by two decay time constants. Both of the components are combine to yield an instant light signal, called S1. Due to the deep UV nature (around 128 nm) of this scintillation light, which is absorbed by most materials, a thin layer of wavelength shifter, tetrphenyl butadiene (TPB), must cover all exposed surfaces to convert the photons to those of optical wavelengths for detection by photosensors. Ionization electrons escaping recombination are drifted to the top of the LAr by an applied electric field, where an electric field stronger than the field applied to drift the electrons, extracts the electrons into the gas pocket above the liquid. Here the strong field accelerates the electrons, enough for them to excite (but not ionize) the argon gas, producing a secondary scintillation signal S2, proportional to the ionization charge. Photosensors placed behind the wavelength shifter-coated windows at the top and bottom of the TPC, read out both scintillation signals (S1 and S2) of each event. S1 is used for energy determination, as well as for pulse shape discrimination (PSD). The latter is derived from the ratio of the prompt and delayed light fractions. S2 is used for energy and 3D position measurements of the event, the vertical coordinate is measured from the drift time between S1 and S2, and the horizontal coordinates from the light pattern resulting in the top photosensors from S2.

The octagonal LAr TPC will have a height of 350 cm and a distance between parallel walls of 355 cm. It will be instrumented with a new kind of photosensors, arrays of SiPMs, arranged in assemblies called photodetector modules (PDMs). Each PDM has an area comparable to that of a 3" photomultiplier tube (PMT), with the LAr TPC containing 8280 PDMs in total. Substantial effort was put into the development of this technology, since SiPMs promise a higher effective quantum efficiency, higher reliability at LAr temperature, and a much higher radiopurity than PMTs. All of these properties are crucial for DS-20k since the PSD, which is the most important mechanism for background discrimination in LAr, depends critically on the light yield. Additionally, the large material budget of PMTs is often a limiting factor for neutron- and gamma-induced backgrounds. The LAr TPC will be equipped with arrays of SiPMs, totaling 21 m^2 in area.

In comparison to DS-50, where a full digitization and recording of the waveform of each PMT could be achieved, a custom scheme for the sampling of the two-orders-of-magnitude higher channel count of the DS-20k SiPM PDMs has to be developed. Design parameters for the data acquisition (DAQ) system are driven by rates and occupancies, as well as leading edge timing and limited charge information from each channel, while compromising as little as possible on energy resolution and pulse-shape discrimination.

All components of the detector, especially the inner components, like the LAr TPC, the SiPM arrays, and cables, must be made from materials of the highest radiopurity to keep backgrounds as small as possible.

The veto detector consists of three separate volumes:

- An inner volume of active liquid AAr, called the Inner Argon Buffer (IAB), surrounding the TPC;
- A passive shell of acrylic loaded with Gd, called the Gd-loaded Acrylic Shell (GdAS), of octagonal shape mounted around the IAB. The GdAS surrounds the TPC in all directions (lateral, top and bottom, with exceptions due to the signal and utility service holes).
- An outer active volume of AAr, called the Outer Argon Buffer (OAB).

A copper cage which acts as a Faraday cage provides the optical insulation from the rest of the AAr external to OAB and, at the same time, it realizes the necessary electric shield for reducing external noise from contaminating the detector signals. The details of the veto design and expected performance are given in Sec. 9.

In order to demonstrate and test technological developments on a scale relevant to DS-20k, the collaboration will build and operate a $\sim 1\text{ t}$ prototype. The project is called DarkSide-Proto (DS-Proto) and is described in Sec. 13. DarkSide-Proto will be at an intermediate scale between DS-50 and DS-20k, able to test a number of full size components intended for use in DS-20k. The size of DS-Proto was chosen to be able to validate detector and PDM components, including the readout system, both from the mechanical and performance aspects of the experiment. The full size cryogenic system will also be tested in this way, especially the argon condenser, the gas pump,

and the heat recovery system. Functionality and stability control, as well as safety issues during power failures, purification flow rates and general controls are meant to be explored. DS-Proto also serves to validate the readiness of the various production lines in the different institutions of the collaboration to ensure quality control and assurance for the production of components for DS-20k.

For the DarkSide-20k detector to reach its physics goals, a comprehensive plan of calibrations for the LAr TPC and Veto detectors is necessary. The calibration equipment and techniques specific to the DS-20k experiment are described in detail in Sec. 8. In addition to this, it will be important to also utilize measurements taken with external calibration experiments placed within the line of sight of a neutron beam. In the SCENE experiment,[33, 34] a monochromatic, low energy, pulsed neutron beam at the Notre Dame Institute for Structure and Nuclear Astrophysics was used to study the scintillation light yield from recoiling nuclei in a small LAr TPC, but only down to 57.3 keV_{nr}. The ARIS experiment was exposed to the highly collimated and quasimonoenergetic LICORNE neutron beam at the Institut de Physique Nucléaire d'Orsay (IPNO) in order to study the scintillation response to nuclear and electronic recoils [35].

The collaboration is now expanding this external calibration work with a new external calibration experiment, the Recoil Directionality (ReD) experiment, described in Sec. 12. The ReD detector is a small LAr TPC (similar in size to SCENE) equipped with the same SiPM tiles planned for use in DS-20k. ReD is designed to select and measure single neutron elastic scatters on argon nuclei, by means of a large acceptance neutron spectrometer, composed of an array of liquid scintillator detectors. Kinematic requirements of the neutron interactions will allow for the precise detection of nuclear recoils in the LAr, since the neutron energy, scattering angle, and drift field direction can all be precisely measured with the use of external neutron detectors.

5. PHOTOELECTRONICS

Silicon photomultipliers (SiPMs) are one of the key enabling technologies for large-scale LAr-based dark matter experiments. SiPMs will also play an important role in the next generation of LAr-based neutrino detectors, such as DUNE [10], and liquid xenon based detectors for neutrinoless double beta decay, such as nEXO [37]. SiPMs have a number of performance advantages over traditional PMTs, including higher photon detection efficiency (PDE) and much better single-photon resolution, all while operating at much lower bias voltage. SiPMs can also be efficiently integrated into tiles that cover large areas and feature better radio-purity than PMTs.

5.1. PhotoDetector Modules (PDM)

For DS-20k, the photosensing unit will be a “PhotoDetector Module” (PDM), consisting of a large tile of SiPMs covering a total area of $50 \times 50 \text{ mm}^2$ operating as a single detector (see the left panel of Figure 6). Besides the tile, each module will also contain a cryogenic preamplifier board that will amplify and shape the signal in the immediate proximity of the sensor. The output of the cryogenic amplifier will be passed on to a signal transmitter, also integrated into the PDM, and responsible for transmission of the signal through the cryostat penetration. Finally, the PDM will also include the mechanical structure required to assemble all components and to efficiently dissipate heat in the LAr target, minimizing the production of bubbles. An intelligent power distribution system is also foreseen, capable of disabling individual PDMs in case of failure.

The unique challenge in readout presented by SiPMs is mainly due to their capacitance. At 50 pF/mm^2 , a single SiPM with a $5 \times 5 \text{ mm}^2$ surface area passes the nF scale for capacitance. Yet, the experiment foresees a photo-sensing area of 21 m^2 . The readout of a LAr calorimeter faced a similar challenge, with capacitance for the individual cells often passing the nF scale [51]. Early developments on LAr calorimeter readout [52–55] demonstrated that the use of a transimpedance amplifier (TIA) is preferable to a charge integration amplifier where the noise and rise time are very strongly affected by the large detector capacitance. With this in mind, the DarkSide Collab-

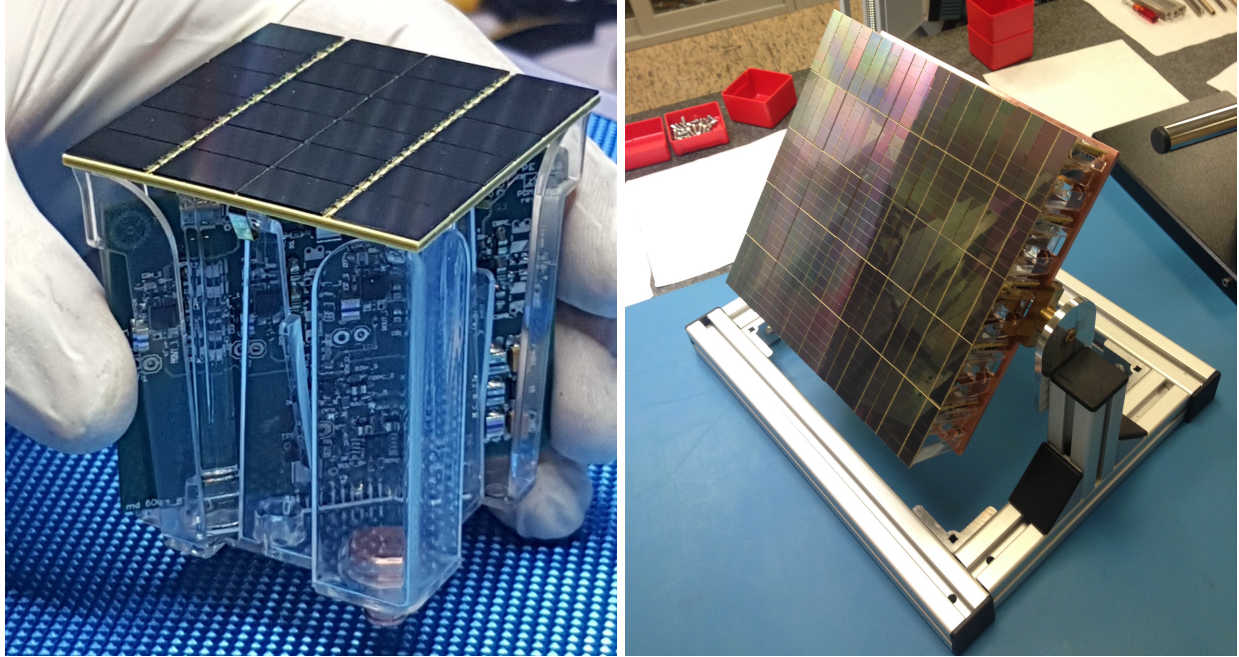


FIG. 6. **Left:** Single channel PhotoDetector Module (PDM) consisting of a $50 \times 50 \text{ mm}^2$ tile of 24 SiPMs and a front-end board. **Right:** The DS-20k motherboard assembled with 25 PDMs.

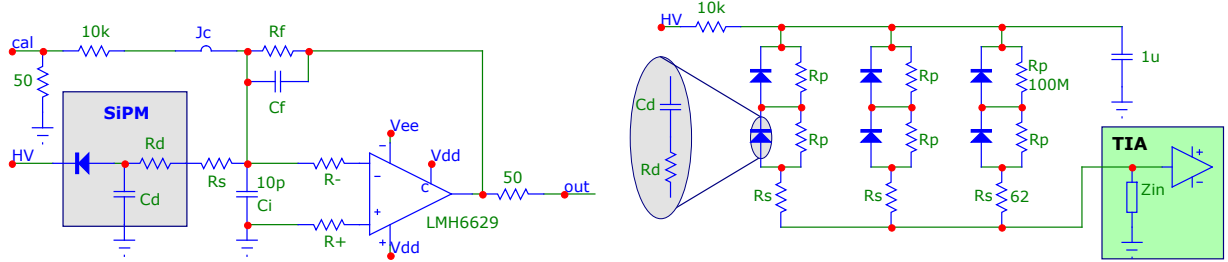


FIG. 7. **Left:** Schematic diagram of the transimpedance amplifier circuit developed to readout SiPMs. **Right:** Schematic diagram of the 2s3p readout scheme optimized for summing six SiPM signal together.

760 oration has developed and optimized a TIA (schematic is shown in the left panel of Figure 7) with
 761 performance at 87 K in mind [25]. The specific goal was to maximize the amplification factor while
 762 preserving a stable signal bandwidth and SNR.

763 The SiPMs readout scheme strongly affects the PDM performance in terms both of SNR and
 764 bandwidth of the signal. A hybrid readout scheme, with parallel-series combination of SiPMs,
 765 first introduced for the MEG experiment [56, 57], solves at once these two problems. In this
 766 configuration, the output signal of an individual SiPM is reduced by a factor equal to the number
 767 of SiPMs put in series, but this disadvantage is offset by the attenuation of the noise gain due to
 768 the reduction in the input capacitance. Most importantly, a strong improvement of the bandwidth
 769 with respect to the parallel readout scheme is achieved, with six SiPMs easily readout by connecting
 770 in parallel three branches of two SiPMs put in series (known as the 2s3p configuration [26], see
 771 right panel of Figure 7) with a bandwidth comparable to the one achievable with a single SiPM in
 772 input. Four such readout quadrants are fit in a single PDM, with their output signals summed at
 773 the transmission stage.

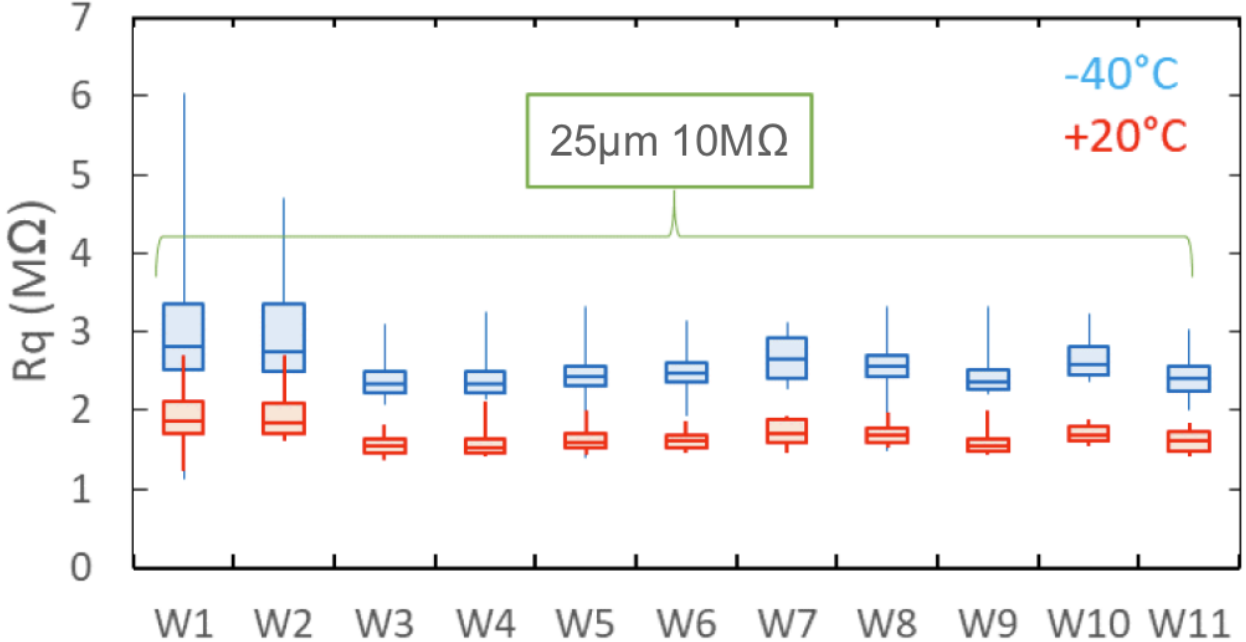


FIG. 8. Average SiPM quenching resistor value vs. wafer number measured at 20 °C and -40 °C.

774

5.2. Signal Transmission

775 The signal transmission from the PDMs to the warm electronics is of primary importance for
 776 the experiment. Given the high number of independent channels, cables would introduce a large
 777 mass in the cryostat with the inherent problems of radio-purity and heat load. The delivery of the
 778 PDM signals to the outside world through optical fibers will solve at once these two problems. For
 779 this purpose an optical analog cryogenic transmitter has been developed. The prototype boards
 780 of the opto-link system (optical driver and optical receiver board) have been recently produced.
 781 The optical receiver board (32 channels) was successfully tested, while the optical driver board (25
 782 channels) is at the moment undergoing testing.

783 The PDMs will be located above the anode and below the cathode, fully covering the top and
 784 bottom faces of the LAr TPC active volume, to detect both the S1 and S2 signals with high
 785 efficiency. The top and the bottom photon readout assemblies will consist of 4140 PDMs each.
 786 Multiple PDMs are mounted to a single motherboard to form two larger basic mechanical units
 787 called the square board (SQB) and the triangular board (TRB), described in Sec. 6.6.1 and shown
 788 in Figure 13. The SQB and TRB have the same edge size of 25 cm. The SQB and TRB are then
 789 used to form the full readout planes (shown in Figure 12). The total number of readout channels
 790 (top and bottom) is 8280.

791

5.3. PDM Fabrication and Characterization

792 Following the successful construction of the first Photo-Detector Module (PDM) in March 2018,
 793 the Photo-Electronics Working Group proceeded to the construction of the first Motherboard,
 794 shown in Figure 6. The FBK company delivered two SiPM runs: the first one with standard doping
 795 SiPMs (cell size $25 \times 25 \mu\text{m}^2$ and quenching resistor $10 \text{ M}\Omega(77 \text{ K})$) and the second one with triple
 796 doping SiPMs (cell size $30 \times 30 \mu\text{m}^2$ and quenching resistor $5 \text{ M}\Omega(77 \text{ K})$). Since the latter SiPM type
 797 is considered the best candidate for the DS-20k experiment, we decided to use the single doping
 798 SiPMs for the first Motherboard construction, so that the triple doping type could be mounted
 799 later, taking advantage of the experience gained with the mounting of the first Motherboard.

800 This SiPM run was characterized by a reasonable yield at -40 °C of about 50 %. A detailed

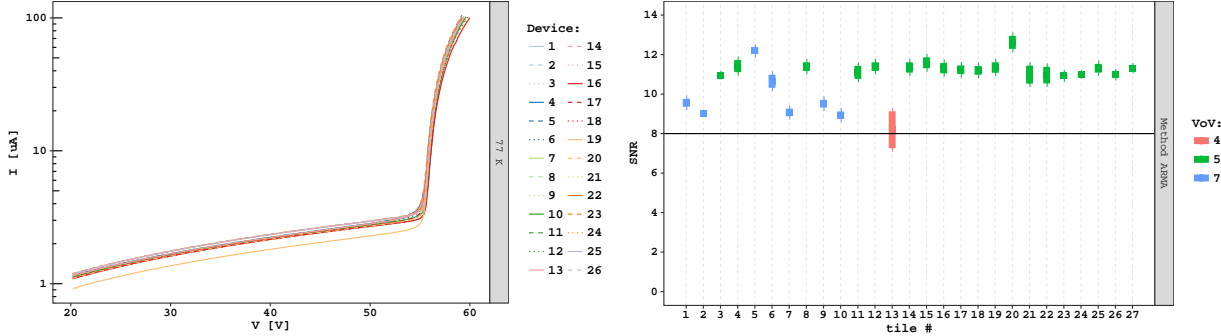


FIG. 9. **Left:** Reverse I-V curves for the SiPM tiles measured at 77K. **Right:** SNR of the 27 bonded SiPM tiles.

801 inspection of the SiPM quenching resistor (R_q) showed good uniformity for most of the wafers,
 802 while the first and the second wafers (W1,W2) had a 20% larger R_q (see Figure 8). The optimal
 803 working voltage of the SiPM is expected to change as a function of R_q , so in the forthcoming
 804 mass production by the LFoundry company, where hundreds of 8" SiPM wafers are scheduled,
 805 this quenching resistor spread is not an issue since the SiPMs with similar R_q can be paired. In
 806 this way, each Motherboard, with PDMs biased at the same voltage, will be made of devices with
 807 similar R_q . Due to the limited SiPMs available in the present production we had to use all of them
 808 to make the first Motherboard, and thus all were biased with a common voltage despite the slight
 809 difference in R_q . As a consequence, the tiles made with SiPMs belonging to wafers 1 and 2 were
 810 fed with an overvoltage lower than the optimal one for some of the SiPMs, i.e. 5 V. It is worth
 811 noting that a dedicated facility for the Motherboard production is not available yet, and therefore
 812 the use of equipment through outsourcing and additional man power was therefore required.

813 The tile and the Front-End Board PCBs were made with an Arlon 55-NT substrate, following
 814 the experience gained during the first PDM construction. The electronic components were mounted
 815 with outsourced equipment, under the supervision of LNGS personnel. The tile PCBs were tested
 816 both at warm and at cryogenic temperatures to verify the correct circuit impedance. After the wafer
 817 dicing, the SiPMs were shipped from FBK to Princeton University, where the first Motherboard
 818 tiles were bonded by personnel from LNGS, Princeton University and TIFPA. A cryogenic epoxy
 819 for the SiPM back-side and a wire-bonding connection for the front-side was used. The 27 tiles,
 820 each made of 24 SiPMs, were then shipped to LNGS, using multipurpose acrylic boxes, designed
 821 by the Pisa group. This box allows for safe shipping of the tile, offering an adequate protection of
 822 the SiPM wire bonding and, at the same, time allows the tile characterization in liquid nitrogen
 823 by permitting the insertion of the Front End Board without removing the tile from the box. The
 824 tiles underwent a comprehensive test at LNGS both at warm temperature and in LN, including the
 825 reverse I-V curve measurement, the power spectrum and the charge spectra. We found just one
 826 tile out of the 27 with two SiPM branches (4 SiPMs) not working properly. Another tile showed
 827 a noise level higher than the average. These two tiles were therefore excluded from the list of the
 828 tiles selected to populate the first Motherboard.

829 As an example, the left side of Figure 9 shows the tile I-V curves taken at 77K, indicating a
 830 homogeneous behavior.

831 The right panel of Figure 9 shows the signal to noise ratio (SNR) for the 27 tiles at their
 832 optimal voltage. It is worth noting that all of them have a SNR larger than the minimum SNR
 833 of 8, required by the DarkSide-20k experiment specifications. For each tile, the SNR was obtained
 834 relying on several different procedures and analysis methods. The bar length in the figure represents
 835 the spread of each measurement, depending on the method used. The signal-to-noise ratio (SNR)
 836 is defined as the ratio between the gain and the width of the baseline noise peak. The gain is
 837 measured by fitting the center values of the amplitude multiple peaks and evaluating the slope of a
 838 linear fit. The baseline noise is extracted from the average standard deviation of the waveform in a
 839 pre-pulse window, 500 ns long, using 500 samples. For most tiles, the distribution of the standard
 840 deviation is not symmetric around the peak. The most important contribution to the noise baseline

841 is the presence of one or more photoelectrons not stimulated by the laser pulse. These can originate
842 from a SiPM having an excess of dark-rate or more probably by an excess of after-pulsing.

843 Since the distribution is not symmetric, the estimate of the baseline noise is intrinsically biased
844 and two options are possible, corresponding to the mean value or the most probable value (mode).
845 Consequently the SNR is defined in a confidence interval between $\text{SNR}_{\min} = \text{gain}/\text{noise}_{\text{mean}}$ and
846 $\text{SNR}_{\max} = \text{gain}/\text{noise}_{\text{mode}}$.

847 Figure 10 shows the SNR obtained with the common over-voltage of 5 V. Although a few tiles, as
848 expected, manifest a SNR slightly below 8, the SNR is quite good for all tiles used in the assembly
849 of the first Motherboard.

850 5.4. Motherboard Assembly

851 Before assembling the first Motherboard, a full mock-up made of an aluminum Motherboard
852 structure, an FR4 Motherboard strip PCB, 25 dummy tiles and FEBs, and the PDM acrylic
853 mechanics was mounted at Bologna. Each PCB had the same dimensions of the final one, while
854 the HV/LV and signal layers were not included in the stack-up. The mounting required just a few
855 hours and the overall procedure was validated, while the mechanics of the different components
856 nicely merged, suggesting just a few minor mechanical improvements.

857 After these tests, the tiles were finally shipped to Pisa, while the PDM pillars and the copper
858 Motherboard structure were milled at Bologna using 99.997 % pure copper sold by the Luvata
859 Company. The first Motherboard was equipped with a PCB strip connecting the PDMs, made of
860 a thin stack-up (0.5 mm) based on a Pyralux substrate and shipped to Pisa to start the mounting
861 of the 25 PDMs on the Motherboard.

862 The PDMs were assembled in the Pisa clean room, following the prescriptions used for the first
863 PDM, assembled in March 2018. The mounting of the 25 PDMs on the Motherboard was finalized
864 in few days. A picture of the first Motherboard, fully equipped with the first 25 PDMs is shown in
865 the right panel of Figure 6.

866 In summary the construction of the first Motherboard required the production, testing, selection
867 and bonding of more than 600 SiPMs. Although a cryogenic probe and an automatic bonder were
868 not available yet, the Collaboration was able to increase the number of successfully built PDMs
869 from 1 to 25, in just 6 months. The bonding yield exceeded 95 % (just 1 tile out of the 27 showed
870 problems with the SiPM bonding strategy), while the satisfactory PDM SNR demonstrated the
871 validity of the full Motherboard construction process.

872 After the completion of the first motherboard, equipped with 25 PDMs each containing 24 single
873 dose SiPM's, the collaboration moved to the construction of a second Motherboard, equipped with
874 triple dose SiPMs. At the moment, half of the PDMs have already been assembled and mounted
875 in the copper structure. The remaining PDMs will be mounted within the summer of 2019. The
876 FEBs were already successfully tested, while the SiPM tiles are currently undergoing testing in
877 LN. The next step in the photo-electronics schedule is the production of about 400 PDMs for the
878 DS-Proto detector. These SiPMs will be produced by the LFoundry Company in Avezzano, Italy.
879 The first run is expected in the summer of 2019.

880 5.5. Mass Production

881 The first engineering run, finalized in September 2018 and tested shortly after, showed the
882 capability of the silicon foundry to implement the FBK technology. The produced SiPMs showed
883 good performance at both room temperature and in liquid nitrogen. A second LFoundry engineering
884 run, presently ongoing, is devoted to the development of the through silicon vias (TSV). This post-
885 production rework requires some delicate mechanical manipulation of the SiPM wafers.

886 The DS-20k SiPM packaging foresees the production of more than 10 000 PDMs in 2.5 yr. This
887 remarkable effort requires a large clean room, relying on cutting edge technology equipment and

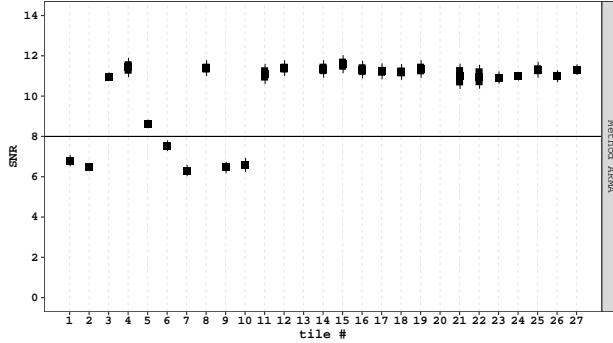


FIG. 10. SNR of the 25 SiPM tiles populating the first motherboard while operating the SiPM tiles at an over-voltage of 5 V.

888 trained personnel. The GADM selected for the NOA DS-20k SiPM packaging facility a clean room
 889 at the *Tecnopolo dell’Aquila*, with surface exceeding 700 m². The clean room will be soon refurbished
 890 to comfortably host the needed equipment and personnel. This facility will be managed by GSSI,
 891 through an agreement with INFN that will soon be finalized. Concerning the procurement of the
 892 equipment for the DS-20k PDMs mass production, the cryogenic probe tender was just approved
 893 by the INFN Executive Board and the flip-chip bonder tender will follow in the weeks to come.

894

6. INNER DETECTOR AND CRYOGENICS SYSTEM

895

6.1. DS-20k LAr TPC

896

The DarkSide-20k LAr TPC is the dark matter detector and the central element of the experiment, with all auxiliary detectors and systems specified and designed in support of it. The DS-20k LAr TPC will use 50t of LAr extracted from an underground source as the target material for WIMP detection. An ultra-pure acrylic vessel is used to contain the LAr. Features directly fabricated onto the inner surfaces of the acrylic vessel will form the TPC itself. These features are the TPC field cage system, the anode and the cathode and are implemented on the acrylic panels with a commercial conductive polymer coating, called Clevios™. Use of this coating eliminates the use of metal conductive materials.

904

The same pure acrylic material, in the form of 4 mm thick sheets, is used to hold the Enhanced Specular Reflector (ESR) reflector foils installed to maximize light collection. The TPC is designed such that all the inner surfaces facing the active volume are coated with TPB, a wavelength shifter, to ensure the complete conversion of the 128 nm argon scintillation light to 420 nm, where the SiPMs’ peak in their PDE. Two identical photosensor arrays of 4140 channels each are placed on top and bottom of the TPC, but outside of the acrylic vessel. The TPC is mounted inside a neutron veto detector, whose most important component is a 10 cm thick, gadolinium loaded, acrylic shell that completely encapsulates the TPC. This plastic shell defines two 40 cm thick active volumes, respectively named the inner and outer buffer, filled with liquid Ar. The buffers are further segmented with ESR, also coated with TPB. The whole apparatus is placed inside a light and electromagnetic shield barrier, contained in the ProtoDUNE-like cryostat filled with Ar.

915

Sealed PMMA Vessel: An acrylic (PMMA) vessel will be used to confine the UAr rather than a metallic vessel, since PMMA is extremely radiopure, resulting in a residual neutron background estimated to be $<10^{-3}$ for the exposure of 200 t yr. As described above, the TPC active volume is confined in all directions by the sealed PMMA vessel that is formed by bonded plates or panels. In order to use the UAr more efficiently, all the UAr will be sealed in this PMMA vessel, so that no other external vessel will be required (as shown in Figure 11). The body of the PMMA vessel will be fused together by 5 cm thick acrylic plates, and then flanged and sealed with the top and the bottom lid, that serve as the anode plate and cathode plate of the TPC, respectively.

DS-20k TPC Dimensions	
TPC Drift Length	350 cm
Octagonal Inscribed Circle Diameter	355 cm
Total LAr Mass	51.1 t
Active LAr Mass	49.7 t
Fiducial Cut Distance (vertical)	70 cm
Fiducial Cut Distance (radial)	30 cm
Fiducial LAr Mass	20.2 t
Nominal TPC Fields and Settings	
Drift Field	200 V/cm
Extraction Field	2.8 kV/cm
Luminescence Field	4.2 kV/cm
Cathode Voltage	-73.8 kV
Extraction Grid Voltage	-3.8 kV
Anode Voltage	ground
Gas Pocket Thickness	7 mm
Grid Wire Spacing	3 mm
Grid Optical Transparency	97 %
SiPM PDM	
Number of PDM on TPC Top	4140
Number of PDM on TPC Bottom	4140
PDM Effective Area	50 × 50 mm ²

TABLE III. DS-20k LAr TPC detector parameters.

923 The ESR-acrylic reflector panels are located inside the acrylic vessel. The top and bottom PDM
 924 arrays are placed outside of the acrylic vessel, immersed in the AAr of the neutron veto detector.
 925 PDM arrays will be isolated from any light generated in the veto detector. In this way, 97.3 % of
 926 the total argon is active, resulting in the most efficient usage of UAr. All cables, HVFTs, and most
 927 mechanical structures are moved outside of the UAr volume as well, resulting in less outgassing
 928 and hence higher purity of the UAr.

929 The HV Cathode connection through the acrylic vessel is being studied and a new design will be
 930 tested to adapt the cable connection to the cathode itself. The acrylic vessel design integrates the
 931 HV connection so that the contact point is outside the vessel. In this case, both the HV cable and
 932 the HVFT are in the AAr volume. The HVFT will penetrate through the veto cryostat.

933 A commercial conductive and transparent Polymer coating, Clevios™, is found to be a very
 934 promising alternative to the traditionally used indium tin oxide (ITO) thin film coating. Clevios™
 935 is being used in industrial applications such as transparent electrodes for touch panels and printed
 936 electronics. The main advantage of Clevios™ is its composition. Being a water-based solution, the
 937 large-area coating needed for the anode and cathode will be easier to accomplish with respect to an
 938 ITO coating. A sample of 100 g has been procured for the radioactivity assay. The initial ICP-MS
 939 assay results from PNNL are encouraging, and further analysis of Rn emanation is scheduled at
 940 Krakow. In terms of the optics, three coating samples of Clevios™ on acrylic plates were provided
 941 by The Heraeus Company. The wet coating thickness of each sample is 4 µm, 8 µm and 12 µm,
 942 respectively, and their transparency has been measured at Princeton University. A 1.5 % absorption
 943 at 420 nm was observed for a 4 µm thick Clevios™ layer, which is a good result comparable to
 944 the 98 % transparency of ITO measured in DS-50. Further studies, including coated thickness
 945 resistivity, TPB coating on Clevios™, and durability in LAr are ongoing. Besides the anode and
 946 cathode, the new design replaces the bulky copper field shaping rings with Clevios™ conductive
 947 coatings. Consequently, the use of this polymer will reduce the expected background, as well as
 948 the total cost, and make the fabrication and installation of the TPC simpler.

949 **LArTPC Size Consideration:** Since the SiPM tiles are all square shaped, the DS-20k TPC
 950 will be an octagonal shape to best fit the coverage of the PDM, while optimizing the fiducial mass.
 951 The size of the TPC is determined by the patterning strategy of the SiPMs, driven by the design
 952 size of the square and triangular motherboards (SQB and TRB, respectively). Figure 12 shows
 953 the current SiPM pattern strategy for both the top and bottom arrays. Each array consists of 156

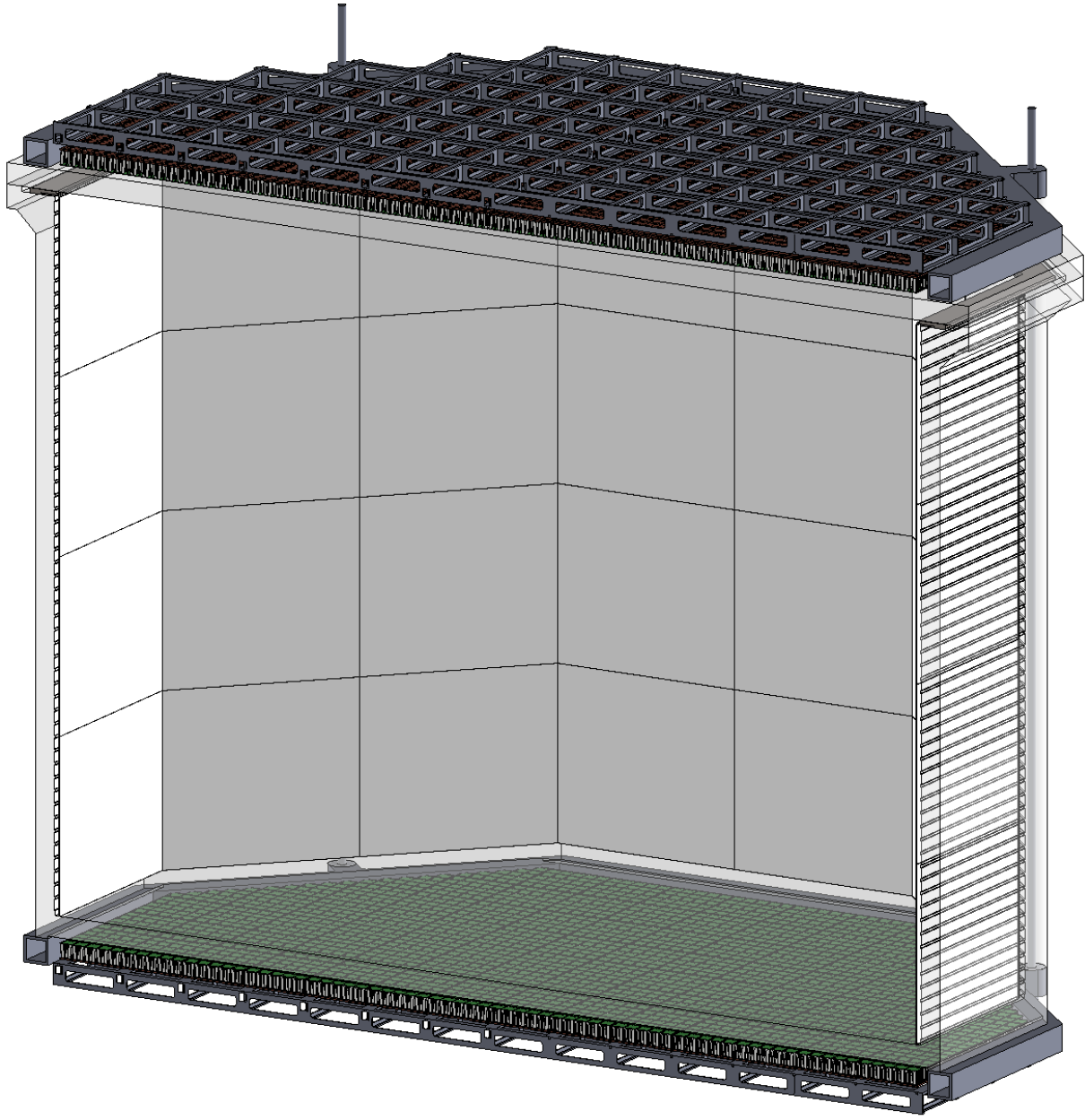


FIG. 11. Artist rendering of the PMMA vessel and the TPC.

954 SQBs and 16 TRBs. Each TRB contains 15 PDMs and each SQB contains 25 PDMs, as shown
 955 in Figure 13. Thus, the number of PDMs used in each array is 4140, while the total number
 956 envisioned in the TPC is 8280. Based upon this pattern strategy, and considering that the edge
 957 of the active volume of the TPC will shrink about 2.7 cm from the edge of the SiPM array, the
 958 distance from edge to edge of the octagonal active volume will be 355 cm. The height of the TPC
 959 will be 350 cm. With this design, the total mass of LAr in the active volume and fiducial volume
 960 (with 70 cm vertical and 30 cm lateral cuts) are 49.7 t and 20.2 t respectively.

961 **Reflector Panel:** In order to get rid of the conventional PTFE reflectors, which would be the
 962 predominant source of neutron background and Cherenkov background due to the enormous mass
 963 required for DS-20k, ESR foils will be used as the TPC reflector. The ESR is a thin layer foil which
 964 has reflectivity of 98 % for 420 nm light, with a thickness of only 50 μm . In order to hold the ESR

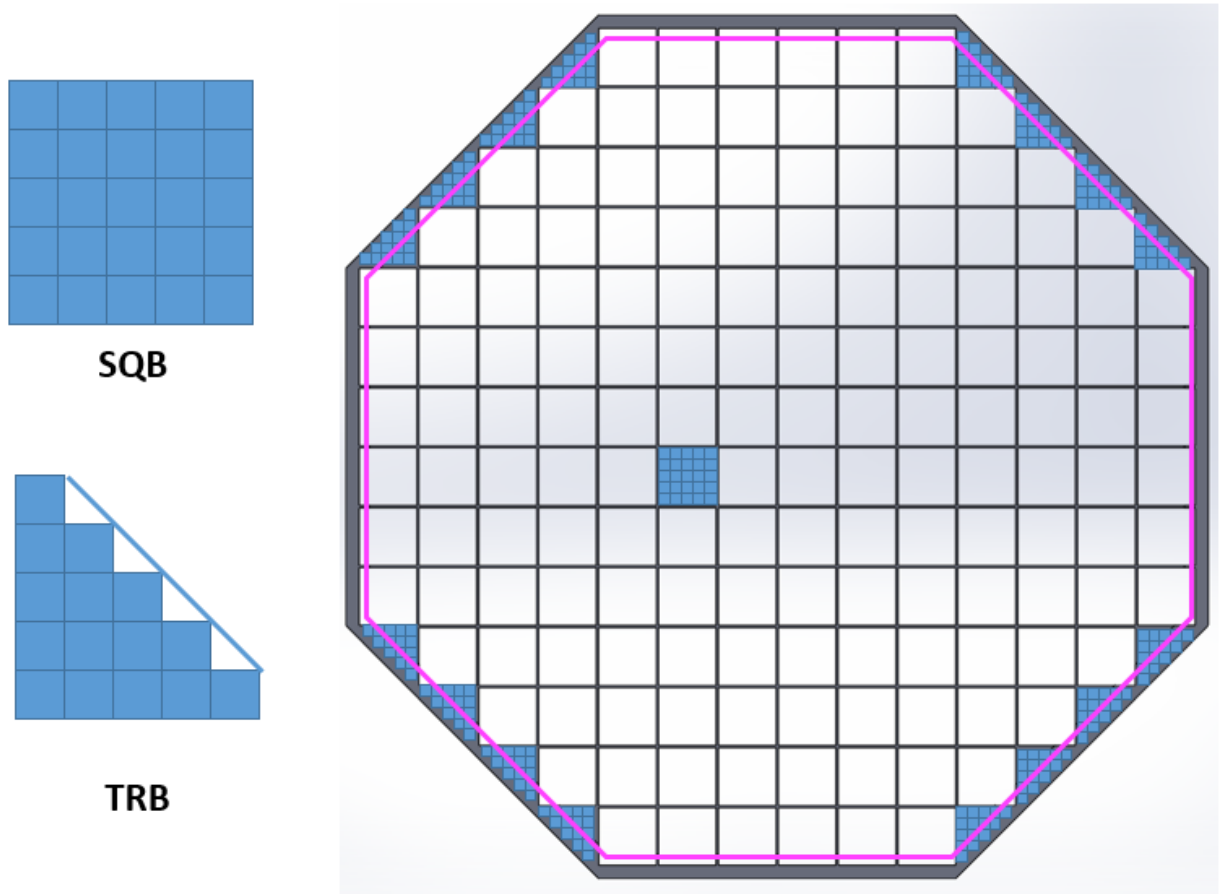


FIG. 12. Patterning scheme for the PDMs. Pink lines indicate the edges of the TPC active volume.

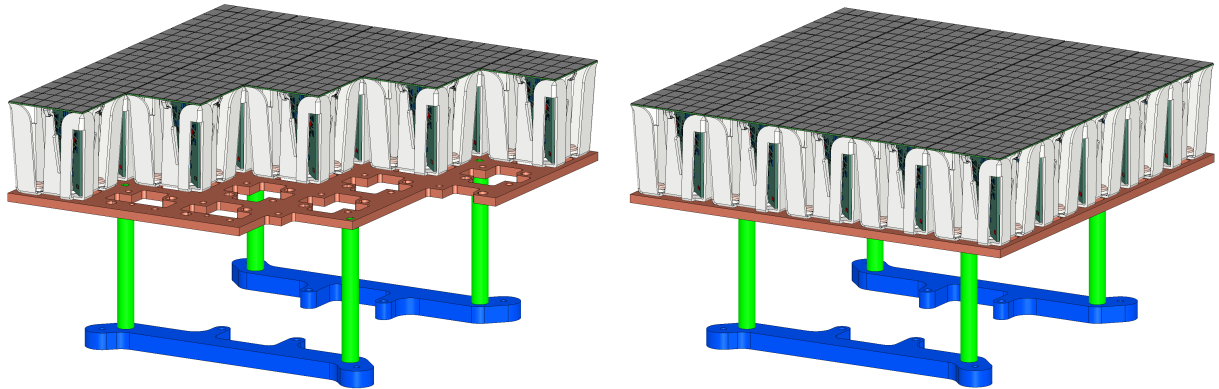


FIG. 13. Schematic drawings of the two types of DS-20k PDM motherboard arrangements. **Left:** triangular with 15 PDMs arranged for center and edge placement. **Right:** square with 25 PDMs.

965 foils in place and maintain their flatness during the operations, 4 mm thick UVT acrylic sheets will
 966 be used. The thickness of the backside acrylic sheet is chosen to be 4 mm, providing the panels
 967 with enough strength to maintain the flatness of the ESR foils. The surface of each ESR foil facing
 968 the active LAr volume will be coated with TPB.

969 The entire reflector panel of the TPC is shown in Figure 14. The ESR mountings are strategically
 970 arranged such that no gaps can develop during the cool down of the TPC, hence guaranteeing 100 %

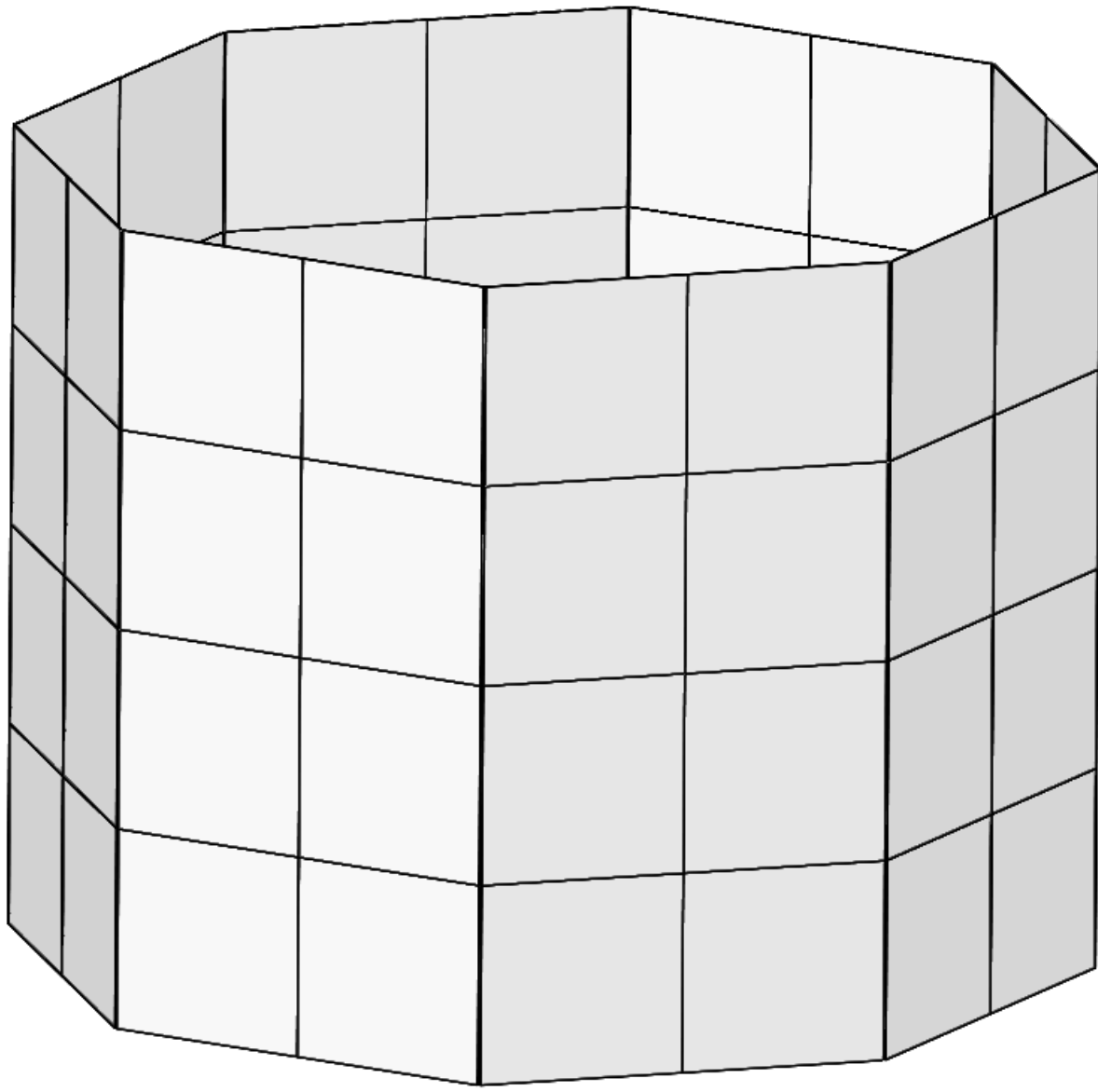


FIG. 14. 3D model of the full DS-20k LAr TPC reflector panels system.

971 TPB coverage. Each ESR-acrylic sub assembly will be fixed by several acrylic screws, with the screw
 972 heads facing the active volume. To avoid losing any light, each head of the screw will also be coated
 973 with TPB. By design, some space is left between the acrylic and the ESR to allow venting of any
 974 gas during the filling with LAr, but also to allow the LAr to fill the space between the back of the
 975 ESR and the acrylic panel. The flat and corner assemblies will be mounted on the field cage, which
 976 is attached to another set of acrylic structures by PTFE screws. The ESR holding panels are not
 977 connected at the corners in order to accommodate the shrinkage when the assemblies are cooled to
 978 LAr temperature. Overlaps between ESR foils at each joint are also designed for the same reason.
 979 A small mock-up to mimic the shrinkage has been built at UC Davis, whose results have confirmed
 980 the design concept. Repeated tests in liquid nitrogen showed that all parts moved in the desired
 981 way during cooling down and warming up, which proves the design idea.

982 **Field Region:** Within the sealed acrylic vessel, the electrode features of the TPC are realized
 983 using the CleviosTM conductive polymer coated directly onto the acrylic vessel. The inner surface

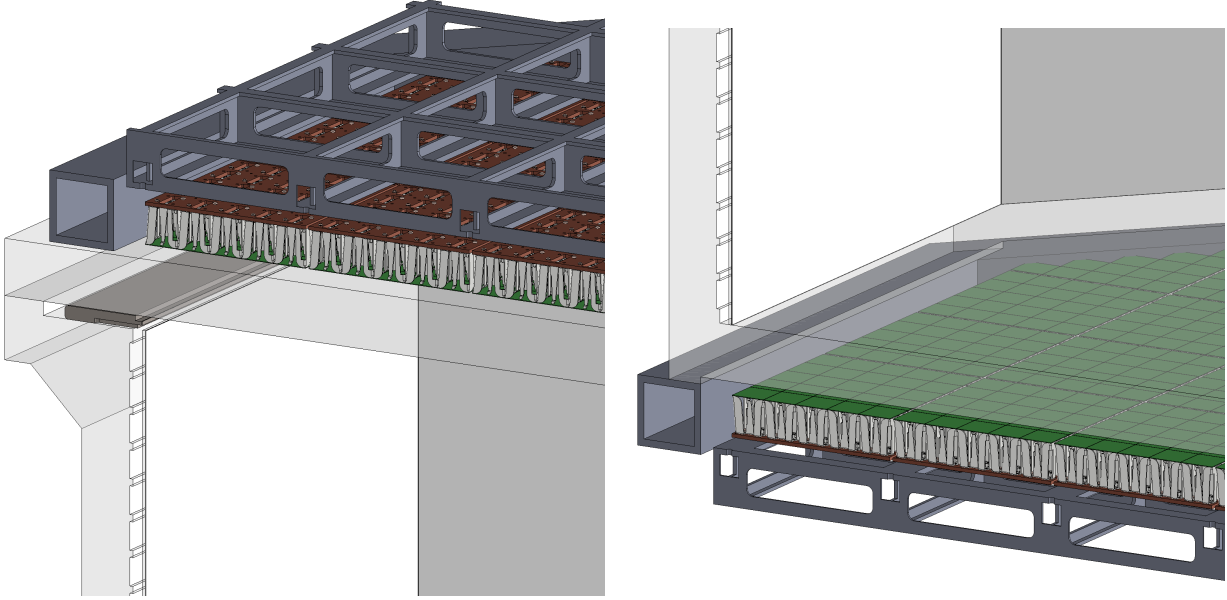


FIG. 15. **Left:** 3D model of the LAr TPC anode and extraction grid region. **Right:** 3D model of the LAr TPC cathode region.

984 of the acrylic vessel will be machined with grooves such that recessed areas have geometries similar
 985 to an electrode ring, and when coated with the Clevios™ comprise the TPC field-shaping rings
 986 that are highly uniform across the height of the TPC.

987 The relative permittivity of LAr and GAr are 1.54 and 1.03, respectively. By applying electric
 988 potentials of zero, -3.8 kV , and -73.8 kV to the anode, extraction grid and cathode, respectively,
 989 three different field regions are formed in the TPC:

- 990 • The uniform drift field of 200 V/cm in the liquid phase, formed by the geometry of the field cage.
 991 The drift distance between the cathode Clevios™ layer and the extraction grid is 350 cm ;
- 992 • The extraction field in the liquid phase above the grid is 2.8 kV/cm . The distance between the
 993 extraction grid and the surface of the LAr is 3 mm ;
- 994 • The electroluminescence field in the gas phase is 4.2 kV/cm . The gas gap between the surface of
 995 the LAr and the Clevios™ layer acting as the anode is 7 mm thick.

996 These values are based on the settings used for DS-50, while since the DS-20k gas pocket will be
 997 operating at a higher pressure, the extraction and luminescence fields will be scaled by the ratio of
 998 the electric field to the pressure of the gas pocket. The final values to be used will be confirmed with
 999 the DS-Proto detector that is designed to confirm final design choices for the DS-20k LAr TPC.

1000 As the top boundary of the active volume, a 5 cm thick acrylic window serves as the diving bell
 1001 to maintain a stable gas pocket. A thin layer of Clevios™ conductive polymer is coated on the
 1002 inner surface to act as the anode and a layer of TPB coated onto the Clevios™ layer to shift the
 1003 scintillation light wavelength. The Clevios™ layer coating geometry is optimized for gas pocket
 1004 electroluminescence field uniformity, as shown in the left panel of Figure 15. Right below the liquid
 1005 surface is the extraction grid, composed of stainless steel wires (not shown in figure) stretched in
 1006 parallel with 3 mm spacing and held in place via small posts set into a stainless steel frame. Slots
 1007 going in the radial direction and on the rim of the acrylic diving bell act as a concentric guide,
 1008 to compensate the different thermal expansion coefficients between the acrylic and stainless steel
 1009 while maintaining precise alignment. The LAr level will be maintained at the top surface of the grid
 1010 frame. Suitable tensions will be pre-loaded on each of the grid wires to minimize the sagging, an
 1011 effect that would distort the electroluminescence field. The frame must be stiff enough to sustain
 1012 the total tension load of all wires, while having as little mass as possible. Both simulation studies
 1013 and prototyping tests are well underway and have presented a feasible design for the extraction
 1014 grid.

1015 The bottom boundary of the active volume, shown in the right panel Figure 15, is a 5 cm thick
1016 acrylic window coated with a thin layer of Clevios™ on both sides. A layer of TPB will be coated
1017 on the top Clevios™ layer for wavelength shifting. The edge of the top Clevios™ layer is in
1018 contact with a C-profile feature on the walls of the acrylic vessel, which acts as a field shaping
1019 ring and smooths the electric field lines in the corner of the cathode region. Similarly, the bottom
1020 Clevios™ layer is in contact with a smoothing-profile solid guard copper ring to provide connection
1021 for the ground bias and electric field minimization. The 5 cm thick acrylic window can easily sustain
1022 the applied electric field with this design. Figure 16 shows the full field mapping modeled with
1023 the COMSOL Multiphysics software. Since the vessel is sealed, there is no path for HV to break
1024 through the acrylic at the cathode region. To confirm this, a full scale mock-up will be built to
1025 confirm the cathode HV delivery method around the acrylic vessel bottom. The bottom surface of
1026 the cathode acrylic window will have a convex shape to avoid bubble accumulation. Any bubbles
1027 generated by the bottom photon detector array, or any other parts, will be driven outwards and
1028 rise to the top of the AAr cryostat.

1029 A one tonne-scale prototype with full features of the DarkSide-20k TPC will then be built to
1030 validate the design comprehensively. General considerations, such as the requirements of surface and
1031 bulk contamination, coating procedures, handling and bonding of acrylic, are based on knowledge
1032 available within the GADMC. Detailed plans and procedures are currently being developed. All
1033 mock-up designs and tests will use final DS-20k geometries and full size components in order to
1034 confirm the validity of the final DS-20k mechanical design and functional parameters. The DS-20k
1035 LAr TPC parameters are summarized in Table III.

1036 6.2. Cryogenics

1037 The main system parameters of the cryogenics system are given in Table IV. The parameters
1038 that are listed in bold are considered to be system requirements, most often driven from experience
1039 gained during operations of the DS-50 cryogenics system.

1040 The cryogenics system is derived from the successful scheme of the DS-50 cryogenics and gas
1041 handling system. Additional lab tests, already performed over the past 4 years, demonstrated
1042 individual or integrated features required for the performance of the control system and the safety
1043 of the large amount of UAr in the DarkSide-20k system. A full P&ID diagram is already developed
1044 as shown in Figure 17. There are two major linked systems: one for the AAr in the veto shield
1045 inside the ProtoDUNE cryostat and one for the UAr in the sealed acrylic vessel for the LAr TPC.
1046 The AAr cryogenics system can be the same as the demonstrated ProtoDUNE system already
1047 built at CERN, or an optimized version specific for the LNGS installation. The UAr cryogenics
1048 system for the TPC will be an upgraded system based on DS-50. The ProtoDUNE cryostat is a
1049 passively insulated system so that its thermal load is not subject to the availability of the electric
1050 power. Liquid nitrogen is the primary cooling source of the entire cryogenics system. A minimum
1051 storage of the liquid nitrogen is maintained such that the system will be protected during power
1052 failure mode. A full scale version of the condenser box for the underground argon has already been
1053 designed and all parts procured. The cryogenics test of the condenser is planned at the CERN
1054 cryogenic division in summer 2019.

1055 Heat exchangers are strategically placed throughout the system for LAr filling and LAr removal at
1056 the various required speeds for the different operational modes. The continuous argon circulation for
1057 purification is driven by a set of specialized gas argon pumps (developed within the collaboration).
1058 Combined with the integrated heat exchanger systems, the system can handle high circulation
1059 rates (10 000 std L/min AAr, and 1000 std L/min UAr) drawing either, or both, liquid and gas
1060 phase argon to effectively remove electronegative impurities. The designed P&ID system allows
1061 the use of SAES hot getter to effectively remove N₂, CO₂, and O₂. The total cooling power of the
1062 cryogenics system is designed to handle the total heat load from the power dissipated by the cold
1063 electronics operating inside the liquid argon volume.

1064 The cryogenics system for the LAr TPC in DS-20k shares the same principle as that fully demon-

Parameter	Value
ProtoDUNE Cryostat parameters for AAr	
ProtoDUNE Cryostat inner width	8548 mm
ProtoDUNE Cryostat inner height	7900 mm
LAr height in ProtoDUNE Cryostat	7500 mm
Total AAr in ProtoDUNE Cryostat	700 t
ProtoDUNE Cryostat insulation per unit area	6.5 W/m ²
Thermal Heat Load of ProtoDUNE Cryostat	2.7 kW
TPC PDM Cold Electronics Power	1.5 kW
Veto PDM Cold Electronics Power	0.5 kW
AAr System Design Mass Circulation Speed	10 000 std L/min
Minimum heat recovery efficiency of AAr heat exchanger	>95 %
AAr Turn Over Time	30 d
Total Cooling Power Required	10 kW
LAr boiling threshold at 3 m depth	60 mW/cm ²
Minimum AAr condenser cooling power to hold LAr inventory	2.7 kW
ProtoDUNE AAr top pressure	1.075 bar
TPC Cryogenics Parameters for UAr	
Total UAr mass during normal operation	51.1 t
TPC UAr Cryogenics Design Mass Circulation Speed	1000 std L/min
Minimum heat recovery efficiency of UAr heat exchanger	>95 %
UAr Turn Over Time	20 d
Total Cooling Power Required for UAr	500 W
UAr Turn Over Time	20 d
UAr electron lifetime required for stable S2 generation	>5 ms (<0.01 ppb O ₂ equiv.)
Pressure stability achieved in DarkSide-50	0.023 psi (RMS)
Nominal flow rate of single DarkSide-20k GAr circulation pump	500 std L/min
Total mass of LN ₂ storage in cooling system	30 t
Efficiency of radon purification by activated charcoal trap	<2 μ Bq/kg after trap
Maximum required helium leak rate at all welds and joints	2×10^{-9} std cm ³ /s

TABLE IV. DarkSide-20k cryogenics system parameters.

strated in DS-50, which has been running smoothly for five years. The long-term TPC pressure stability, an essential parameter for S2 resolution, has been achieved with incredible success, quantified as 0.023 psi RMS. A drift electron lifetime of \geq 5 ms has been achieved, resulting in an oxygen contamination in LAr of less than 0.01 ppb, which is greatly beneficial to the low-mass dark matter search, as recently published in [7, 8]. The immunity to total power failure (including UPS system failure), as tested in the commissioning phase and verified by a recent accident of total LNGS blackout, secures the safety of the entire LAr TPC, especially the valuable UAr.

The features of the DS-50 cryogenics system are fully implemented into the DS-20k system, not only by simply scaling up the argon volume, but also upgrades based on experience and lessons learned. A major improvement is to increase the circulation speed to the required 1000 std L/min, to initially reach the purity requirement of LAr in a couple of turn-over times of 20 d. Another major improvement is to increase the cooling power needed to accommodate such a large circulation speed. A full-size prototype LAr condenser, the core component in the cryogenics system, has been built and tested at UCLA, and a cooling power of 2.2 kW (latent heat only) has been achieved, nearly twice that needed for the DS-20k UAr cooling requirement. The main components of the UAr cryogenics system condenser box have already arrived at CERN and are ready for welding and the first test to follow in summer 2019.

The UAr cryogenics system is made up of several sub-systems (while the AAr system will be similar except at larger scale in volume and power, but with lower requirements on purity): the liquid argon handling system, the liquid nitrogen reserve system, the purification system, the cold box, the gas circulation pump, the recovery and storage system, the integrated heat exchanger system, and heat exchangers close to the TPC. The overall schematic is shown in Figure 17,

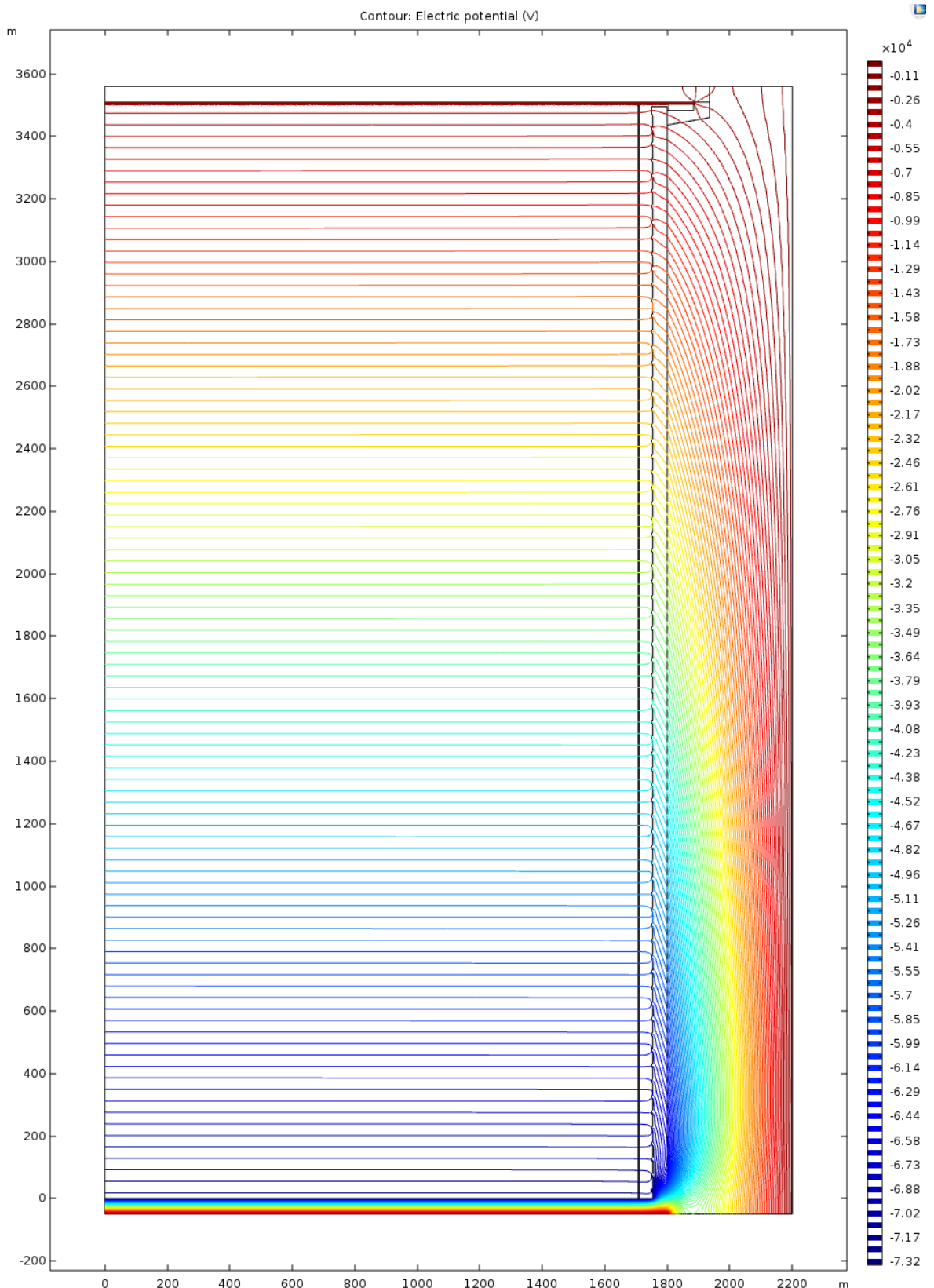


FIG. 16. Equipotential lines mapping in the DS-20k TPC showing an extremely uniform field distribution, modeled with the COMSOL Multiphysics program. Parameter settings for the calculation are those defined in Table III.

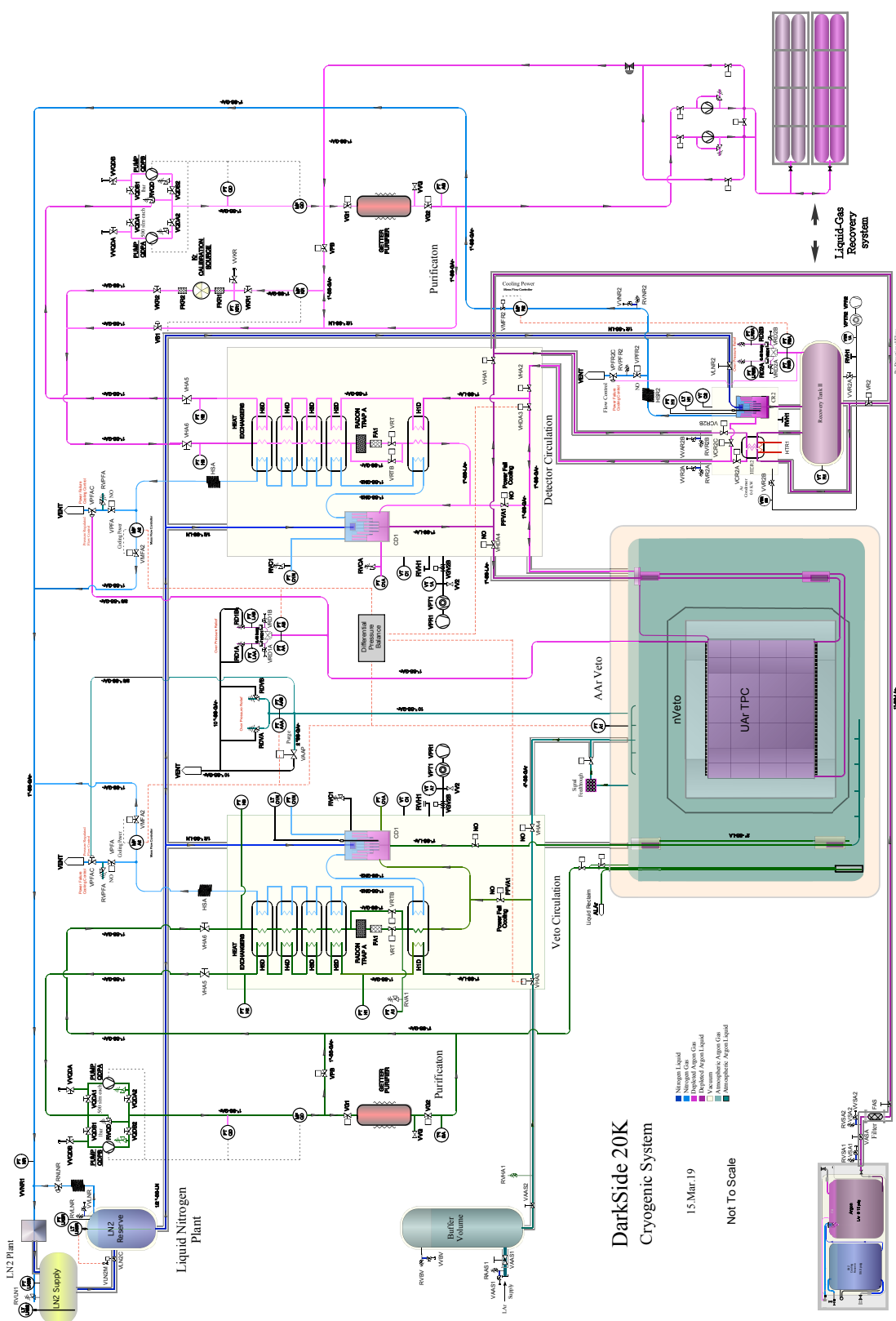


FIG. 17. DS-20k cryogenics system P&ID.

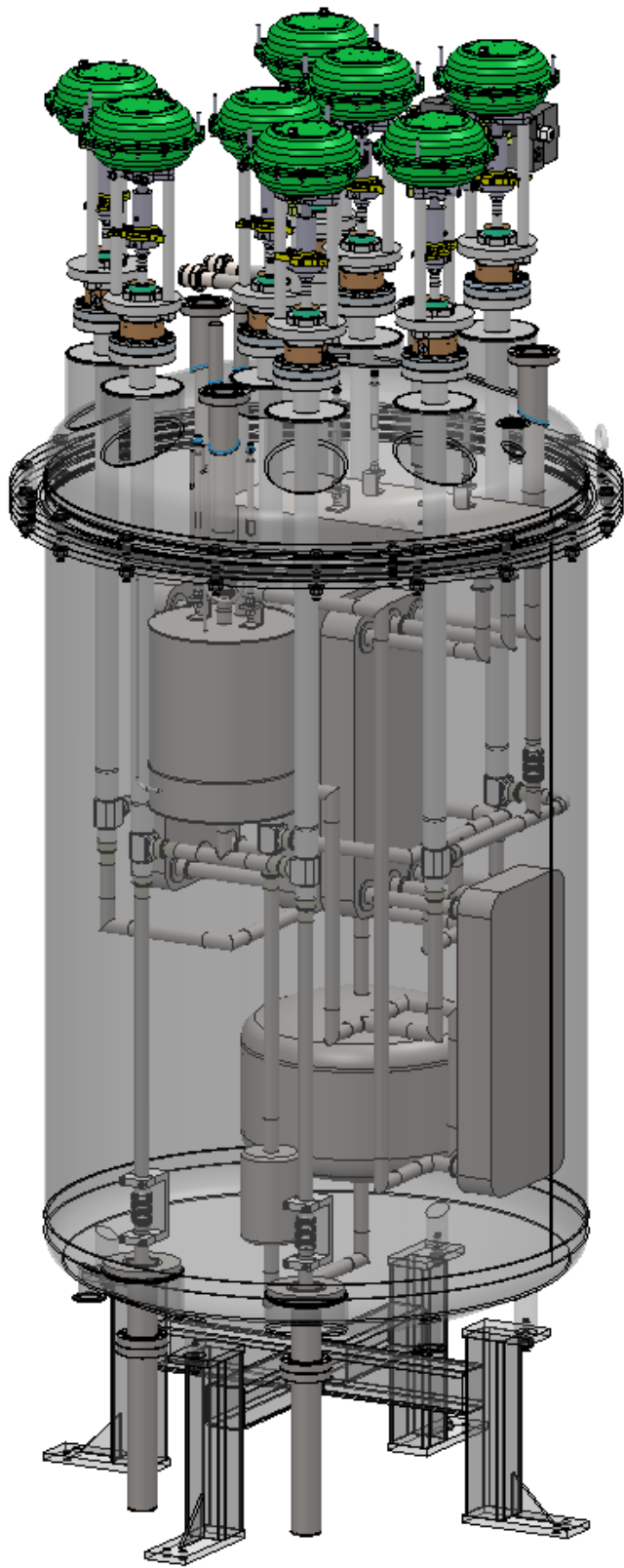


FIG. 18. DS-20k condenser box.

1087 including the AAr cryogenics system for the veto detector, which employs the same principle. Two
1088 cryogenics systems share the same liquid nitrogen reserve loop, but have separate argon loops of
1089 UAr and AAr, respectively. Also shown in the figure is the condenser box integrated with the heat
1090 exchangers and inline radon trap.

1091 The LAr handling system delivers the clean radon-free UAr, which is initially stored in the
1092 recovery storage system capable of storing the full target of UAr for DS-20k. Two options are
1093 being considered, full liquid phase storage or gas phase high-pressure storage. The gas handling
1094 system will be adopted to either solution in order to pre-purify the UAr before filling the TPC
1095 volume. The system is also designed such that the UAr can be recuperated from the inner detector
1096 to the recovery system, as needed, if an emergency occurs or at the end of the experiment.

1097 The LN₂ reserve system is a closed loop with a LN₂ plant located outside of Hall C and a few
1098 local liquid nitrogen dewars. The system delivers liquid nitrogen as the source of cooling power to
1099 the condensers in the inner detector UAr cryogenics system, the AAr cryogenics system, and the
1100 recovery system, if liquid phase storage is chosen, and recuperates the boiled-off nitrogen gas to
1101 liquify it back into the LN₂ system. The UAr purification system purifies the argon in gas phase
1102 during the circulation. A commercial SAES getter system has already been proven to work well in
1103 DS-50 and an identified model with increased circulation capability will be used in DS-20k.

1104 The cold box, as shown in Figure 18, is one of the key components of the DS-20k cryogenics
1105 system, which contains all the major cryogenic handling components. Apart from the condenser,
1106 the cold box contains five heat exchanger modules to efficiently pre-cool the argon gas by cold
1107 nitrogen gas and cold outgoing argon gas. In this way the necessary cooling power is reduced
1108 dramatically. The radon trap is placed between the coldest and the second coldest heat exchanger
1109 modules to ensure that the argon passing through is still in its gas phase, while at its lowest
1110 temperature, which maximizes the radon removal efficiency. Eight cryogenic valves and several
1111 temperature and pressure sensors are also installed to control and monitor the system. Tubings
1112 are chosen as 1" OD stainless steel, in order to accommodate the argon circulation speed up to
1113 1000 std L/min.

1114 The stainless steel LAr condenser contains 127 0.5" OD top-sealed tubes finely patterned on a
1115 thick plate as the thermal exchanging part of the condenser. The condenser is therefore separated
1116 into the nitrogen volume on the top and the argon volume on the bottom. A so-called *chicken
1117 feeder* is mounted at the end of the liquid nitrogen delivery tube to maintain a continuous liquid
1118 nitrogen dropping. The flow of the evaporated nitrogen gas is monitored by a mass flow meter
1119 and adjusted by a control valve, both located at ambient temperature. The control valve uses
1120 the LAr TPC pressure from both UAr and AAr as feedback signal to automatically adjust the
1121 evaporated nitrogen gas flow rate, which is essentially the cooling power of the condenser, hence
1122 in return maintains the LAr TPC pressure at the desired set point and balanced with AAr system
1123 with an incredible stability, as demonstrated in DS-50.

1124 Based on the successful demonstration of the gas circulation pump in DS-50, which provides a
1125 speed up to 50 std L/min, the gas circulation pump of DS-20k uses the similar design, relying on two
1126 components: linear motors and reed valves. The linear motors, consisting of a piston and cylinder
1127 pair, can provide a continuously adjustable pumping power. The reed valves guide the gas flow
1128 direction when the linear motors going back and forth. Two balanced linear motors will be placed
1129 face to face, to counteract the vibration produced during the motor operation. The combination of
1130 the linear motors and the reed valve allows the pump to work in a frictionless condition, resulting
1131 in a long lifetime. The initial fast circulation requires a speed of 1000 std L/min to achieve a good
1132 UAr purity level, and then the circulation speed can be decreased to only maintain the purity
1133 and stability. This minimum flow could be very low since the UAr system essentially is embedded
1134 in the AAr system while all cold electronics are outside the UAr volume so no cooling power is
1135 required. To achieve such a high circulation speed, flexibility of operations, as well as the ease of
1136 the pump development, two individual circulation pumps will be placed in parallel, each providing
1137 a circulation rate up to 500 std L/min. A full-size prototype circulation pump has been fabricated
1138 at UCLA and Princeton, and passed the initial tests. It was shipped to CERN and is being certified
1139 for the EU safety requirement. Once fully tested, it will be integrated into the prototype cryogenics

1140 system for the full-system test.

1141 The heat exchangers close to the TPC are basically large heat exchangers using many tubes as
1142 the thermal exchanging parts, similar to the concept of the LAr condenser described above, but
1143 with a much increased thermal exchanging surface area. Outgoing LAr from the LAr TPC absorbs
1144 heat from the incoming liquid-gas mixture of purified argon here, boils off into gas phase, and then
1145 enters the circulation loop. This heat exchanger is located above the LAr TPC and ensures that all
1146 outgoing argon above it will be in gas phase, avoiding otherwise a large argon head height coming
1147 directly from the LAr TPC to the lowest heat exchanger modules in the cold box. This would
1148 result in an argon pressure below its triple point at some point in the argon loop and causing argon
1149 to freeze. Another set of near TPC heat exchangers are strategically placed close to bottom level
1150 of the UAr TPC for fast recovery during the draining stage. This lower level heat exchanger is
1151 completely passive during normal operations and only useful during the draining phase. The entire
1152 near TPC heat exchangers are immersed in LAr inside the ProtoDUNE cryostat, which serves as
1153 a thermal bath for them.

1154 The integration and tests of the full scale UAr cryogenics system at CERN is ongoing. The first
1155 pass FEA engineering has proven the design load is as anticipated and fabrication is officially ap-
1156 proved. All condenser box components, large pneumatic cryogenics valves and associated auxiliary
1157 components are on site at CERN for integration. The full scale cryogenics test of the DarkSide-20k
1158 UAr system will be performed over the summer of 2019.

1159

7. MATERIAL ASSAYS

1160 Trace radioactivity in detector materials can be a dominant background for the direct dark-
1161 matter searches. In addition to this bulk contamination, a major source of background can be
1162 caused by the cosmogenic activation of the materials and by the surface contamination (due to
1163 radon diffusion and plate out of the radon daughters produced in the surrounding air). Beta and
1164 alpha particles produced by the radionuclide decays can typically contribute to the background
1165 only if the atom is in contact with the LAr target, while gammas and neutrons, the last ones from
1166 spontaneous fission and (α, n) interactions, can produce background from more distant sites.

1167 A strategy for selecting the materials, as well as machining, storing, transporting and mounting
1168 the detector components, is mandatory in order to control the backgrounds and to maximize the
1169 physics reach of DS-20k. This will be accomplished by developing the “background budget” to
1170 identify materials’ purity requirements. In addition to the assays on the raw purchased materials,
1171 performed to identify the right technologies and compositions, we are developing cleaning and
1172 handling procedures to meet radiopurity standards, and performing assays to validate processes for
1173 the construction and commissioning of the detector and its components.

1174 In DS-20k this responsibility is delegated to the Materials and Assays Working Group (M&A WG),
1175 a single Working Group within the collaboration, comprised of experts in each of the assay methods
1176 and representatives from each institution that hosts assay capabilities. The group coordinates and
1177 schedules the assays according to the pre-evaluated radiopurity requirements, the urgency, the
1178 capacity of the available assaying resources and their queue.

1179 The goal is to assay and approve *all* materials or items selected to reside within the cryostat,
1180 particularly by scrutinizing the entire ^{232}Th and ^{238}U decay chains. This calls for multiple assays
1181 with multiple techniques for each sample, as different techniques are applicable to different sub-
1182 chains of the ^{232}Th and ^{238}U decay chains. These results are combined with the (α, n) cross-sections,
1183 calculated according to the chemical composition of the material in order to extract the neutron
1184 yield expected in the detector.

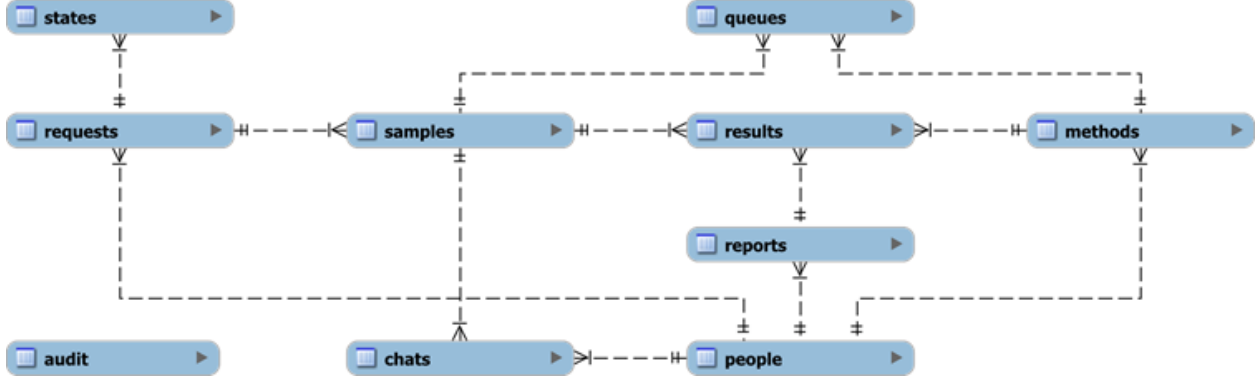


FIG. 19. A simplified DS-20k materials database structure. Information on each relevant aspect of the assay process is stored in the database, facilitating the management of the whole assay process.

1185

7.1. Radio-purity database

1186 The need for fast access to, and exchange of data between different Working Groups (WG) is
 1187 addressed by the DarkSide Materials Database (MDB). Information on the radioactive content of
 1188 materials to be used for DS-20k construction is stored therein, and is crucial for the comprehensive
 1189 estimation of the background budget for the experiment. The MDB contains all the relevant
 1190 information about samples: chemical composition, origin (production batch), data-sheets, pictures,
 1191 part of the detector where it will be placed, history of assays etc. This information is included in
 1192 the total background budget estimation and carefully evaluated. Rules for handling and cleaning of
 1193 samples, developed and verified during the screening process, are also stored in the database. Later,
 1194 during the detector construction and integration, reproducible results of the estimated internal
 1195 background may be expected upon application of the provided handling and cleaning procedures.

1196 The database helps to systematize the radioactive background budget estimation, material se-
 1197 lection and tracking, assay prioritization, and cleaning and handling methods. Additionally, the
 1198 database is also used to balance the workload and assay resources between numerous institutions
 1199 involved in the task by coupling assay needs with assay capabilities of members of the Materials
 1200 WG.

1201 The MDB structure reflects the flow of the material assay process, aiding material selection
 1202 and application during the construction phase of the experiment. The database consists of several
 1203 cross-related tables, holding information on the status of the assay requests, screening methods,
 1204 samples, assay results and people (institutions) involved (see Fig. 19). It also keeps track of the
 1205 queues in different facilities, and the history and the current status of any assay performed within
 1206 the M&A WG. A convenient web-based interface is provided for the users (see Fig. 20), dedicated
 1207 to: ease submission of new assay requests from other Working Groups; browse and report of the
 1208 assay results (including uploading the results); and to manage the assay status of the samples and
 1209 queues at different facilities.

1210 Assay results obtained for the materials used for DS-50 were also imported to the new database.
 1211 Currently the database stores almost 2000 assay results (more than 120 assays performed since
 1212 2017) of nearly 300 samples, and counts (see Tab. V). The M&A WG has established protocols to
 1213 efficiently handle the radioactive budget of the experiment.

1214

7.2. Managing Assay Capabilities

1215 To ensure the radiopurity of all detector materials to the levels defined by the background model,
 1216 the M&A WG has developed a radiopurity assay program that takes advantage of facilities through-
 1217 out the collaboration. Overall, it is anticipated that this program will span approximately three
 1218 years and will involve around a thousand more assays, including searches for radiopure materi-

Sample name	Description	Batch	DS-20 reference	Search ▾												
Show 25 entries					Copy	CSV	Hide empty	Show all	Column visibility ▾	Search: capa						
ID	Report	Name	Reference	Method	Sample	Date	^{60}Co	^{137}Cs	K	^{40}K	^{234m}Pa	Pb	^{210}Pb	^{210}Po	^{226}Ra	
1910	253	Capacitor 22pF	273 Non-satisfactory	PDM module	HPGe GeDSG (Matthias Laubenstein, LNGS, INFN),	complete	2018-12-13	<6 [mBq/kg] (3 sigma)	<6 [mBq/kg] (3 sigma)		1.5 ± 0.7 [Bq/kg] (1 sigma)	<1 [Bq/kg] (3 sigma)				<1 [Bq/kg] (3 sigma)
36	5	Panasonic SMD capacitors	5 Decision pending	PDM module	HPGe GeCris (Matthias Laubenstein, LNGS, INFN),	complete	2017-12-14	<2 [mBq/kg]	<4 [mBq/kg]		<1 [Bq/kg]	<2 [Bq/kg]				<6 [mBq/kg]
1854	246	Panasonic capacitors	57 More assays needed	PDM module	HPGe BEGe (Matthias Laubenstein, LNGS, INFN),	complete	2018-08-30	<7 [mBq/kg]	<5 [mBq/kg]		<2 [Bq/kg]	<7 [Bq/kg]				<0.2 [Bq/kg]

FIG. 20. Interface web page, presenting a selection of assay results for various types of capacitors. The database is also used to manage the assay process of each sample.

als, development and validation of cleaning and handling procedures, and screening of all detector components. The collaboration has extensive and diverse assay capabilities that are sufficient to complete this program on schedule, with extra capacity to handle additional unforeseen assays. Estimates of the capacity available to DS-20k for each assay type are summarized in Tab. VI. The assay challenges are organized into six focus areas: mass spectrometry (ICP-MS), radon emanation, direct gamma assay (HPGe), surface assays (alpha activity), cosmogenic activation and materials handling and process development.

7.3. Radioactive budget

The radioactive budget states the expected background of everything that goes into the detector, taking into account material's (element) radiopurity, mass, composition, shape and location. These parameters are the input of Monte Carlo simulations, performed using a Geant4-based package written within the collaboration and called G4DS. The result of the simulation is the efficiency of our detector for rejecting the background coming from different sources, either because of geometrical reasons or because of active tagging of undesired events. The neutron budget is calculated on a single-element basis, so the mentioned inputs (radiopurity, composition and the position in the detector) are needed for every component of the detector.

The most critical requirement in terms of radiopurity is given by the α activity, mainly caused by the naturally occurring radioactive chains of ^{232}Th and ^{238}U and potentially producing neutrons through (α, n) reactions. The cross section of this reaction is calculated using the *neucbot* program, where the energy spectrum of neutrons is generated as well. Hence, the (chemical) composition and construction of each component needs to be known with sufficient detail in order to calculate the interaction cross-sections correctly.

Provided that some construction elements may be in similar locations, and that a component may be used in different places, a cross-linked, multi-tab spreadsheet is used to calculate the expected neutron budget. Propagation of any modifications or updates in a coherent way is easy to maintain. A summary of background budget components is tabulated in a user-friendly form, collecting all the relevant information structured following the same organization scheme as the Working Groups in the collaboration (Veto, TPC, PhotoElectronics, etc). M&A WG is in close cooperation with other WGs through dedicated group representatives, aiding selection of proper construction materials at the early stages of the design. The background budget is constantly evolving and converging as the material assay campaign progresses, such that more components' activities are determined.

Assay Method	Number of assays
ICP-MS	50
Germanium spectroscopy	40
Chemical extraction of Po	20
Surface α 's counting	5
Radon emanation	5
Other	3

TABLE V. Summary of the assays performed since 2017 in preparations of the DS-20k construction, with breakdown by assay method.

Assay Method	Capacity [assays per year]
ICP-MS	60
Germanium spectroscopy	35
Chemical extraction of Po	20
Surface α 's counting	10
Radon emanation	10

TABLE VI. Summary of the assay capabilities available for DS-20k.

1250 It is estimated that over 1000 more assays will be performed until the completion of the detector
 1251 construction, for more than 150 expected material samples.

1252

8. CALIBRATION

1253 Calibrations for both the TPC and the Veto range from low-level detector issues, such as the
 1254 single-photoelectron response of individual photosensors, to high-level physics issues like the accep-
 1255 tance as a function of energy for nuclear recoils. The combination of radioactive sources, neutron
 1256 generators, and light sources ensures a robust calibration plan to reach ultimate science goals of
 1257 DS-20k.

1258

8.1. Distributed Gas Sources

1259 Full volume calibration of the TPC will be achieved with distributed gas sources: ^{83m}Kr and
 1260 ^{220}Rn . Gas sources are simple to implement, since they are added to the argon recirculation stream
 1261 and feature short halflives, quickly decaying out from the argon target volume. The monoenergetic
 1262 decays of ^{83m}Kr , distributed through the active volume of the TPC, can give a key calibration
 1263 point in the WIMP recoil energy region. The 3D reconstruction of events in the TPC allows a full
 1264 mapping of position-dependence of the light yield using the ^{83m}Kr source. This means that, while
 1265 broad dissemination through the active volume is important, a uniform distribution is not required.

1266 The ^{83m}Kr decays quickly ($\tau = 2.64\text{ h}$) to a stable nuclide and causes no long-term contamina-
 1267 tion or background to the WIMP search. The DS-20k ^{83m}Kr source is based on the source used
 1268 successfully in DS-50. A tiny droplet of a solution of ^{83}Rb ($\tau=124.4\text{ d}$) is adsorbed into a piece
 1269 of charcoal, which, after drying, is placed between two particulate filters in a branch of the argon
 1270 recirculation system which is normally isolated by valves and can separately be pumped to vacuum.
 1271 In DS-50, an initial 8.5 kBq of ^{83}Rb gave a ^{83m}Kr trigger rate of hundreds of Hz, even though the
 1272 flow subsequently passed through a cooled radon trap. In DS-20k, the challenge will be to get the
 1273 ^{83m}Kr broadly distributed in the 49.7 t active mass before it decays. To further this, LAr will be
 1274 returned to the TPC after repurification via numerous tubes whose endpoints will be distributed
 1275 over the surface area of the TPC side panels.

1276 ^{220}Rn and its short-lived daughters produce several γ -rays, β 's, and α 's of various energies,
 1277 making it an attractive distributed calibration source that can be implemented in a similar manner
 1278 as the ^{83m}Kr source, except for the need to bypass the charcoal trap before insertion into the gas

1279 stream. The source of ^{220}Rn may be prepared as an electroplated ^{228}Th on stainless steel or copper.
1280 Enclosed in a small metal-sealed and vacuum-tight volume equipped with a VCR/CF port. The
1281 advantages of the ^{220}Rn source are the following:

- ^{220}Rn and its daughters are short-lived, the longest half-life in the chain is 10.6 h for ^{212}Bi ,
1282 therefore the activity introduce into the detector will disappear after a few days;
- The high energy alphas appearing in the chain (6.05 MeV, 6.09 MeV, 6.29 MeV, 6.78 MeV, and
1284 8.78 MeV);
- The coincident ^{220}Rn - ^{216}Po and ^{212}Bi - ^{212}Po decays will allow to study the homogeneity of the
1286 distributed sources, and possible LAr flow patterns as well as potential “dead volumes” that are
1288 not affected by the LAr circulation;
- Drift of the charged ions inside the LAr volume (interesting also with respect to Po isotopes from
1289 the ^{222}Rn chain);
- Low-energy β 's appearing in the chain may be used for calibrations of the low-energy response
1292 of the detector.

1293 To avoid removal of the ^{220}Rn source by the charcoal trap it should be bypassed during the
1294 calibration run. Release of ^{220}Rn from the source should be done in a way that avoids contamination
1295 of the detector with residual ^{224}Ra (half-life 3.6 d) or ^{228}Th (half-life 1.9 yr). A similar risk exists
1296 for the ^{83m}Kr source, but has been thoroughly mitigated and never observed.

1297 8.2. Gamma Sources

1298 Three external γ -ray sources, ^{60}Co , ^{133}Ba , and ^{137}Cs , are planned for use in the TPC calibration.
1299 The combination of these sources in the absence of ^{39}Ar gives an excellent calibration of the electron
1300 recoil PSD band, energy scale and provide valuable data for tuning of the detector response in the
1301 Monte Carlo simulation. The γ -ray sources were chosen to span the energy range of interest in
1302 combination with the distributed ^{83m}Kr source: 41.5 keV for ^{83m}Kr , 122 keV for ^{60}Co , 356 keV for
1303 ^{133}Ba , and 662 keV for ^{137}Cs . Sources will be miniature in size to be inserted inside the source
1304 guide tube for TPC, the overall design of which is shown in Figure 21.

1305 8.3. Neutron Sources

1306 Neutron sources are of particular interest for calibration of the nuclear recoil PSD band and
1307 the efficiency of the neutron veto, a key feature of the DS-20k design. Small (α, n) sources such as
1308 $^{241}\text{AmBe}$ and ^{241}Am - ^{13}C will be fabricated for this purpose. $^{241}\text{AmBe}$ is utilized as a tagged neutron
1309 source utilizing 4.4 MeV gamma in 56 % cases. ^{241}Am - ^{13}C can serve as a gamma-free source for Veto
1310 neutron calibration, after slowing down alphas for (α, n) reaction to always produce daughters in
1311 the ground state. Sources will be small in size to be delivered with the source guide.

1312 While the ^{241}Am - ^{13}C source represents the best choice for calibration of the neutron detection
1313 efficiency, interactions in the source holder and materials between the source and the TPC pro-
1314 duced significant electron recoil background in the DS-50 TPC, problematic for characterization
1315 of the nuclear recoils of argon nuclei. The $^{241}\text{AmBe}$ source was shown to be more suitable for this
1316 calibration. The 4.4 MeV γ -ray is promptly emitted in the $^9\text{Be}(\alpha, n)^{12}\text{C}$ nuclear reaction in about
1317 56 % of cases. By tagging the 4.4 MeV γ -ray in the Veto in a very tightly constrained time interval
1318 prior to the signal in the TPC, a very pure sample of nuclear recoils is obtained. The $^{241}\text{AmBe}$
1319 calibration in DS-50 provided the best available nuclear recoil calibration of the DS-50 TPC *in situ*,
1320 and was in excellent agreement with the nuclear recoil calibration from the stand-alone SCENE
1321 experiment [33].

1322 The main novelty planned for the $^{241}\text{AmBe}$ calibration is a custom production of a miniature (a
1323 few mm) $^{241}\text{AmBe}$ source, since the typically available commercial sources cannot fit within the
1324 planned narrow guide tube system. The miniature $^{241}\text{AmBe}$ source will rely on the procedure de-
1325 veloped by the neutrino group at the University of Alabama [58]. The group successfully fabricated

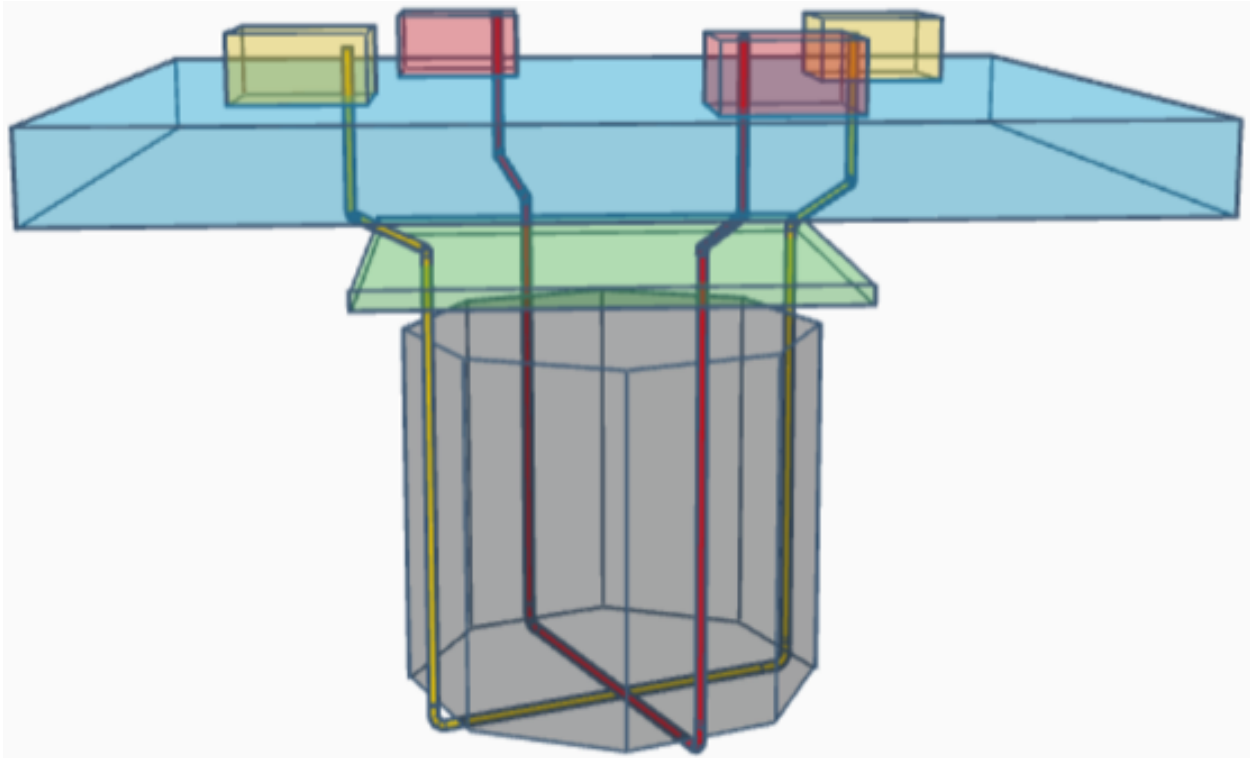


FIG. 21. Schematic representation of the system of guide tubes for insertion of sources.

1326 an $^{241}\text{AmBe}$ source with an outer capsule dimension of just 2 mm in diameter and 7 mm long, with
 1327 an activity of 50 neutrons per second using 1.9 MBq of ^{241}Am . Fig. 22 shows the outer and inner
 1328 source capsules. The inner capsule is made of tungsten to efficiently suppress the 4 MeV gamma
 1329 emission from the ^{241}Am . A very pure Be powder is mixed with ^{241}Am high purity powder in an
 1330 alcohol solution in a miniature test tube with a special micropipette and then transferred into the
 1331 tungsten capsule. After the alcohol evaporates, the procedure is repeated. In the end, the mixture
 1332 of $^{241}\text{AmBe}$ is compressed with a wire for higher source activity. The wire is also used to seal
 1333 the tungsten capsule. The tungsten capsule is placed inside the stainless steel capsule and welded
 1334 shut. The source is then ready for certification and use. The outside capsule has a threaded part
 1335 to attach the source to the rest of the calibration system.

1336 Photoneutron sources such as YBe emit nearly monoenergetic 157 keV neutrons, suitable for the
 1337 low energy end of the nuclear recoil band. However, such source requires 15 cm thick tungsten
 1338 shield to block copious γ -rays present in the source. Thus, this source is very bulky and requires
 1339 a separate deployment system. Deployments will be monitored via a camera system to avoid any
 1340 undesirable contact while operating in a delicate Veto.

1341

8.4. Guide Tube System

1342 Implementation of calibration sources is being finalized, following the completion of the designs of
 1343 the TPC the Veto, and the AAr cryostat. In parallel, plans are being developed for the calibration
 1344 needs of the DS-20k prototype detectors for x-y positioning, light yield and nuclear recoil calibration.
 1345 While work is still in progress, the overall schematic of how to guide radioactive sources from the
 1346 roof of the AAr cryostat, down around and inside of the Veto detector, and then back up to the
 1347 cryostat roof, is shown in Figure 21. The guide tube systems have been designed for simple, safe
 1348 and efficient calibration of the Veto and TPC using miniature radioactive sources. They will allow
 1349 deployment of the sources inside the Veto without direct contact with the argon, eliminating risks
 1350 associated with it.

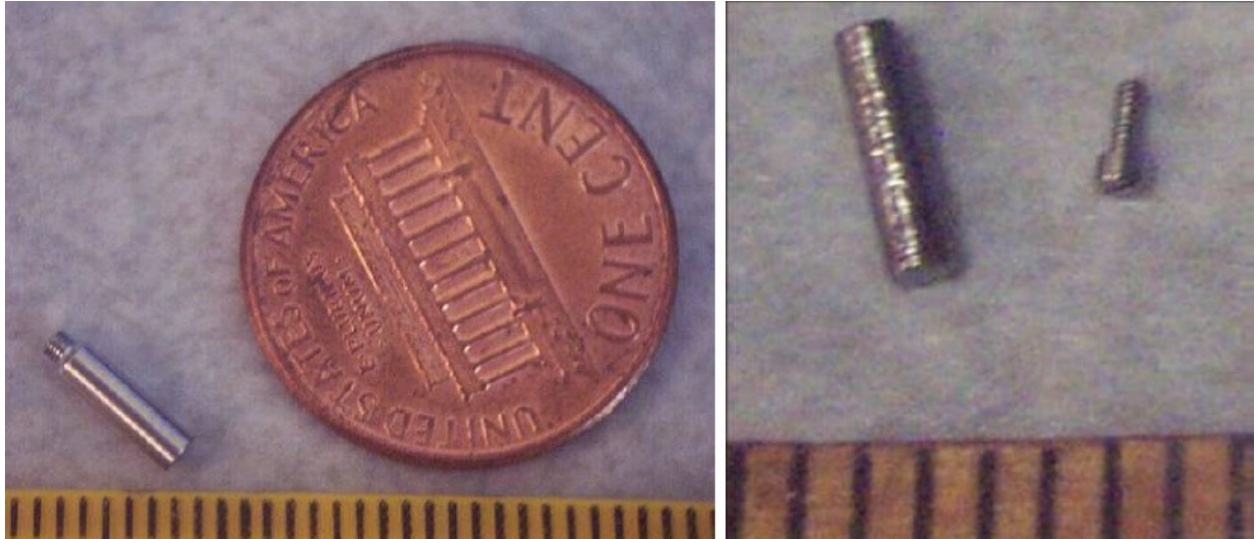


FIG. 22. **Left:** the outer capsule of the custom made $^{241}\text{AmBe}$ source from the Alabama group [58]. **Right:** the inner tungsten capsule of said $^{241}\text{AmBe}$ source.

1351 The guide tube system will bring radioactive sources from the top of the AAr cryostat, to
 1352 locations along the TPC exterior. The sources will be delivered through an enclosed stainless steel
 1353 tube coming vertically down from the top of the cryostat, passing by the TPC PMMA vessel and
 1354 around its bottom. The guide tubes will be 3 cm (1.18") in diameter to minimize shadowing, dead
 1355 space and radioactive background coming from the stainless steel. The stainless steel tube segments
 1356 will be connected with Swagelok connectors. In addition, relatively small tube diameter will help
 1357 for tighter control of the source location, especially important in the case of the gamma sources.

1358 The miniature sources will be attached to the stainless steel guide wire that will be pushed with
 1359 a wire driver powered by a stepper motor. A sleeve, made out of the PTFE tubing, will envelope
 1360 the guide wire and the source to significantly reduce friction while the source and its guide wire are
 1361 being pushed around. The wire driver will be equipped with a set of encoders and two sensor boxes
 1362 for accurate positioning of the source. A pair of ring type inductive proximity sensors placed inside
 1363 the sensor box will be used to reset the encoders when sources pass through a sensor at exactly
 1364 known locations. The system will be purged with a low pressure nitrogen to eliminate any residual
 1365 radioactivity that may have entered into the tubes.

1366 Except for the sensor box, all other parts of the guide tube system that require power, control
 1367 and nitrogen flow will be at the top of the AAr cryostat. An elaborate testing program must be
 1368 performed to ensure high quality and safety of the calibration when using the guide tube system.
 1369 All parts will be radio-assayed and the entire system will be tested off-site for robustness, precision
 1370 and reliability. Dedicated survey is planned to record the exact guide tube path around the TPC
 1371 PMMA vessel.

1372

9. VETO DETECTOR

1373

9.1. Overall Design

1374 Benefiting from the implementation of a ProtoDUNE-like AAr cryostat, the Veto detector will
 1375 utilize AAr as the scintillation material. The Veto detector is composed of three separate volumes;
 1376 a passive octagonal acrylic shell loaded with gadolinium called the GdA and mounted around the
 1377 TPC and providing $4 - \pi$ coverage, a 40 cm thick inner volume of active liquid AAr called the Inner
 1378 Argon Buffer (IAB) and sandwiched between the TPC vessel and the GdA, a 40 cm thick outer
 1379 active volume of AAr called the Outer Argon Buffer (OAB) contained between the GdA and the

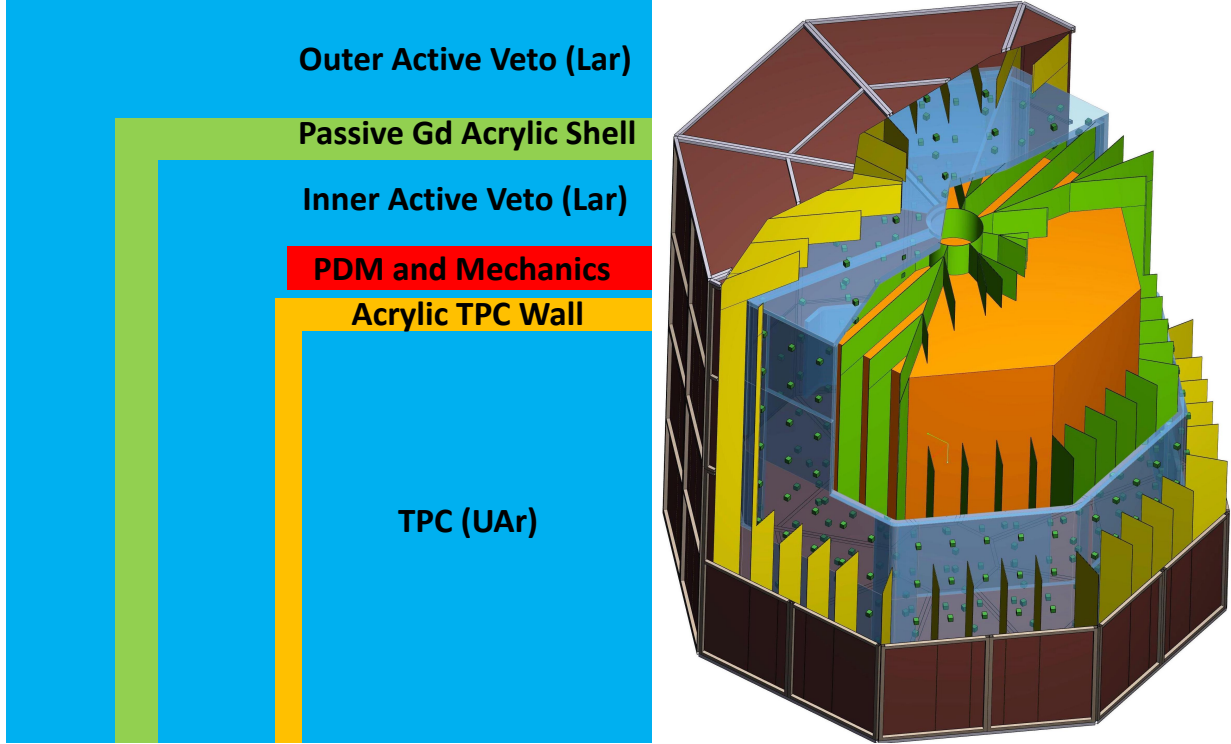


FIG. 23. **Left:** schematic conceptual view of the veto detector. **Right:** 3D cut-away view of the DS-20k veto detector.

1380 outer copper Faraday Cage. The Faraday Cage will contain the Veto and TPC and optically and
 1381 electrically isolate them from the remaining outermost AAr volume contained within the cryostat.
 1382 A schematic drawing of the Veto concept is shown in the left side of Figure 23, as well as a 3D
 1383 cut-away drawing which presents the preliminary design.

1384 The required thickness of both the IAB and OAB of about 40 cm has been determined by MC
 1385 simulation. The required thickness of the GdAS determined by the same simulation, is about 10 cm
 1386 with a required Gd loading of 1 to 2 % by weight. The GdAS moderates neutrons emitted from all
 1387 of the detector materials, particularly from the ones which make-up and surround the LAr TPC,
 1388 while also enhancing the neutron capture probability with the inclusion of the Gd. The capture of
 1389 the neutron on a Gd nucleus results in the emission of multiple γ -rays. These γ -rays interact in
 1390 the IAB and OAB, their detection efficiency setting the required GdAS thickness and Gd loading
 1391 fraction, as well as the minimum required IAB and OAB thickness. γ -rays are detected by use of
 1392 scintillation light emitted by the liquefied AAr in both the IAB and OAB.

1393 Vertical segmentation of the IAB and OAB is foreseen to reduce the pile-up rate of ^{39}Ar events
 1394 from the AAr. The concept of this is shown in the cut-away view of the detector in the right panel
 1395 of Figure 23, while the exact details are still being optimized by use of the Monte Carlo simulation.
 1396 SiPMs will be mounted on the sides of the GdAS such that they are facing both the IAB and OAB.
 1397 The basic detector element is the same PDM used in the TPC, but with a different front-end board
 1398 coupled to it that is optimized for the geometry of the Veto detector. Tests are in progress to
 1399 investigate the possibility of using an integrated electronics readout design for the Veto detector.

1400 All of the inner surfaces of the Veto, including the external walls of the TPC and the walls of the
 1401 vertical sectors, will be covered with reflector foils coated with wavelength shifter (TPB), so that
 1402 the VUV argon scintillation light is shifted to longer wavelengths where the LAr is very transparent.
 1403 This light is then trapped within a segment of the Veto detector by multiple reflections until it
 1404 reaches a SiPM. The optimal number of segments is being studied with the Monte Carlo simulation.
 1405 We expect no more than 5 segments for each edge of the octagon. The segments are not liquid tight
 1406 to allow flow of the argon through them, with a dedicated fluid-dynamics simulation planned to be

1407 performed to ensure that the LAr can be properly re-circulated throughout the proposed geometry.

1408 The overall Veto detector design and the Monte Carlo simulation results will be validated using
1409 smaller prototype setups. Due to the nested nature of the detector system, strategic planning for
1410 the detector integration is also a big part of the development planning.

1411 This conceptual design promises to achieve the most important criteria for the DS-20k detector,
1412 which is the efficient detection of neutrons such that no instrumental background interferes with
1413 the potential nuclear recoil signal from a WIMP scattering off of an argon nucleus. The design
1414 concept is scalable and lends well to serve as the basis for the future 400 t scale detector designed
1415 to collect an exposure of 1000 t yr in absence of instrumental background. The Veto design is based
1416 on elements which require no R&D and therefore can be built out of materials already available,
1417 with the only exception being the gadolinium loaded acrylic. We have established good contacts
1418 and an agreement with a company available to test in its laboratory techniques to mix gadolinium
1419 compounds with liquid MMA before starting the polymerization process. Taking into account that
1420 we do not need the final Gd-doped acrylic to be transparent to light (it acts only as passive neutron
1421 moderator), and that the homogeneity of the mixture is also not a critical parameter, several known
1422 difficulties related to metal loading into plastic scintillators are not an issue. After the success of
1423 the small scale laboratory test done in 2018, the company who will likely provide the high-quality
1424 acrylic for the JUNO experiment has agreed to produce samples of gadolinium loaded acrylic using
1425 their industrial production line. Radio-purity tests will be performed on these samples once they
1426 are available.

1427

9.2. Assembly

1428 The assembly sequence starts with the mounting of the bottom part of the GdAS along with its
1429 PDMs. This component will rest on a stainless steel support structure (Veto support structure)
1430 that is itself supported by the cryostat floor via temporary feet. The TPC is then lowered into its
1431 place above the bottom of the Veto detector. Once in place, the TPC is mechanically connected
1432 to the support structure of the Veto through mounting pillars. This choice has been driven by the
1433 aim of reducing the mass of the support structure of the TPC and avoiding relative movements
1434 between the TPC and the VETO during construction, commissioning and detector operation.

1435 Once the TPC is fixed to the Veto support structure, the lateral panels of the GdAS and their
1436 PDMs are mounted. The vertical thin panels that divide the IAB into segments are then installed.
1437 The top GdAS panels are assembled next. Once the construction of the IAB is completed, PDMs are
1438 installed on the external surfaces of the GdAS and the panels which divide the OAB into segments
1439 are integrated. Then the copper frames that are used as the main structure of the Faraday cage
1440 are installed in the outermost part of the Veto. Finally the Veto detector is hanged from the
1441 cryostat roof using a dedicated support structure and several Kevlar ropes. One the Veto detector
1442 construction is completed, the temporary pillars used to support the Veto on the cryostat floor
1443 during the construction are removed.

1444

9.3. Background Rejection

1445 The combination of the signals occurring inside the IAB and OAB, within a given time window,
1446 is used to tag and reject neutron captures. If a neutron produces a signal in the TPC, it will mimic
1447 that of a WIMP signal, meaning that it produces a single energy deposit with energy in the range
1448 30 keV_{nr} to 200 keV_{nr}. This also includes fiducial volume cuts which exclude events occurring at a
1449 distance from the TPC walls less than 30 cm in the radial direction and less than 70 cm from the
1450 top and bottom. For events that pass this fiducialization, the Veto is then searched within a time
1451 window of 800 μ s around the TPC trigger time. To minimize dead time losses due to β -decay from
1452 ^{39}Ar in the veto filled with AAr, a 800 keV threshold is set for each of the two parts of the Veto

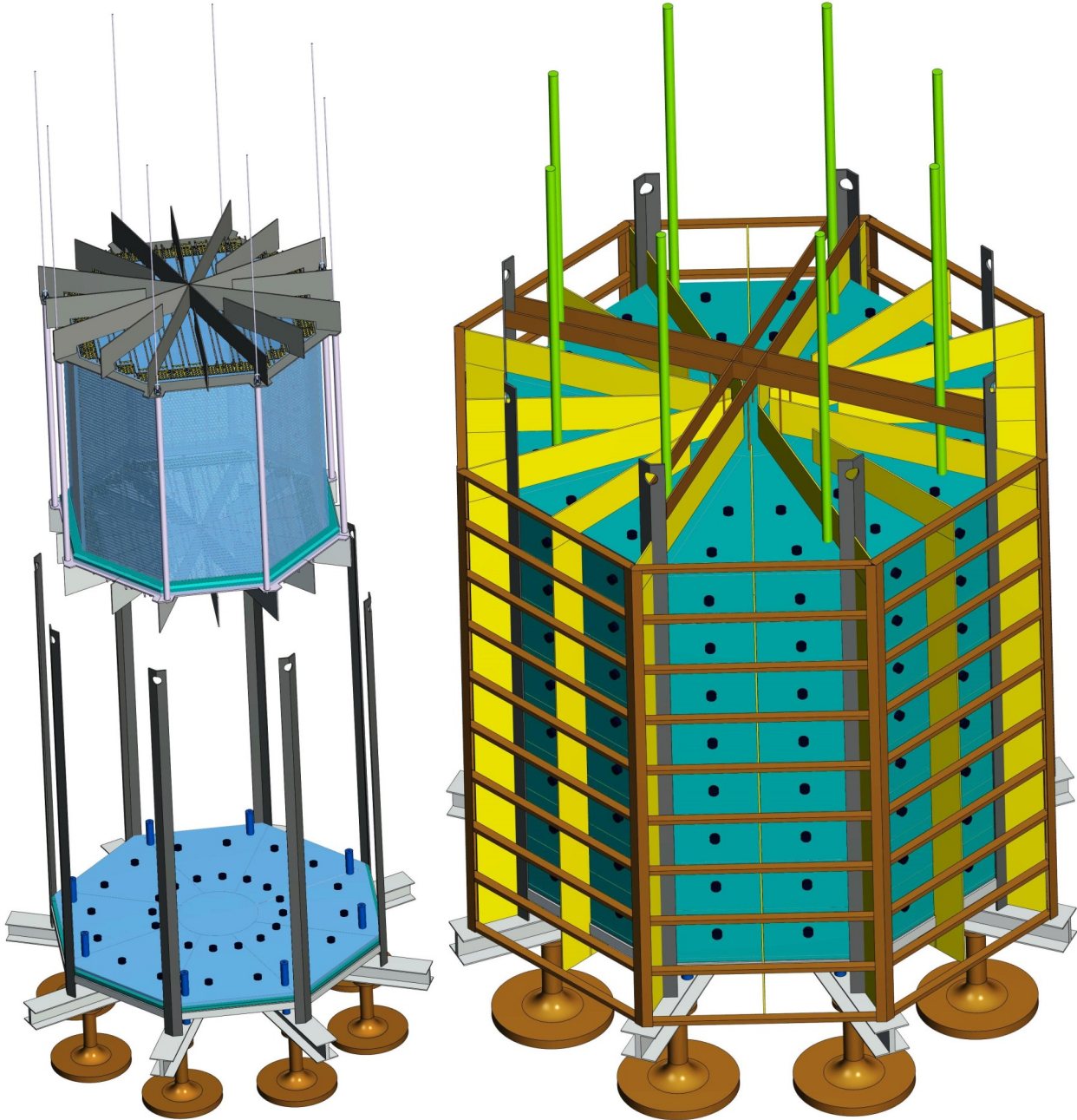


FIG. 24. **Right** Conceptual view of the placement of the TPC within the Veto support structure. **Left** 3D drawing of the DS-20k Veto detector, along with the temporary bottom support structure used for assembly and the Faraday cage.

1453 detector, while a lower 100 keV threshold is set for events with coincidence signals in both parts of
 1454 the Veto detector.

1455 The design of the Veto and the choice of all the materials used to build the entire detector are
 1456 set by the requirement of having less than <0.1 events untagged neutrons during the total exposure
 1457 of 200 t yr. The radioactive contamination of the materials used to build the Veto is therefore also
 1458 considered and limits are set by requiring that the corresponding neutron background induced in
 1459 the TPC, after the implementation of all analysis cuts, is well below the above mentioned threshold
 1460 of <0.1 events in 200 t yr.

1461 DS-20k is designed to operate with zero backgrounds, meaning that all sources of instrumental

Material	Mass [tonne]	^{238}U [mBq/kg]	^{226}Ra [mBq/kg]	^{232}Th [mBq/kg]	Neutrons $[10\text{ yr}]^{-1}$	+TPC $[200\text{ t yr}]^{-1}$	+TPC+veto $[200\text{ t yr}]^{-1}$
TPC Vessel	2.7	1.2×10^{-2}	10	4.1×10^{-3}	1.1×10^3	0.17	1.7×10^{-2}
TPC SiPMs	0.12	-	-	-	1.1×10^4	0.16	1.6×10^{-2}
TPC Electronics	1.0	-	-	-	2.5×10^4	0.36	3.6×10^{-2}
TPC Mechanics	1.1	3.9	3.9	1.9	1.8×10^3	1.8×10^{-2}	2.0×10^{-3}
Veto SiPMs+elec.	0.40	-	-	-	1.3×10^4	0.10	1.0×10^{-2}
Veto Acrylic	13	1.2×10^{-2}	10	4.1×10^{-3}	5.2×10^3	4.2×10^{-2}	4.0×10^{-3}
Veto Reflectors	1.0	1.2×10^{-2}	1.0	4.1×10^{-3}	4.0×10^2	2.4×10^{-2}	2.0×10^{-3}
Veto Steel	1.1	3.9	3.9	1.9	1.8×10^3	1.4×10^{-2}	1.0×10^{-3}
$\text{Gd}_2(\text{SO}_4)_3$ α 's on self	0.26	7.0	7.0	0.2	2.1×10^2	2.0×10^{-3}	$<1.0 \times 10^{-3}$
$\text{Gd}_2(\text{SO}_4)_3$ α 's on PMMA	0.26	7.0	7.0	0.2	7.2×10^2	6.0×10^{-3}	1.0×10^{-3}
Copper Cage	1.0	0.30	0.30	2.0×10^{-2}	1.2×10^1	$<1.0 \times 10^{-3}$	$<1.0 \times 10^{-3}$
Cryostat Steel	250	50	1.0×10^3	3.9	1.0×10^6	-	$<1.0 \times 10^{-3}$
Cryostat Insulation	40	3×10^3	8.0×10^3	3.0×10^3	8.0×10^7	-	$<1.0 \times 10^{-3}$
Total						0.9	0.09

TABLE VII. Radiogenic neutrons sourced by the LAr TPC construction materials, veto and cryostat materials, with details of expected contamination levels, background after TPC cuts, and residual background after combined TPC and veto cuts, all relative to the full 10 yr run time and the full fiducial 200 t yr exposure. The number of expected neutrons is calculated from the expected contamination levels and material composition. Note that no specific activity is reported for the TPC SiPMs and associated electronics: in this case the predicted neutron yield is the results of an extremely detailed calculation, accounting for the cumulative contribution of several tens of components, individually assayed. The same consideration holds for the veto SiPMs and electronics, which contribution is reported in combination. For neutrons due to (α, n) reactions resulting from α 's originating from impurities in $\text{Gd}_2(\text{SO}_4)_3$, the contribution is broken down between those due to reactions on Gd sulfate itself and those due to reactions in the PMMA matrix containing the Gd sulfate; the mass fraction of Gd in the GdAS 1%, for the anticipated 2% concentration by mass of $\text{Gd}_2(\text{SO}_4)_3$. (For ease of conversion: 1 ppt(^{238}U) $\simeq 1.2 \times 10^{-2}$ mBq/kg; 1 ppt(^{232}Th) $\simeq 4.1 \times 10^{-3}$ mBq/kg.)

background are reduced to <0.1 events over a 200 t yr exposure. All background from minimum-ionizing radiation sources will be completely removed thanks to the combined action of PSD of the primary scintillation pulse and comparison of the primary and secondary scintillation (see the “Project Narrative” for details on the suppression of background from pp scatters on electrons and Ref. [24] for that from ^{222}Rn , ^{220}Rn , and progenies).

We focus here on the leading source of background, that is neutrons from the LAr TPC construction materials. We simulated the response of the LAr TPC, IAB, and OAB to (α, n) , which is expected to be the dominant contribution to the instrumental background budget. The geometry of the LAr TPC is that described in the rest of the document. The LAr TPC vessel is made of 5 cm-thick PMMA, which helps to mitigate backgrounds by moderating the neutrons coming from the detector’s construction materials. For the PMMA, we assume the purity achieved in Ref. [42], while for the Gd-loaded acrylic, we assume the purity of the scintillator of Ref. [59].

The results of the Monte Carlo simulation are summarized in Table VII, where it is seen that the final results meet the goal of <0.1 events in the full 200 t yr exposure. The two main sources of contamination are the electronics of the SiPMs and the insulation of the cryostat. The collaboration is now working to further improve the materials selection, which could reduce the expected neutron flux coming from those components.

The only remaining background for WIMP searches will be the signal from the coherent scattering of atmospheric neutrinos on argon nuclei, with an expected 3.2 events over the 200 t yr exposure. DS-20k will thus be the first experiment in a position to detect this important signal.

Surface contamination due to plate-out of radon on the surfaces is an additional source of background that can not be neglected. Radon is present in the outdoor air with a concentration of few to 10 Bq/m³, while inside buildings and in underground laboratories the concentration is typically higher (up to 120-150 Bq/m³). ^{210}Pb atoms accumulate on every surface of materials exposed to air and decay to ^{210}Bi that produces ^{210}Po . This is the potentially dangerous isotope because the α originating in its decay could produce neutrons. We estimate the concentration of ^{210}Pb

1488 adsorbed on an acrylic surface using data measured for polyethylene exposed to the SNOLAB air.
1489 We roughly expect a few tens of neutrons (before the analysis cuts) per day during the time which
1490 the entire surface of the acrylic is exposed to atmospheric air. This sets specific requirements for
1491 the cleanliness of the acrylic surfaces and on the mounting procedures of the Veto, which must be
1492 done in a radon free environment.

1493

10. DATA ACQUISITION

1494 The current design for the DS-20k electronics and its data acquisition system (DAQ) accommodates
1495 both the large number of sensors and the long drift-time (expected maximum electron drift
1496 time is 4 ms) of the LAr TPC, as well as the readout of the Veto detector. The trigger rate during
1497 normal dark matter search data taking has three major contributions: background events from de-
1498 tector materials, background events from ^{39}Ar , and random triggers. In order to estimate the first
1499 term, the event rate measured in the UAr exposures of DS-50 is taken, excluding the contribution
1500 from the PMTs and from the remaining ^{39}Ar in DS-50. This is scaled by the ratio of surface areas
1501 of DS-20k and DS-50, a factor of 55, obtaining an expected rate of 27 Hz. It is noted that these
1502 events will be concentrated at the surfaces of the active volume.

1503 By using UAr and making the assumption of an ^{39}Ar reduction factor of 1400 with respect to
1504 AAr, there will still be an additional rate of about 16 Hz generated by ^{39}Ar decays, uniformly
1505 distributed throughout the active volume. In summary, events with correlated S1 and S2 signals
1506 are expected in DS-20k at a rate of about 50 Hz. On the other hand, the average singles rate per
1507 channel is dominated by the dark count rate (DCR) of the SiPMs. With the required 0.08 Hz/mm²
1508 specification, this will imply a singles rate per PDM of about 200 Hz. The event rate in the Veto
1509 detector, instead, will be dominated by ^{39}Ar decays in the instrumented AAr buffers.

1510

10.1. General DAQ scheme

1511 The baseline scheme for the TPC and Veto detector DAQ electronics hardware foresees an optical
1512 signal receiver feeding a differential signal to a flash ADC digitizer board that is connected to a large
1513 Field Programmable Gate Array (FPGA). The digital filtering capability within the digitizer board
1514 would allow the discrimination of single photoelectron signals and the determination of the time
1515 and charge of the individual channel pulses. For large and slow signals, such as the S2 ionization-
1516 born pulses in the TPC, the digitizer board would provide a downsampled waveform matching the
1517 expected signal bandwidth of a few MHz.

1518 The combination of the data processing will provide the needed data reduction to allow trigger-
1519 less operation of the readout for the TPC. Data from the Veto and TPC detectors will be transferred
1520 to the front-end data processing units where further data reduction will be performed. Finally the
1521 data will be passed to an online event building processor that will select interesting events and
1522 write them to permanent storage.

1523 In normal data taking mode, an event could be identified by a coincidence of hits in the TPC
1524 within a specified time window. A coincidence of 7 hits in 200 ns would result in a random trigger
1525 rate well below 0.1 Hz. Nuclear recoil events at the trigger threshold, producing about 15 PE in
1526 5 μs , would result in the collection of 6 PE to 8 PE within the first 200 ns. Thus, the trigger would
1527 be 100 % efficient for the WIMP-like signals of interest.

1528 The event building and software trigger stage is realized with modern commodity CPUs and
1529 connected through fast ethernet with the front-end DAQ processors. Given the low expected rate,
1530 the trigger-less option is foreseen to be feasible to implement. The expected combined event size
1531 for the TPC and Veto detectors is projected to be well below 1 MB.

1532 Synchronization between the TPC and Veto DAQ is fundamental for the effectiveness of the
1533 design, and will be provided and maintained during the data taking. The clock source of the TPC
1534 DAQ will be used as reference and digital signals (like GPS time stamps or trigger IDs) will be

1535 generated to uniquely identify each event regardless of the trigger origin or the detector. A pulsed
1536 signal distributed to all the modules will be used to check and correct the alignment of each channel
1537 among the TPC and Veto detectors.

1538 The DAQ system will be located in an electronics room which will be placed on the roof of the
1539 AAr cryostat. The environment will allow personnel access while minimizing the length of the
1540 optical fibers used to transmit the data from the TPC to the signal receivers.

1541

10.2. Digitizers

1542 The basic readout element of the proposed DS-20k DAQ system is a multi-channel board hosting
1543 several fast ADCs linked to a large FPGA for digital signal processing. This will be connected
1544 to a host CPU for control, monitoring and data formatting using as an output channel through
1545 a 1 Gbit/s to 10 Gbit/s ethernet connection to an external computer. The ADC will have 14 bits
1546 resolution and 125 MHz sampling speed. The board will accommodate one octal fADC chip for
1547 each of the 8 mezzanine boards, allowing it to handle 64 channels in total with a single board with
1548 a VME64 6U form factor. Data from the ADCs will be sent using high bandwidth JESD interface
1549 directly to a large FPGA. The board will host a Xilinx made Zync Ultrascale+ with a quad-core
1550 ARM Cortex A53 processor. Recent progress on this development includes the full implementation
1551 of the JESD interface and the ability to output data at the maximum specified speed. Specialized
1552 firmware is to be provided by the collaboration for noise filtering, basic data formatting and zero
1553 suppression to be implemented in the FPGA.

1554 The development of this electronics board is an ongoing partnership between the CAEN Company
1555 from Viareggio, Italy, which was selected as the provider of the electronics by the INFN, and the
1556 collaboration. The basic layout of the boards and the components that will comprise them have
1557 been selected and the first prototype will be available for testing in the summer of 2019. In the
1558 meantime, work in close cooperation between the GADMC and the CAEN firmware experts is
1559 ongoing to implement the needed signal filtering algorithms. In parallel, a DAQ system for the
1560 initial prototype TPC tests has been deployed at CERN in order to acquire data from up to two
1561 PDM Motherboards, amounting to 50 PDM channels.

1562

10.3. DAQ software

1563 The Maximum Integrated Data Acquisition System (MIDAS) has been chosen as a framework
1564 for developing the DAQ readout and related online control software for the DS-20k detector. The
1565 MIDAS DAQ package has been used extensively within the DEAP-3600 experiment, and together
1566 with the CAEN hardware provides a nice baseline for the digitization and recording of the raw data.
1567 A collaboration between the MIDAS and CAEN developers has been established to ensure that the
1568 interfacing of the front-end hardware is compatible with the back-end hardware and software that
1569 will ultimately compile and write the data to permanent storage.

1570 MIDAS is also well suited for handling the DAQ of the DS-Proto, for which, at least in the first
1571 stage, has a readout strategy and hardware implementation similar to those used in the DEAP-3600
1572 experiment. The DEAP-3600 hardware is mainly composed of 32xVME-V1720 and 4xVME-V1740
1573 using the proprietary CAEN CONET2 optical link to 5 different computers, providing optimum
1574 individual link data throughput using the A3818C PCIe interface. The DS-Proto readout will be,
1575 in the first phase, based on 5 CAEN VME-V1725 and a custom trigger module developed by the
1576 TRIUMF group. This system has been already installed at CERN in the first part of 2019 in order
1577 to provide the DAQ system for the first 50 channels (2 motherboards) of DS-Proto. In a later
1578 stage, the readout for DS-Proto will be based on the new digitizer boards from CAEN, previously
1579 described. Work has started toward designing an evolution of the MIDAS software to accommodate
1580 the new hardware boards and provide the needed event building and software trigger capability.

1581

11. COMPUTING

1582 The data storage and offline processing system must support transfer, storage, and analysis of
 1583 the data recorded by the DAQ system, for the entire lifespan of the experiment. It must provide for
 1584 production and distribution of simulated data, access to conditions and calibration information and
 1585 other non-event data, and provide resources for the physics analysis activities of the collaboration.
 1586 Necessary components for data storage and offline systems are the software framework and services,
 1587 as well as the data management system, user-support services, and the world-wide data access and
 1588 analysis job-submission system. The design of the system is built upon the knowledge acquired in
 1589 the construction and operations of the DS-50 detector.

1590 The large number of channels in the LAr TPC makes it impractical to digitize and save the full
 1591 waveform of each channel, as done in DS-50. Nevertheless, the charge and hit time information
 1592 that will be saved will preserve all the necessary details about the amplitude and time evolution
 1593 of the signals generated in the target. With appropriate filtering and compression, in addition
 1594 to the expected background reduction described elsewhere in this document, the amount of data
 1595 selected for recording in DS-20k is expected to be only a few times that of DS-50. The DS-50
 1596 experiment typically collects about 9×10^5 events/d, of which 8×10^5 events/d come from laser
 1597 calibrations, with the remaining 1×10^5 events/d from the dark matter search. The size of a DS-50
 1598 laser calibration event is about 0.1 MB, while the size of a dark matter search data event is about
 1599 2.6 MB. This is expected to decrease by a factor of 3 to 4 in DS-20k, despite the much larger number
 1600 of channels. Taking into account the event size and data rate, the improved background rejection
 1601 and data filtering, and using the experience from DS-50, the short-term storage required at the
 1602 experimental site is expected to be 20 TB. The total storage inventory required for the experiment
 1603 is expected to be more than 20 PB, including the storage needed for simulated and reconstructed
 1604 events.

1605

11.1. Computing systems and data workflow

1606 The primary event processing will occur at the experimental site in the software trigger farm.
 1607 Pre-processed data is archived on the temporary storage at the experimental site and copied to
 1608 central computing centers (Tier-1/Tier-2). These facilities archive the pre-processed data, provide
 1609 the reprocessing capacity, provide access to the various processed versions, and allow analysis of
 1610 the processed data. Derived datasets produced in the physics analyses are also copied to the
 1611 Tier-1/Tier-2 facilities for further analysis and long-term storage. The Tier-1/Tier-2 facilities also
 1612 provide the simulation capacity for the DS-20k experiment.

1613 Bulk data processing is expected to be performed using low cost commodity cluster computing
 1614 based on commercial CPUs. Final data analysis will be performed either directly at the Tier-1/Tier-
 1615 2 centers or on commercial CPUs hosted at institutes participating in the experiment. There is
 1616 also the option of using the considerable free resources available on the Open Source Grid, which
 1617 many experiments are currently using to run their reconstruction and analysis jobs.

1618 The amount of short term storage currently available at LNGS for DS-50 consist of 7 TB of
 1619 front-end storage used as temporary buffer and located in the underground laboratory, plus 710 TB
 1620 of disk space in the above ground computing center for short- and long-term storage of DS-50 data.
 1621 From there, raw data are copied to CNAF and Fermilab for reprocessing and analysis. CNAF is
 1622 making available 1 PB of disk storage and 300 TB of tape storage. At Fermilab, there is 50 TB
 1623 of fault-tolerant disk storage and about 620 TB on the dCache-based tape system for long-term
 1624 storage. It is expected that much of this inventory will be recycled for the DS-20k experiment,
 1625 aside from what is necessary for ongoing storage of DS-50 raw data. Any necessary additional
 1626 tape storage will be purchased and installed. The total amount of storage for the ten years of
 1627 data-taking, including calibration and simulated data, is 20 PB of disk storage and 20 PB of tape
 1628 storage. The processing power currently used for reprocessing and analysis of DarkSide-50 data
 1629 includes a farm of 400 cores at LNGS for production and validation, plus 400 job queues at CNAF

1630 and 25 guaranteed batch slots (soon to increase to 60 guaranteed batch slots) on the Fermilab grid
1631 system.

1632 Currently, a single DS-50 event takes about a half of a second to reconstruct on a typical 2.8 GHz
1633 processor, meaning that 100 dedicated cores can maintain reconstruction in realtime for an event
1634 rate up to 200 Hz. Assuming a factor two increase in the cpu time needed to reconstruct an event,
1635 a factor ten to simulate a full event, a real data plus calibration event rate of 100 Hz, and a sample
1636 of simulated events of the same dimension of the real-data one, DS-20k needs 100 dedicated cores
1637 to maintain reconstruction in realtime of the collected real data + calibration events, and 1000
1638 dedicated cores to produce the simulated samples. Moreover, 2000 physical cores are sufficient to
1639 reprocess all physics events collected in one year in a three month time period.

1640

11.2. Software Environment

1641 DS-20k will adopt an object-oriented approach to software, based primarily on the C++ pro-
1642 gramming language, with some components implemented using other high level languages (Python
1643 etc.). A software framework has been built up during the DS-50 experiment which provides flexi-
1644 bility in meeting the basic processing needs of the experiment, as well as in responding to changing
1645 requirements. In order to support code reuse, build a system optimized for both the offline and
1646 software trigger environment, and provide common user access to low-level algorithms used for I/O
1647 and data persistency, the C++ code will make heavy use of object oriented abstract interfaces
1648 techniques.

1649 The reconstruction combines information from the TPC and the veto detectors. A typical recon-
1650 struction algorithm takes one or more collections of information from the event data model (EDM)
1651 raw data stream as input, calls a set of modular tools, and outputs one or more collections of recon-
1652 structed objects. Common tools are shared between reconstruction algorithms, exploiting abstract
1653 interfaces to reduce dependencies. Analysis of calibration data will also be performed within the
1654 reconstruction and simulation software environment.

1655 DS-20k will produce roughly 2 PB of data annually, combining the data processing, simulation,
1656 calibration, and distributed analysis activities. A data storage and management infrastructure is
1657 necessary to allow efficient storage and access to all this data. Two types of data storage are
1658 foreseen. The first is a file-based data and the second is relational-database-resident data. File
1659 storage is used for bulky items such as event data (physics data, calibration data and simulation
1660 data). Database storage is used for other types of information, including technical data like detector
1661 production, installation, survey and geometry data, online/TDAQ databases, conditions databases
1662 (online and offline), offline processing configuration and bookkeeping information, and to support
1663 distributed data and database management services. File-based storage of C++ objects will be
1664 implemented through the use of ROOT I/O, which provides high performance and highly scalable
1665 object serialization to random-access files. Database storage will be based on SQL-based relational
1666 databases (MySQL and SQLite). All these technologies are widely used and well tested in HEP
1667 experiments.

1668 Computing resources will be accessed through Grid middleware components and services. These
1669 provide services for software installation and publication, production operations, and data access
1670 for analysis through a uniform security and authorization infrastructure, as well as interfaces for
1671 remote job submission and data retrieval, and job scheduling tools designed to optimize utilization
1672 of computing resources. The Grid infrastructure will be based on the infrastructure and the software
1673 tools and services developed for the LHC Computing Grid (LCG) project.

1674 The High-Level Software Trigger (HLST) provides the online event selection. The trigger is
1675 based on an online version of the DS-50 reconstruction software, which has been optimized and
1676 tailored for the DS-20k online environment running on farms of Linux PCs and/or GPUs farms.
1677 Overall, the HLST has to provide the required rate reduction and pre-processing of raw data,
1678 including the production of global event records in analysis EDM format. The HLST will use
1679 the offline computing environment, allowing DS-20k considerable commonality in the design and

1680 management of the selection software itself. This also allows the HLST to use various offline
1681 software components, like detector description, calibrations, EDM, and reconstruction algorithms.
1682 The same infrastructure can be used for data monitoring by simply replacing or augmenting the
1683 selection algorithms with those for monitoring.

1684

11.3. Simulation

1685 G4DS is a Geant4-based simulation toolkit specifically developed for DarkSide. The modular
1686 architecture of the code was developed in order to describe the energy and time responses of
1687 all the detectors belonging to the DarkSide program, namely DS-10, DS-50, and DS-20k, but
1688 other variations of the geometries as well. For each of them, G4DS provides a rich set of particle
1689 generators, detailed geometries, real data tuned physical processes, and the full optical propagation
1690 of the photons produced by scintillation in liquid argon and by electroluminescence in gaseous argon.
1691 The main goals of G4DS are to accurately describe the light response, calibrate the energy responses
1692 in S1 and S2 and the time response expressed by the f_{90} variable, tuning of the analysis cuts and
1693 their efficiency estimation, prediction of the electron and nuclear recoil backgrounds, and definition
1694 of the signal acceptance band.

1695 G4DS tracks photons up to their conversion to photoelectrons, which occurs when a photon
1696 reaches the active region of a photosensor and survives according to the quantum efficiency. The
1697 conversion of the photoelectron into a charge signal is handled by the electronic simulation, an
1698 independent, custom-made C++ code. The electronic simulation embeds all the effects induced
1699 by the photosensors (e.g. after-pulse and cross talk) and by the electronics itself (e.g. saturation).
1700 The electronic simulation also has the option to overlap simulated events and real data baselines
1701 in order to provide more realistic simulations. As output, it produces waveforms for each channel
1702 with the same data format of the real data, in order to be processed by the same reconstruction
1703 code.

1704 G4DS can also track events generated by FLUKA and TALYS simulation codes, previously
1705 developed within the collaboration. The FLUKA simulation is mostly used to study cosmogenic
1706 neutrons and isotope productions, while TALYS is used for (α, n) reactions, both providing
1707 input for the prediction of the nuclear recoil background.

1708

12. THE ReD EXPERIMENT

1709 The ReD project aims to characterize the light and charge response of the LAr TPC to neutron-
1710 induced nuclear recoils, especially at low energy, and to explore for the possible directional de-
1711 pendence suggested by the SCENE experiment [33, 34]. ReD encompasses the irradiation of a
1712 miniaturized LAr TPC with a neutron beam at the INFN, Laboratori Nazionali del Sud (LNS),
1713 Catania. Neutrons are produced via the reaction $p(^7\text{Li}, ^7\text{Be})$ from a primary ^7Li beam delivered
1714 by the TANDEM accelerator of LNS. A $\Delta E/E$ telescope, made by two Si detectors, identifies
1715 the charged particles (^7Be) which accompany the neutrons emitted towards the TPC. Neutrons
1716 scattered from the TPC are detected by using an array of nine 3" liquid scintillator (LSci) detec-
1717 tors, using EJ309 liquid scintillator coupled to ET 9821B PMTs. The Si telescope and the TPC
1718 are not at the same height: this is mandatory in order to tag neutron scatterings (n, n') from a
1719 non-horizontal interaction plane. All LSci are placed such to tag recoils having the same energy,
1720 i.e. the same scattering angle with respect to the incident neutron, but different angle with re-
1721 spect to the drift field of the LAr TPC, thus allowing to search for a possible directional response.
1722 Thanks to the support provided by INFN CSN2, the entire set-up has been procured, integrated,
1723 commissioned and deployed to the “80 deg” beamline of LNS. The first beam run test took place
1724 in June-July, 2018.

1725 The core detector of ReD is a custom-made TPC designed by UCLA, which is a miniaturized
1726 version of the LAr TPC for DS-20k. The TPC is a cube with size of about 50 mm. An acrylic vessel

1727 defines the active volume, with the top and bottom acrylic windows ITO coated to allow for the
1728 application of the electric field, and the side ESR-acrylic sandwich reflection panels to maximize
1729 the reflectivity of the chamber. All of the internal surfaces are coated with TPB to wavelength
1730 shift the argon scintillation light. The drift field is kept uniform along the drift coordinate by
1731 means of the field shaping rings, deposited by thin-coating the walls of the acrylic vessel with
1732 ITO. The drift length, extraction length and electroluminescence length of the ReD TPC are
1733 5 cm, 3 mm and 7 mm, respectively. The ReD TPC uses all the innovative features of the DS-20k
1734 design, in particular the optoelectronic readout based on SiPM developed by FBK and the cryogenic
1735 electronics. Two 5x5 cm² tiles are available from FBK, each made by 24 rectangular SiPMs. The
1736 tile on the top of the LAr TPC has a 24-channel readout, in order to improve the (x, y) sensitivity,
1737 while the bottom tile has a standard 4-channel readout. A dedicated 24-channel Front End Board
1738 (FEB) has been designed and produced by INFN-Na in collaboration with INFN-Bo and LNGS.

1739 The LAr TPC is contained in a new cryogenic system. The commissioning of the system was
1740 carried out in Naples. Starting from April 2018, the new TPC and cryogenic system were operated
1741 and tested. Measurements were taken with lasers, low-energy γ sources and neutrons from a
1742 DD generator. This allowed for the first characterization of the LAr TPC and for an integrated
1743 test of: operating procedures, photosensors, DAQ, slow control, data handling and reconstruction
1744 algorithms. The system was successfully operated in single and double phase modes, with a light
1745 yield of about 10 phe/keV at null field. The new LabVIEW-based slow control developed by INFN-
1746 Genova was also integrated and commissioned. The set-up was irradiated in Naples with the DD
1747 neutron gun from the Temple University, such to assess the PSD performance of the LAr TPC.
1748 The run also included one LSci, allowing for the first test of the DAQ for a system made by two
1749 different types of detectors. All nine LSci detectors had been previously tested and characterized
1750 at INFN-Roma1.

1751 The commissioning and the characterization of the system in Naples opened the way for the
1752 deployment of the system at the beamline of LNS. The entire set-up (TPC with cryogenic system,
1753 liquid scintillators with their PMTs and the mechanical support structure) was shipped and re-
1754 assembled in Catania in June 2018. Meanwhile, the beamline had been refurbished on the basis of
1755 the experimental design, optimized with dedicated Monte Carlo simulations, and the mechanical
1756 clearance requirements. The configuration was conceived to allow the tagging of nuclear recoils
1757 between 20 and 100 keV traveling in the parallel and orthogonal directions with respect to the
1758 TPC drift field, by varying the primary beam energy only. Furthermore, having a dedicated liquid
1759 scintillator at small scattering angles opens the possibility to study the response of the TPC to very
1760 low-energy nuclear recoils, O(1 keV). A new scattering chamber was installed with a new beam
1761 pipe. The $\Delta E/E$ telescope was installed inside the vacuum scattering chamber, commissioned and
1762 consists of two Si detector (20 μm and 200 μm thickness, respectively) by ORTEC.

1763 Initially, the cryostat and the liquid scintillators had to be mechanically aligned with respect to
1764 the target with a precision of the order of a few mm. The alignment was performed by following a
1765 detailed procedure worked out in advance. The ReD set up in Catania is displayed in Fig. 25.

1766 After the scientific approval of the project by the Scientific Committee (PAC) of LNS, a test beam
1767 run was scheduled in June-July 2018, meant for technical tests and commissioning. The individual
1768 detectors were first commissioned and tested individually, by using the laser and radioactive sources.
1769 Light yield and timing were checked by using ²⁴¹Am and ²²Na, respectively. A ²⁵²Cf fission neutron
1770 source was used to characterize the pulse shape discrimination performance of both the LAr TPC
1771 and the LSci detectors. The light yield of the TPC was measured to be about 8.5 phe/keV, while
1772 the electron drift lifetime about 250 μs , i.e. much longer than the total drift time (about 40 μs at
1773 the operational field of 0.2 V/cm), with no hints of degradation in time. The calibration of the
1774 LSci detectors indicated a 50 % trigger efficiency at 20 keV_{ee} and a time resolution of 1.2 ns (rms),
1775 which is sufficient for the measurement of the time-of-flight.

1776 The integration of the three detector systems was done with the TANDEM beam. Neutrons were
1777 produced by sending a ⁷Li 28 MeV beam onto a set of CH₂ targets having thickness between 150
1778 and 250 $\mu\text{g}/\text{cm}^2$. The intensity of the beam impinging on the target after the collimator, measured
1779 by the Faraday Cup installed at the far end of the beam pipe, ranged between 0.5 and 7 nA. The

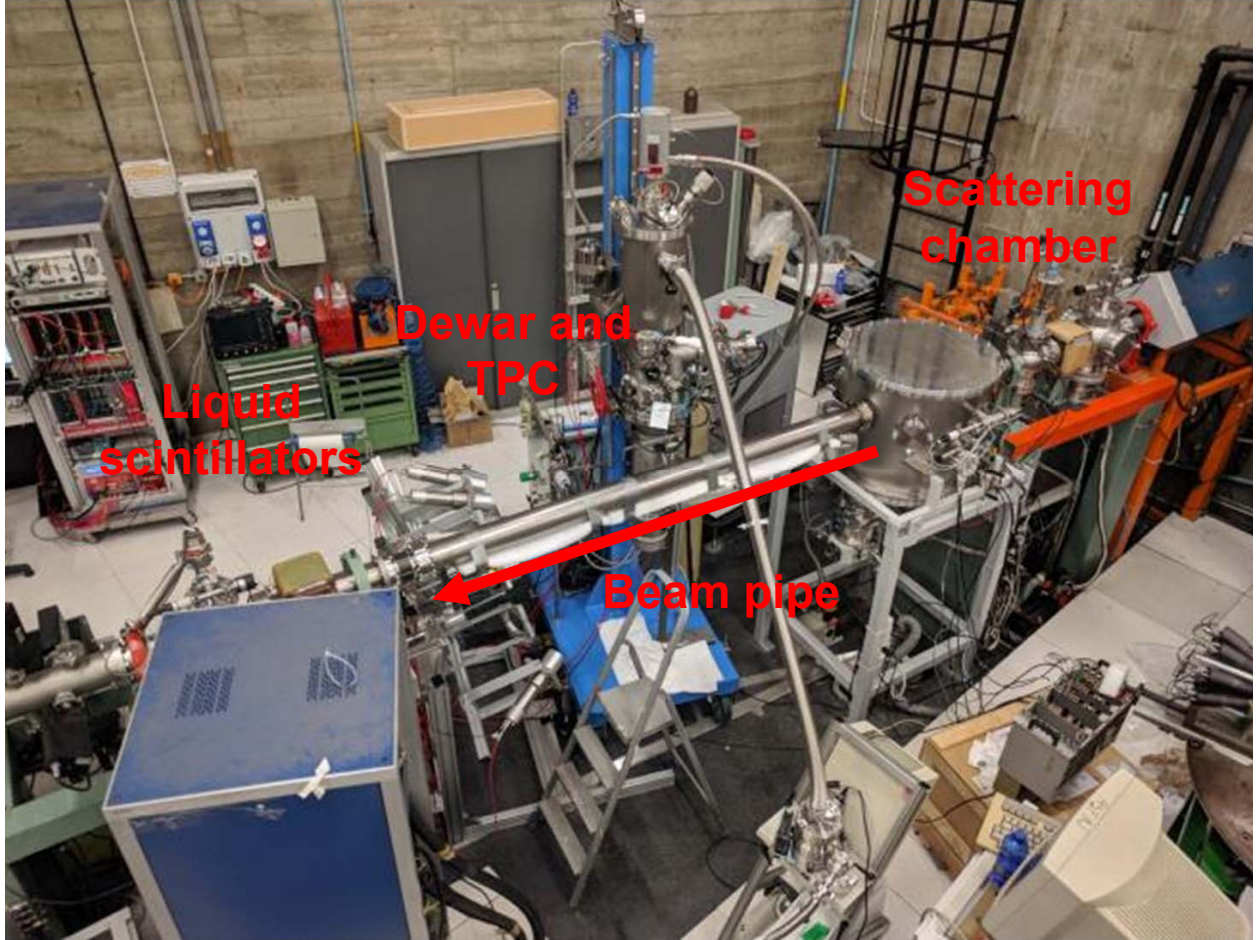


FIG. 25. Photo of the “80 deg” beamline at LNS, after the deployment and alignment of ReD. The targets and the Si telescope are hosted inside the vacuum scattering chamber.

1780 DAQ software handled 41 readout channels from three FADC boards (CAEN V1730), at 500 MHz
 1781 sampling rate. A data-to-disk rate of 40 MB/s has been achieved. The Si telescope was placed at
 1782 5 deg with respect to the beam. The scattering kinematics allows for two solutions with ${}^7\text{Be}$ in this
 1783 direction, one having an associated 7.5 MeV neutron at 22.5 deg, the other with a 2 MeV neutron
 1784 at 45 deg. The LAr TPC is at 22.5 deg from the target, i.e. it is hit by 7.5 MeV neutrons, produced
 1785 in association with the ${}^7\text{Be}$ detected by the Si telescope. The beam energy and the scattering angles
 1786 cause the experiment to select nuclear recoils in the TPC of approximately 70 keV.

1787 About 24 hours of data have been taken in the best operating conditions. Data has been taken in
 1788 both single and double phase modes and with two different trigger schemes, i.e. “Si and TPC”, “Si
 1789 and any PMT”. The latter scheme yields a large fraction of accidentals, due to the large singles rate
 1790 of the PMTs (kHz), but it gives potential access to low-energy recoil in the TPC, which would fail
 1791 to trigger the TPC (low S1, or S2 only). Those events can later be searched for offline in the data
 1792 analysis. Typical trigger rates were between 0.1 and 0.7 Hz. Events were observed with the proper
 1793 signature, i.e. a ${}^7\text{Be}$ nucleus detected by the telescope, a nuclear recoil in the LAr TPC and a
 1794 neutron scattering in the liquid scintillators. Neutron-induced recoil events in the TPC and in the
 1795 LSci detectors are clearly separated from γ signals, either physical or accidental, by means of pulse
 1796 shape analysis. As expected, the time difference Δt between the pairs of detectors features a peak of
 1797 physical coincidences, sitting on a plateau of accidentals. The scatter plot of the amplitudes of the
 1798 ΔE and E Si detectors is displayed in the left side of Figure 26. It shows the ability of the telescope
 1799 to discriminate the charged products of the beam-target reactions, i.e. the main ${}^7\text{Li}$ band due to
 1800 elastic scattering and the two ${}^7\text{Be}$ loci corresponding to the two solutions allowed by kinematics.

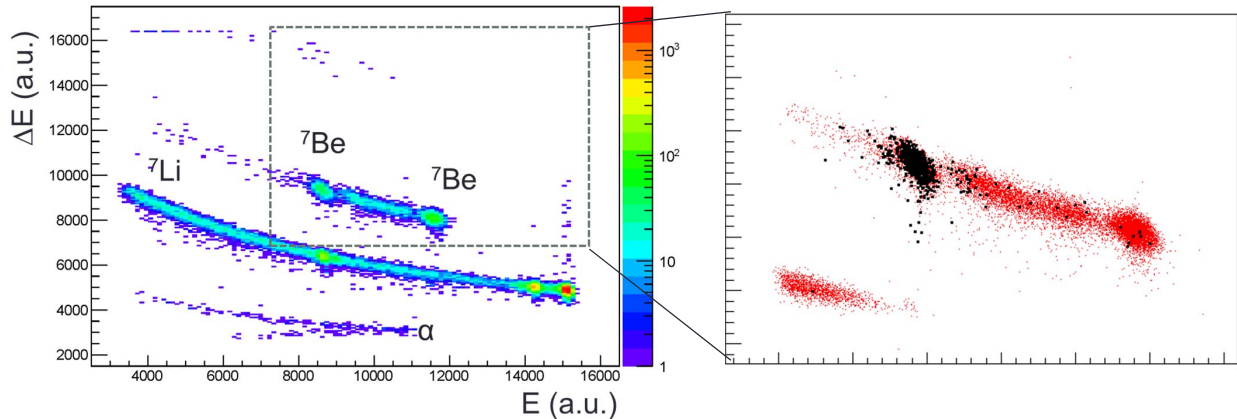


FIG. 26. **Left:** scatter plot of the amplitudes of the ΔE and E Si detectors, placed at 5 deg with respect to the beam axis. **Right:** zoom of the previous scatter plot in the region of the ${}^7\text{Be}$ *locus*; the black markers are events having a coincident signal in the TPC.

1801 The right side of Figure 26 shows the same distribution (zoomed), with the black markers referring
 1802 to the events having a coincident signals in the TPC. As expected, coincident events between Si
 1803 and TPC are mostly associated to ${}^7\text{Be}$ *locus* from the “correct” kinematical solution.

1804 After another LNS test beam in September 2018, the ReD TPC has been transported back to
 1805 Naples, to complete the characterization and re-commissioning in the lab there. Tests have been
 1806 performed to characterize the basic TPC performance in terms of light yield, uniformity, electric
 1807 field configuration and S2/S1 ratio in double phase. The system was calibrated with ordinary
 1808 γ -sources and with an internal ${}^{83m}\text{Kr}$ source, which generates a uniform distribution of mono-
 1809 energetic events. Activities are still ongoing to characterize the extraction and multiplication fields.
 1810 A campaign was also carried out at LNS to measure the neutron detection efficiency of the liquid
 1811 scintillators, using a fission ${}^{252}\text{Cf}$ source. A test beam for the characterization of the neutron beam
 1812 is going to be performed at LNS in June 2019 and for this run only the Si detectors and the LSci
 1813 detectors will be deployed.

1814 The ReD project has received scientific approval by the Scientific Committee of LNS (PAC) for
 1815 a five-week beam allocation that is granted for 2019. Upon completion, the ReD LAr TPC will be
 1816 transported back to Catania and a new beam run with the full setup will be scheduled.

1817

13. DARKSIDE-PROTO

1818

13.1. Prototype Overview and Status

1819 The objective of the DS-Proto experiment is the construction and operation of a prototype de-
 1820 tector of intermediate size (~ 1 t), to fully validate the new DS-20k technologies for their integrity in
 1821 both the mechanical and functional aspects. The prototype will be constructed using the materials
 1822 planned before screening, in order to speed up the mechanical validation, and will therefore not
 1823 necessarily be a physics-results oriented detector. This may evolve over time to include elements
 1824 of the detectors as materials are screened and made available, and eventually all parts could be
 1825 replaced with radio pure materials to form the basis of another experiment with high-sensitivity to
 1826 low-mass WIMPs. Thus, DS-Proto is not intended to replace validation and tests made in labora-
 1827 tories, but rather complement them with the integration with the rest of the detector. The prompt
 1828 execution of DS-Proto is crucial to fulfill the overall schedule of DS-20k. DS-Proto is on the critical
 1829 path of the project.

1830 The program for DS-Proto is expected to span over three different phases:
 1831 1. Design, construction and assembly at test site of the LAr TPC, with the size available for two
 1832 motherboards integration;



FIG. 27. The DS-Proto cryostat and components delivered at CERN.

- 1833 2. Integration of 50 preproduction PDMs to the LAr TPC; assembly, commissioning, and operation
 1834 of full read-out and DAQ for 50 PDMs; The xy resolution and S2 gas pocket optimization will
 1835 be done during this phase.
 1836 3. Assembly and commissioning of full system, including 370 first production PDMs; full readout
 1837 and DAQ operational; evolution towards final configuration.

1838 The plan for DS-Proto was reviewed, approved, and funded by the CNS2 of INFN. Funding has
 1839 already been secured from the NSF for the development and fabrication of multiple components for
 1840 the TPC, the cryogenics system and resources for kick-starting the UAr extraction site preparations.
 1841 Requests for funding from other participating groups are being evaluated or will be submitted in
 1842 the near future.

1843 In August 2017 the collaboration and LNGS reached and finalized an agreement [60] with the
 1844 Accelerator & Technology Sector of CERN and its Technical Division to construct and commis-
 1845 sion the DS-20k cryogenics at CERN, with support from the Cryogenics Group and the Vacuum,
 1846 Surfaces and Coatings Group (both groups are part of CERN's Technical Division). The extension
 1847 of this program to carry out the first surface operation of DS-Proto at CERN before moving the
 1848 detector to LNGS was agreed by the CERN Accelerator & Technology Sector via an Addendum
 1849 to the above agreement. The necessary space and facilities are the same as for the test on the
 1850 DarkSide-20k cryogenics and are already allocated.

1851 A cryostat for DS-Proto has been built by Tecno Alarm, s.r.l., Roma, and delivered to CERN in
 1852 August 2018 (see Figure 27). The 1 mBq/kg U/Th AISI 304 L Stainless Steel was procured from
 1853 NIIRONIT Edelstahlhandel GmbH & Co and it is good enough to be used for a possible physics
 1854 run in LNGS.

1855 Assembly and test of the DS-20k cryogenics will take place at CERN, during the summer and
1856 last quarter of 2019. Construction of DS-Proto is expected at the end of 2019 or early 2020. The
1857 first test operation with a reduced number of photosensors is expected by summer 2019, followed
1858 by a second operation with a full complement of PDMs by early 2020. Full characterization of the
1859 prototype performance and physics runs will be performed after installation at LNGS. The detailed
1860 program of the activities to be carried out underground is under study.

1861 We anticipate that, since the DS-Proto will be a stand alone system, sharing the DS-20k cryo-
1862 genics system at LNGS will not be possible. However over the past few years of R&D for the
1863 DS-20k cryogenics, we have realized and tested several key components which will be more than
1864 capable of handling the prototype system. These parts can be used for DS-Proto with minor system
1865 integration together with most of the DS-50 and existing R&D devices.

1866

13.2. The DS-Proto TPC

1867 The DS-Proto TPC mechanics, including the structural elements, the field cage, the reflector cage,
1868 the transparent cathode, the transparent anode (also serving as a diving bell for the containment
1869 of the gaseous phase), the SiPM PDM assemblies, the high-voltage feed through system, will all be
1870 built utilizing, on a scaled down overall dimension, the same design and construction techniques
1871 foreseen for the baseline of DS-20k (see Figure 28).

1872 The photodetector modules will be arranged to cover the top and bottom of the TPC. Both
1873 top and bottom planes consist of 185 photodetector modules assembled into 5 SQBs and 4 TRBs.
1874 As described in section 10, the readout chain will employ commercial components used during the
1875 first phase, allowing for full digitization of the signals. The final electronics components that will
1876 be used in DS-20k will be used as they become available at each stage of the development. It is
1877 also foreseen that the optical signal transmission will be tested on a significant number of channels
1878 with this detector.

1879 The DS-Proto photosensors are contained in 18 Motherboards made of one set of 5 (SQB) and 4
1880 (TRB) PDMs on top, and another identical set on bottom. With both planes, the DS-Proto TPC
1881 requires 370 PDM to be fully covered. Bonding ~9000 SiPMs in a few months is one of the most
1882 critical tasks of this detector, to maintain the overall project schedule. The construction strategy
1883 relies on two bonding facilities, the first one located at Princeton University and the second one
1884 at LNGS. According to the experience gained in the past months, a bonding rate of 3 tiles /d is
1885 feasible. We therefore need 60 d to bond the 370 tiles across the two facilities.

1886 The man power at LNGS can be provided by the NOA contracts, while finding man power at
1887 Princeton University is more challenging. Different options were evaluated, and others are under
1888 consideration. The University of Manchester (UK) has identified a candidate who will spend a
1889 significant amount of time in the course of the next year to be trained, and then do the work. A
1890 tight connection between the two production sites has to be provided, to include the harmonization
1891 of the procedures and quality assurance test. A person to provide this interface is being identified.
1892 LNGS requires a significant increase of man power since after the bonding the tiles will be equipped
1893 with a Front End Board (FEB), and then mounted and tested at LNGS. After the assembly, the
1894 tiles and the FEB will be tested in LN₂. The first Motherboard, made of 25 PDMs, was just
1895 assembled. The Motherboard will be shipped to Napoli, where a comprehensive test at cryogenic
1896 temperature is scheduled.

1897 A powerful test facility has to be prepared at Napoli, requiring extra man power. The procedures
1898 and the tools to ship the Motherboard from Pisa to Napoli and from Napoli to CERN have to be
1899 carefully planned and made available.

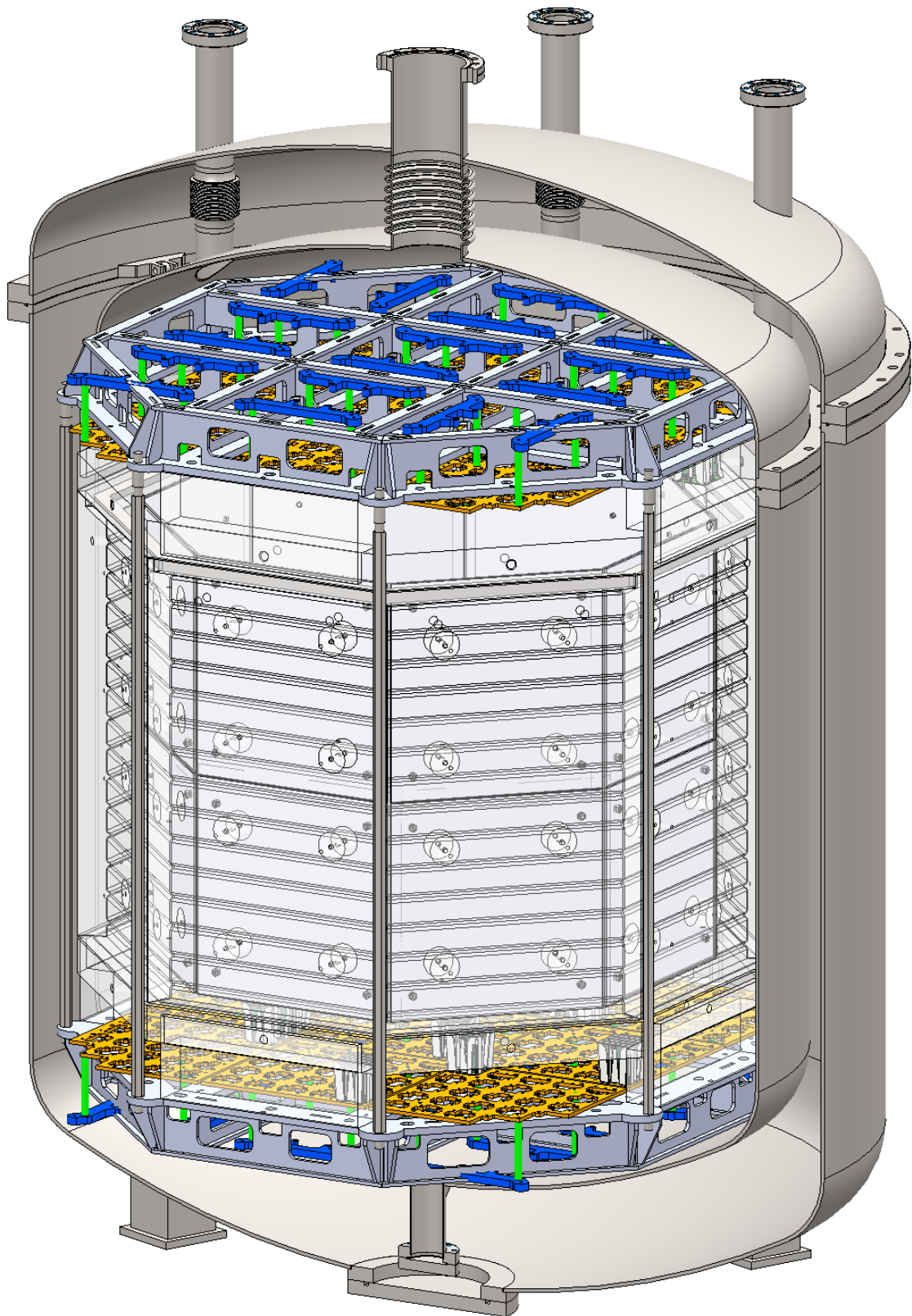


FIG. 28. Conceptual Design of the DS-Proto detector. The cryostat has already been built and delivered at CERN, see Fig. 27.

1900

13.3. Materials for DarkSide-Proto

1901 Since DS-Proto is a test bench of DS-20k, it won't be used to demonstrate the material radio-
 1902 purity requirements of DS-20k, however, it will be built with the goal of achieving the best radio-
 1903 purity conceivable at the time of the construction, based on the current results of materials assay
 1904 campaign. Additionally, DS-Proto can be used to assess the possible contamination related to the
 1905 detector construction procedures (TPC and PE), evidencing material cleaning/handling issues.

1906 The assessment of the DS-Proto radioactive budget will be obtained through the material assay
 1907 campaign and the Monte Carlo simulation. The validation of the predictions concerning the neu-
 1908 tron/gamma originated by the material contamination will be only possible through data taken
 1909 underground with the DS-Proto deployed in a properly shielded environment. A physics run, fo-
 1910 cused on the low-mass WIMP search, will be eventually possible with the S2-only analysis in the
 1911 keV region. In this context, the minimization of the low-energy gamma background of the prototype
 1912 will be extremely important to employ as early as possible.

1913

13.4. Validation tests and operation

1914 Upon successful completion of the test phase of the different parts, we plan to measure the overall
 1915 performance of the DS-Proto through some key parameters, such as the S1 light yield, the electron
 1916 drift time, electro-luminescence field and gas pocket thickness uniformity for high resolution of S2
 1917 signals and the xy position reconstruction. For the purpose of optimizing the S2 signals, the first
 1918 two Motherboards will be assembled into a small TPC with reduced size drift length (12 cm) to
 1919 avoid pile-up (see Figure 29). Full test of the S1 response and therefore of the SiPM readout chain
 1920 can be obtained at the surface by switching off the electroluminescence field. The configuration of
 1921 the gas pocket (geometry and field) can be varied by changing the distance between the anode and
 1922 the wire grid, the width of the gas pocket, as well as the electro-luminescence field. The S2 pulse
 1923 shape can be precisely studied along with different gas pocket configurations, aiming to provide
 1924 us the best solution for the future LAr TPC design. This set-up will also allow for early studies
 1925 of the S2 formation and readout, to be carried out while the pre-production of the remaining
 1926 Motherboards of the prototype is ongoing.

1927

14. AAR CRYOSTAT

1928 Figure 1 shows the DarkSide-20k system conceptual sketch, including the copper electromagnetic
 1929 and light shield, the Veto detector and the LAr TPC, all contained within the large AAr cryostat.
 1930 A ProtoDUNE-like cryostat will be employed to house the LAr bath which the TPC is immersed
 1931 in and also acts as the main component of the Veto detector. This allows to minimize the material
 1932 of the TPC vessel and therefore to limit the possible radio-contaminations very close to the active
 1933 volume.

1934 Figure 30 shows the finished ProtoDUNE cryostat internal view while being cleaned, as well as
 1935 the layout of passive thermal insulation materials that were used to construct the cryostat. The
 1936 design concept for the DS-20k cryostat is based on the experience matured with the construction
 1937 of ProtoDUNE cryostat. The technique is adopted from the LNG (Liquified Natural Gas) carriers
 1938 and vessels, which has proven over many years its solidity and reliability.

1939 Two cryostats of the same size as the one proposed here have been constructed at CERN and one
 1940 of them has been brought into operation in the second half of 2018. The experience gained there in
 1941 the design, construction and operation will be fully translated to the DS-20k project, through the
 1942 involvement of the CERN group that was responsible for the construction and operations of the
 1943 ProtoDUNE cryostat. For that reason, the same mechanical constraints, dimension and thermal
 1944 properties have been kept. The DS-20k cryostat is an improved version based on the experiences
 1945 gained during the construction of the two ProtoDUNE cryostats, namely optimized fabrication and

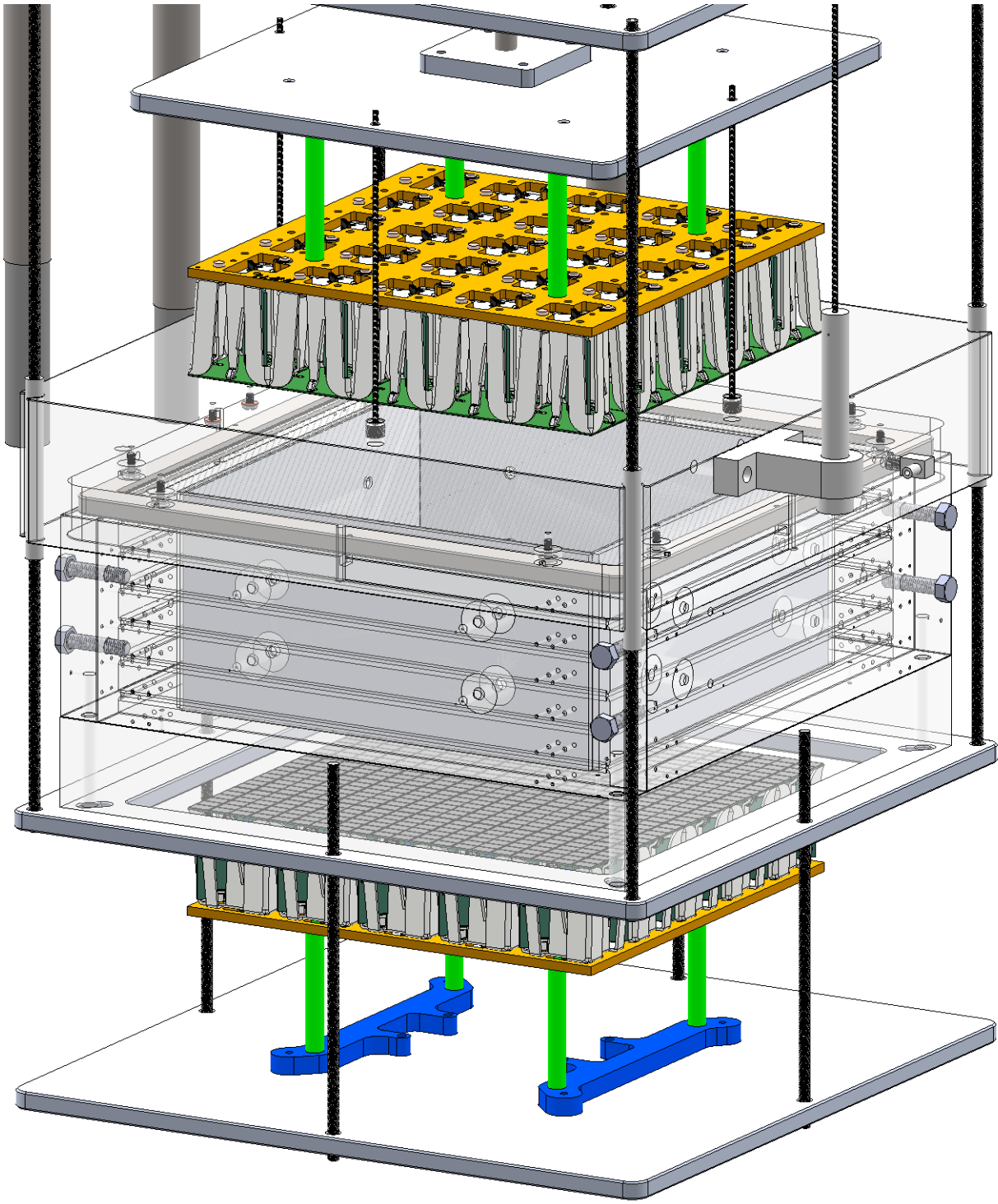


FIG. 29. Schematics of the setup for the optimization of the S2 signals.

¹⁹⁴⁶ construction and access specific for DS-20k project. A 3D conceptual view of the external part of
¹⁹⁴⁷ the cryostat being planned for DS-20k is shown in Figure 31.

¹⁹⁴⁸ To make it as easy as possible for the access and support of the sub-systems of the TPC and the
¹⁹⁴⁹ Veto detectors, all components will now be inserted from the roof of the cryostat, with a “closing
¹⁹⁵⁰ cap” concept being implemented. This has been previously deployed by the CERN team during
¹⁹⁵¹ other large-dual phase TPC R&D experiments and tested with the construction and operation of

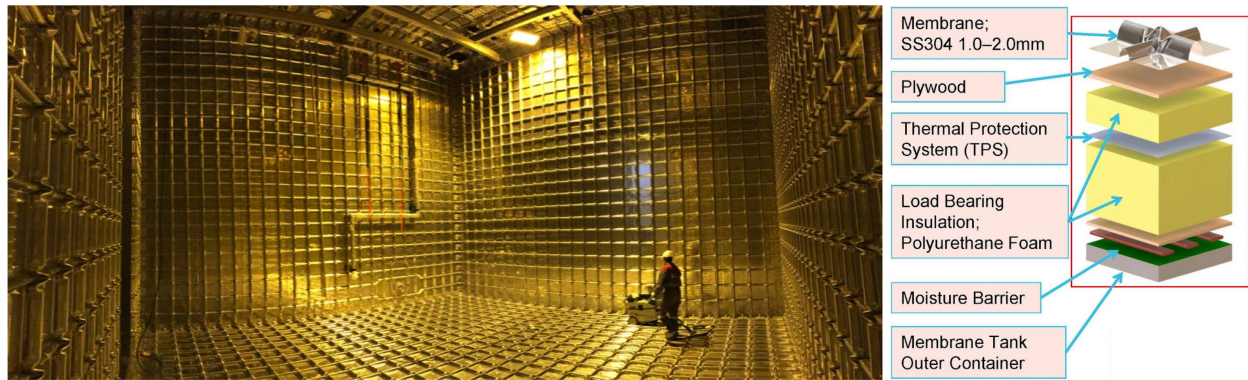


FIG. 30. **Left** Interior view of the ProtoDUNE cryostat used for the single phase LAr TPC test at CERN. **Right** Cryostat insulation construction details from GTT.

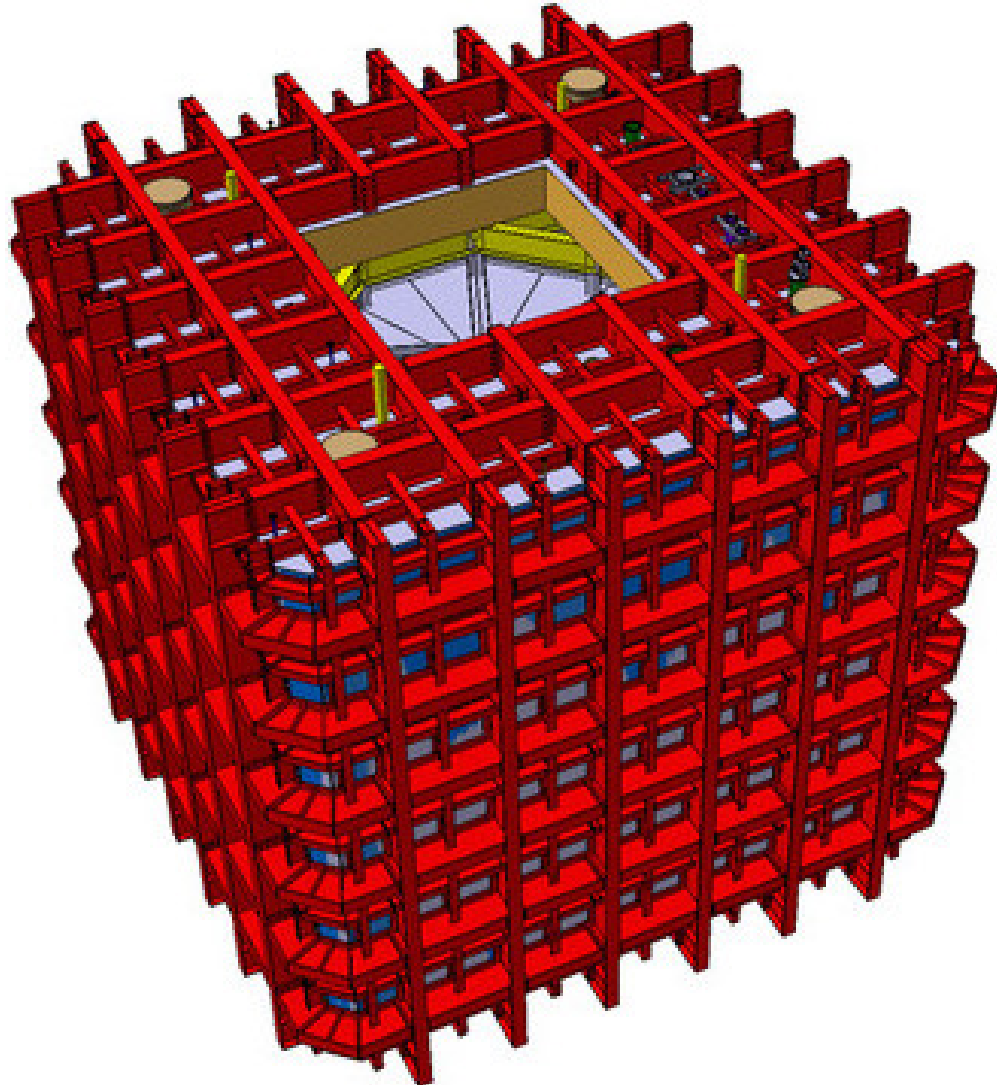


FIG. 31. 3D conceptual external view of the DS-20k AAr cryostat.

1952 the first demonstrator for the ProtoDUNE project. A cross-sectional view of the concept is shown
 1953 in the right side of Figure 32. The plan is to assemble the bottom and sides of the Veto detector

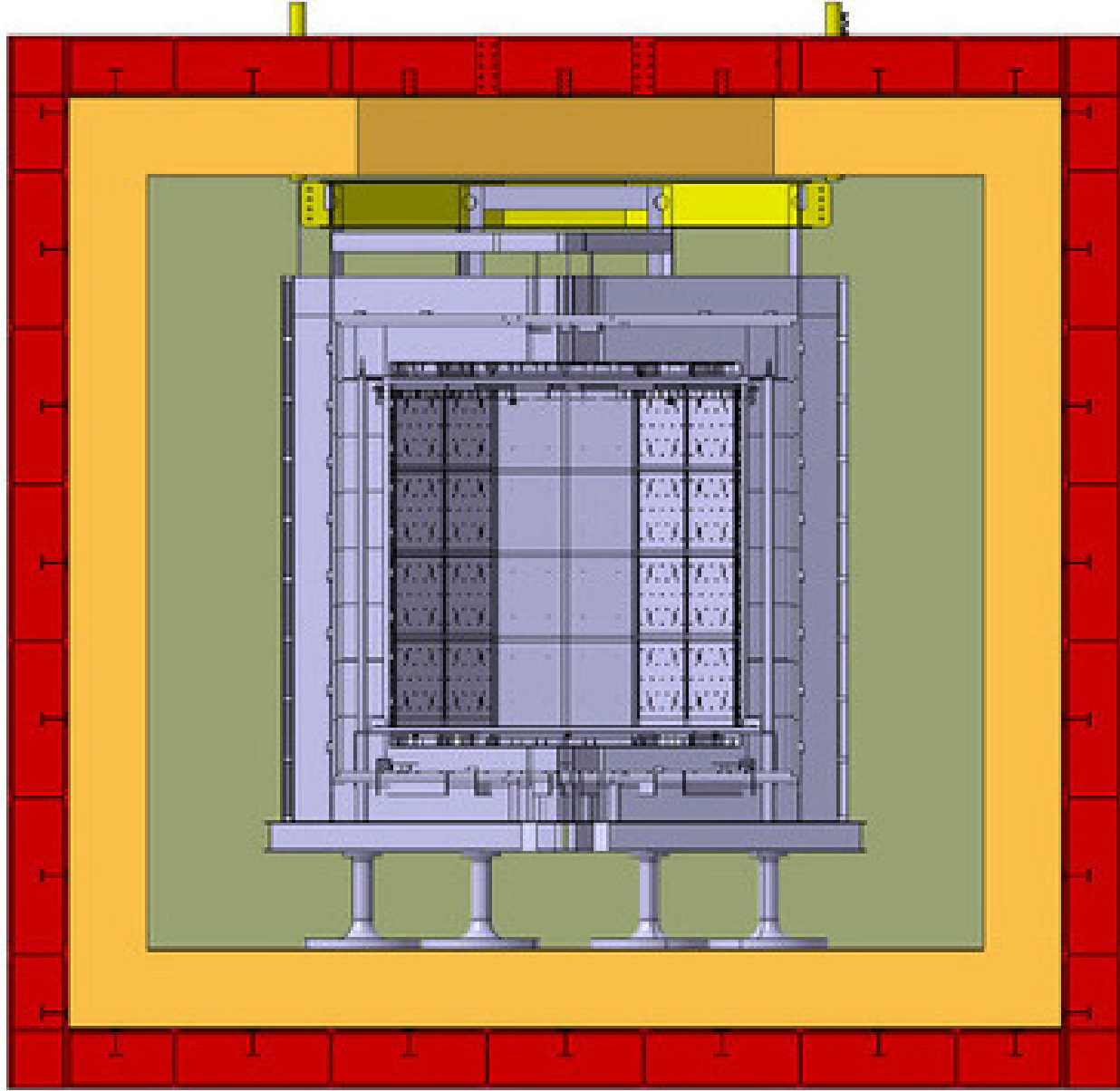


FIG. 32. Cross-sectional view of the large AAr cryostat containing the LAr TPC and Veto detectors and showing the top-cap concept.

1954 using a temporary support frame underneath the Veto detector, and then lower the TPC down into
 1955 the Veto detector while it is attached to the closing cap, see Figure 24. Once in place, the remaining
 1956 parts of the Veto detector could be assembled, the entire detector system support transferred to the
 1957 detector support system of the cryostat, and finally the temporary supports of the Veto detector
 1958 that we required during construction removed. At this point, the two detector volumes, that of the
 1959 TPC and that of the Veto, would be filled simultaneously such that the LAr height in both volumes
 1960 is equal at all times in order to reduce the mechanical stress on all of the detector components.

1961 As mentioned in Sec. 6, the AAr cryogenics system will be built based on the combined expe-
 1962 riences of the ProtoDUNE cryogenics and the DS-50 cryogenics. The final optimization decision
 1963 will be made taking into account that the different requirements of the AAr cryostat for DS-20k
 1964 compared to those for ProtoDUNE, and the available space in Hall C of LNGS. Penetrations on the
 1965 roof of the cryostat are being finalized such to meet the requirements of the other sub-systems, as
 1966 well as to provide the mechanical stability of the cryostat ceiling. The design and development plan

Element	Inlet Purity [ppm]
CH ₄	<0.25
CO	<0.1
CO ₂	<0.1
H ₂	<1
H ₂ O	<1
N ₂	<1
O ₂	<1

TABLE VIII. Inlet argon purity required for operation of the DarkSide-20k getter.

will follow the successful experience of ProtoDUNE, with expert engineering assistance provided by the CERN group, while already a firm baseline design is in place and schematically shown in the left side of Figure 17, along with the rest of the DS-20k cryogenics system.

15. ARGON PROCUREMENT AND PURIFICATION

A broad strategy has been developed to increase the production of UAr to procure the target required for DarkSide-20k. The Urania project will extract and purify the UAr from the CO₂ wells at the Kinder Morgan Doe Canyon Facility located in Cortez, CO, at a production rate of 250 kg/d. It will be necessary to make a final chemical purification of the UAr before deployment into the LAr TPC (driven by the filtration capacity of the getter purification unit), bringing the chemical impurity levels to those shown in Table VIII. Additionally, it would be beneficial to further deplete the UAr of ³⁹Ar, giving extended sensitivity to DarkSide-20k and producing argon with a level of ³⁹Ar that is acceptable to be used in an experiment such as Argo. The Aria project will serve to chemically purify the UAr to better than the levels shown in Table VIII using a cryogenic distillation column called Seruci-I. The ultimate goal of the Aria project is to process argon through Seruci-I to achieve an additional depletion factor between 10 and 100 (on top of the reduction of ³⁹Ar already seen in the UAr).

The procurement of the UAr for DarkSide-20k is broken into two main operations, extraction of the UAr by Urania and then chemical purification by Aria using Seruci-I.

15.1. Urania

The Urania project will extract at least 60 t of low-radioactivity UAr, providing the required 51.1 t of UAr to fill DarkSide-20k. The Urania project will also lay the groundwork for UAr procurement for future, larger argon-based detectors such as Argo. The goal of the Urania project is to build a plant capable of extracting and purifying UAr at a rate of 250 kg/d, from the same source of UAr that was used for the DarkSide-50 detector.

The opportunity to build Urania has grown from the strong relationship between the DarkSide Collaboration and the Kinder Morgan Corporation. Based on gas analysis of the Cortez stream provided to Kinder Morgan by the DarkSide Collaboration during the extraction of the DarkSide-50 UAr target, a major industrial partnership between Kinder Morgan and Air Products was established in order to extract helium from the CO₂ at Kinder Morgan’s Doe Canyon facility. The Air Products helium plant began operation in July 2015 and presently supplies 15 % of the production rate to the National Helium Reserve.

The DarkSide Collaboration reached an agreement with Kinder Morgan to feed the Urania plant with a small fraction (15%) of the gas stream returned to Kinder Morgan by Air Products after helium extraction. This gas stream holds two significant advantages over the gas stream used to extract the UAr for DarkSide-50: it is completely dehydrated, and it contains only trace amounts of helium. These features greatly simplify the process for UAr extraction by the Urania plant, while ensuring the same radioactivity levels, or better. Argon from the active CO₂ wells in south-

2004 western Colorado have been found to contain very low levels of the radioactive isotope ^{39}Ar , with
2005 the concentration shown to be a factor of $(1.4 \pm 0.2) \times 10^3$ below that of argon derived from the
2006 atmosphere [5]. In an effort lasting more than 5 years, DarkSide-50 collaborators at Princeton
2007 and Fermi National Accelerator Laboratory (Fermilab) extracted and purified (156 ± 1) kg of UAr,
2008 slightly more than the (153 ± 1) kg needed for the target material in the DarkSide-50 detector.

2009 The Urania feed gas stream is $\sim 95\%$ CO₂, plus a few percent of N₂, one percent CH₄, 430 ppm
2010 of UAr, and traces of higher hydrocarbons. The processing scheme of the UAr extraction plant is
2011 optimized for this feed composition in order to achieve an UAr purity of better than 99.9%. A
2012 modular plant consisting of skid-mounted units deployable on concrete platforms is being designed
2013 to carry out the processing.

2014 The UAr extraction plant will consist of three gas-processing units, as shown in Fig. 33, followed
2015 by a cryogenic distillation unit. The gas-processing units are two CO₂ liquefier/strippers followed
2016 by a pressure swing adsorption unit (PSA). The first liquefier accepts gas at (49 ± 1) bar, with
2017 a flow rate of 16 250 std m³/h and a temperature of 5 °C. At these conditions, the CO₂ partially
2018 condenses and the stream is separated into 2-phases (gas/liquid) as it goes to the first stripper.
2019 In the column a controlled quantity of heat is given by a hot fluid working between the chiller
2020 condenser and the column reboilers. The light products are vaporized and recovered from the top
2021 of the column in gas phase. The heavy products (mainly CO₂) are collected from the bottom,
2022 compressed to 120 bar and returned to Kinder Morgan as a liquid. The light products coming
2023 from the column head are cooled down in the second step to approximately -50 °C and sent to the
2024 second stripper. The first column produces 1300 std m³/h of product flow, a factor of 5 reduction
2025 in the amount of gas to be processed by the more complex downstream units.

2026 The second liquefaction and stripping unit further reduces the CO₂ content, in a similar process
2027 as the first stripping unit. The separated CO₂ is joined with that from the first unit and returned
2028 to Kinder Morgan. The product gas from the second stripper is re-heated in a heat exchanger
2029 and delivered to the PSA unit, which separates the light fractions, including the argon, from the
2030 remaining CO₂. The PSA is composed of four adsorption beds to allow continuous operation with
2031 short time adsorption cycles. The desorption of CO₂ is made by decreasing the pressure on the bed.
2032 To optimize the performances, the operation of the adsorbers are combined by coupling the purge
2033 and pressure swing phases. At the outlet of the PSA adsorption tanks, one buffer tank is provided
2034 in order to dampen process fluctuations and allow for continuous operations of the final distillation
2035 process. The PSA off-gas is delivered to a recycle compressor and sent back to the second CO₂
2036 stripper inlet for reprocessing.

2037 The PSA is the most critical unit of the entire process since the dynamic adsorption conditions
2038 are the most difficult to simulate and predict. Optimization of the sorbent and other operational
2039 parameters is being done via a small scale lab setup in which breakthrough tests are being performed
2040 for a variety of gas species. A picture of the test setup being used is shown in Fig. 34. Sorbent
2041 screening relies on measurements of the breakthrough curves of the different gas species for the
2042 candidate sorbents. A selection of sorbents which could work for the PSA unit have already been
2043 identified, while the final selection of the exact sorbent to be used in the UAr extraction plant will
2044 be determined by the test results and consultation with the contracted company who will build the
2045 plant.

2046 The final unit of the UAr extraction plant consists of three cryogenic distillation columns. The
2047 CO₂-free product coming from the PSA plant is pre-cooled and sent to the first column, which
2048 works at a lower pressure (~ 9 barg) for the removal of CH₄. The second column is used to remove
2049 the remaining light fractions from the resulting N₂-rich stream, and the third to perform the final
2050 purification of the UAr using a batch distillation process. In addition to removing the CH₄ and N₂
2051 at this point, any ⁸⁵Kr present in the stream will also be removed by the series of three cryogenic
2052 distillation columns. The CH₄-rich and N₂-rich distillation wastes are returned to Kinder Morgan
2053 along with the CO₂. The final product, 99.9% pure UAr, will be taken in liquid form from the
2054 top of the last column and a small portion collected into a tank to check the quality of the argon.
2055 The majority of the liquid UAr will be sent to the appropriate cryogenic vessels for shipment to
2056 Sardinia, where it will undergo final chemical purification by the Seruci-I column.

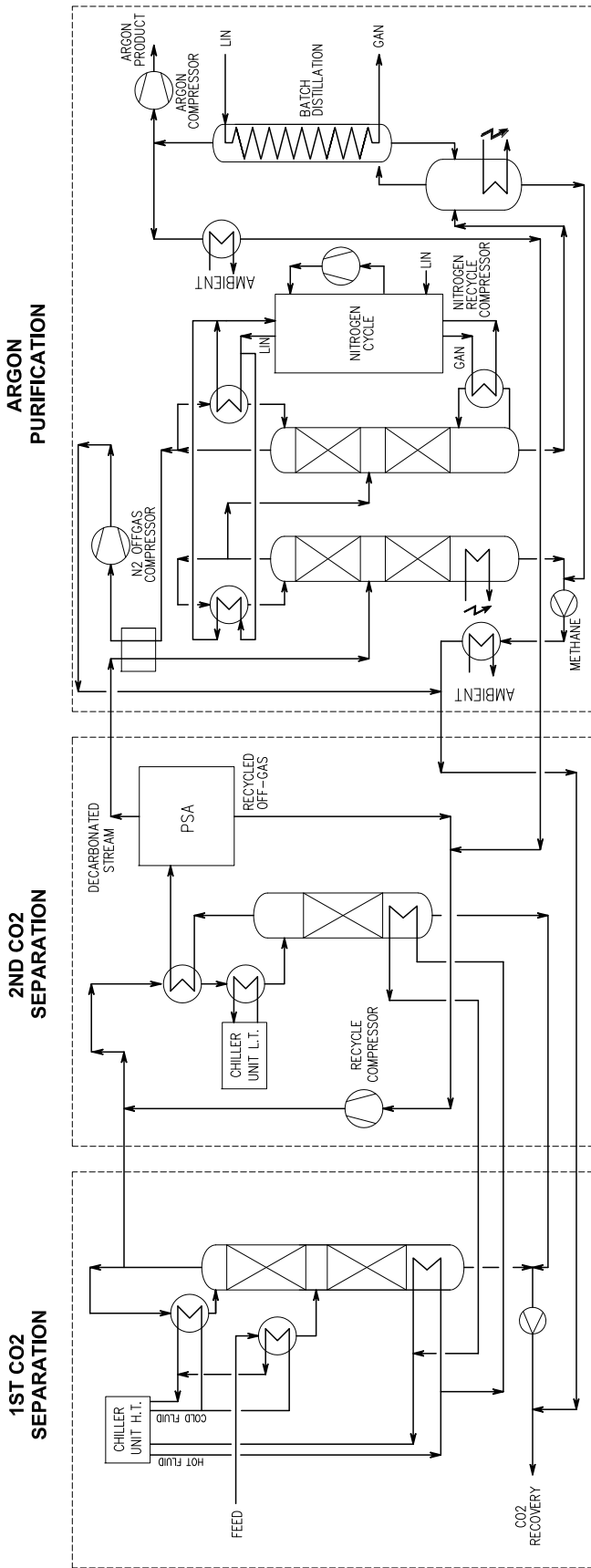


FIG. 33. Process Flow Diagram (PFD) for the Urania UAr extraction plant.



FIG. 34. Test plant in use at Università degli Studi di Napoli “Federico II” for the characterization and selection of sorbents for the PSA unit of Urania.

2057 The Urania project has recently made significant strides, most importantly with the opening
 2058 of the tender for the construction and shipment of the argon extraction plant by the INFN. The
 2059 opening of the tender has officially marked the start date for the progression of the sub-project
 2060 schedule, and the timeline for the extraction of the 60 t of UAr required for the DS-20k experiment
 2061 has now been set and has been integrated with the overall project schedule. It is now expected
 2062 that the tender process will close at the beginning of the fourth quarter in the 2019 calendar year,
 2063 and at that point a contract will be executed for the construction and delivery of the plant to the
 2064 extraction site in Colorado, USA.

2065 The tender for the construction of the argon extraction plant has been opened and the winner
 2066 will be selected and contract signed by the end of October, 2019. The plant will be delivered to the
 2067 Kinder Morgan Doe Canyon Facility by the end of 2020 calendar year. The current plan is to install
 2068 and commission the plant in the first three quarters of 2021 calendar year, allowing for extraction
 2069 of the 60 t of UAr by the middle of the 2022 calendar year, in order to meet the DarkSide-20k
 2070 schedule. The preparation of the extraction site is being planned now and will be managed by the
 2071 collaboration with help from the Kinder Morgan CO₂ Company and the contractors hired to carry
 2072 out the work. Site preparations for developing the facility before the arrival and installation of the
 2073 plant will begin as soon as the necessary land development permits have been secured and the RFQ
 2074 process has been completed.

2075 The shipment from Colorado to Sardinia will be done by boat in order to minimize the cosmic
 2076 activation of the argon. For the shipment of the UAr from Colorado, two options are under
 2077 investigation. The first option, which was determined to be the baseline method, is to ship the
 2078 UAr in liquid phase using custom built cryogenic vessels. This is a more efficient and cost effective
 2079 method, compared to shipping the UAr in gas phase. The custom built cryogenic vessels will have
 2080 a double wall structure, there will be two inner volumes with the larger one containing the UAr and
 2081 the smaller containing LN₂. The outer volume would be at ultra-high vacuum to thermally insulate
 2082 the two inner volumes from the atmosphere at ambient temperature. During the transport, a LN₂
 2083 fed condenser would slowly re-liquify the UAr as it evaporated away, ensuring that none of the UAr

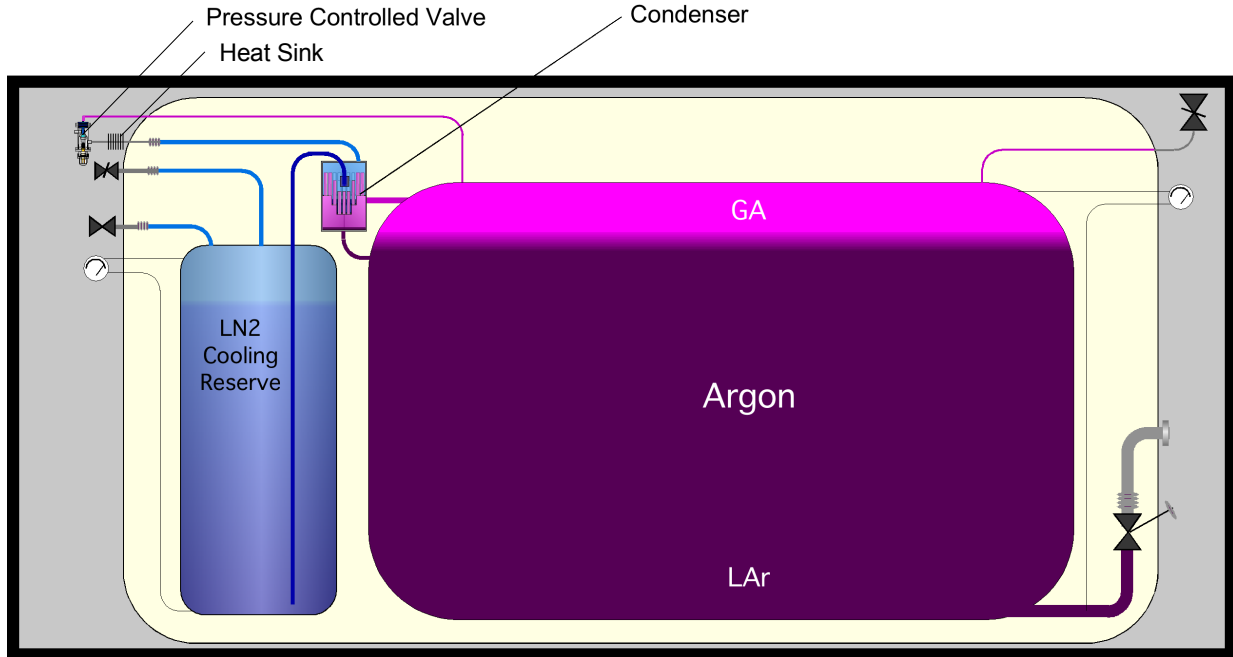


FIG. 35. Schematic view of the cryogenic shipping vessel design, one of the two options for argon shipment from Colorado to Sardinia.

would be lost during the trip. A schematic view of the cryogenic vessel design is shown in Fig. 35. A minimum of five cryogenic vessels is foreseen enabling one for Urania production, one for Aria feed, one for Aria production, and two traveling between Sardinia and LNGS for delivery and then LNGS and Sardinia for further production of UAr, at all times.

In the case of cryogenic shipping, the extracted UAr will be shipped to Sardinia in batches of 11 t (roughly every 100 days) in liquid phase, also eliminating the need to liquify the UAr to be reprocessed by the Aria column. After chemical purification in Aria, the UAr will then be shipped to LNGS, also in batches of 11 t, and stored in the argon recovery system. In order to minimize the exposure to cosmic rays, the argon will be stored underground at Seruci and/or LNGS for any necessary long durations.

The second option that is now being investigate as an alternative, is to ship the UAr in high-pressure gas cylinder placed in trailers which can be hauled by trucks. This option is made possible by special cylinders which allow for the storage of argon at pressures up to 400 bar. With pressures of this magnitude, and cylinders that are able to be the size of large trailers, the number of trailers that would be required for the total DS-20k detector target is something that is manageable, on the order of 10 to 20 depending on the storage pressure. The overall benefit of moving to this option, instead of going with the cryogenic vessel option, is that the gas can be maintained in the cylinders for years without the need of any type of consumable to prevent the loss of the argon. This would basically eliminate the risk of losing any of the UAr during the transport and storage, other than potential loss of the shipment.

The Urania project team is now collecting all of the information that is required to make the technical and economic assessment of the two options. Based on the technical risks and the economic impact on the project, the option that is best for the overall project will be chosen.

15.2. Aria

The aim of Aria is to perform chemical purification of the UAr extracted by Urania. Aria will also be the test bench to develop active depletion of ^{39}Ar from the UAr to possibly provide DAr targets for future larger-scale LAr detectors. Aria consists of a 350 m tall distillation column, Seruci-I,

2111 capable of separating isotopes with cryogenic distillation, a process that exploits the tiny difference
2112 in volatility due to the difference in isotopic mass [61–66].

2113 The design of the plant started in April 2015 with seed funding from the US NSF through
2114 PHY-1314507. Aria is to be installed in a underground vertical shaft of 5 m diameter and 350 m
2115 depth, located at the Seruci mine campus of CarboSulcis, a mining company owned by the Regione
2116 Autonoma della Sardegna (RAS). In February 2015 a proposal was submitted to the Italian INFN
2117 and RAS, and the funding for the Seruci-I column was approved on July 24, 2015. Construction
2118 of Seruci-I modules started in September 2015 in a Italian company.

2119 The measurements of the relative volatility of argon isotopes [67–69] and their theoretical inter-
2120 pretation [70–72] marked the birth of the Italian school of condensed matter in Genoa and Milan.
2121 The study of the relative volatility of argon isotopes was recently revisited [73, 74] and shows a
2122 promising path for the separation of ^{39}Ar from ^{40}Ar . Following these studies, DarkSide collabora-
2123 tors developed the framework for comparing ^{39}Ar to ^{40}Ar . Algorithms developed to calculate the
2124 relative volatility of argon isotopes, based on the extensive and detailed models available in the
2125 literature, predict that the volatility of ^{39}Ar relative to ^{40}Ar is 1.0015 ± 0.0001 , and that it stays
2126 constant within theoretical uncertainties in the range of temperatures practical for the distillation
2127 of argon (84 K to 100 K). The small volatility difference can be used to achieve active isotopic
2128 separation by using a cryogenic distillation system with thousands of equilibrium stages.

2129 Design of the Aria plant was optimized on the basis of high-precision numerical methods for
2130 estimating the isotopic separation of ^{39}Ar from ^{40}Ar . DarkSide Collaborators developed two in-
2131 dependent numerical codes, one based on the McCabe-Thiele method [75], and a second based on
2132 the Fenske-Underwood-Gilliland (FUG) method and its derivative, the Wynn-Underwood-Gilliland
2133 (WUG) method [76–78]. Calculations for the isotopic separation power of ^{39}Ar from ^{40}Ar and of the
2134 processing rate were performed with the custom codes, as well as with software routines supported
2135 by commercial chemical engineering CAD programs, such as Aspen [79].

2136 Fig. 36 illustrates the core of the process for isotopically separating ^{39}Ar from ^{40}Ar . The process
2137 consists mainly of two loops: the process loop where the argon is distilled and the ^{39}Ar is separated
2138 from the ^{40}Ar , and the refrigeration loop where nitrogen gas and liquid is used to evaporate and
2139 to condense the argon. Most of the heat is recovered, thanks to the compressor that pumps the
2140 nitrogen gas evaporated in the condenser to the reboiler and to the pumps that move the liquid
2141 nitrogen produced in the reboiler to the condenser, making the system as efficient as possible. In
2142 Fig. 36 all the sub-parts of the plant are represented:

- 2143 • Feed station, to filter and regulate the feed to the column;
- 2144 • Compressor station, to bottle the distillate at the bottom;
- 2145 • Vacuum system, to keep a good vacuum in the cold-box, in order to minimize the heat losses;
- 2146 • LN₂ storage;
- 2147 • Nitrogen condenser system, consisting of 4 Stirling cryo-refrigerators needed to re-condense the
2148 nitrogen, used in a closed loop.

2149 Seruci-I will consist of 28 modules of 12 m height, plus a top module (condenser) and a bottom
2150 module (reboiler).

2151 Calculations indicate that Seruci-I will be able to process UAr at a rate of O(1 t/d) removing all
2152 chemical impurities (including traces of N₂, O₂, and Kr) with a separation power better than 10³
2153 per pass. Additionally, Seruci-I can be used in a different mode of operations to test the isotopic
2154 separation of the argon, in order to further reduce the ^{39}Ar content in the UAr. The same models
2155 which have been used to calculate the chemical purification rate, have also been used to show that
2156 Seruci-I would be able to isotopically separate the UAr at a rate of 10 kg/d, while obtaining an
2157 ^{39}Ar depletion factor of 10 per pass.

2158 All modules for Seruci-I have already been built and passed a series of quality assurance checks.
2159 During the first check, the process column and all the service pipes were individually checked for
2160 leaks at room temperature. Then, the pipes were wrapped with super-insulation and everything
2161 was assembled into the cold box. The second check was a full module check, with an additional
2162 check done on the bottom reboiler module at 77 K. To date, all modules have passed both checks
2163 at room temperature and the bottom module has passed the final cold temperature check.

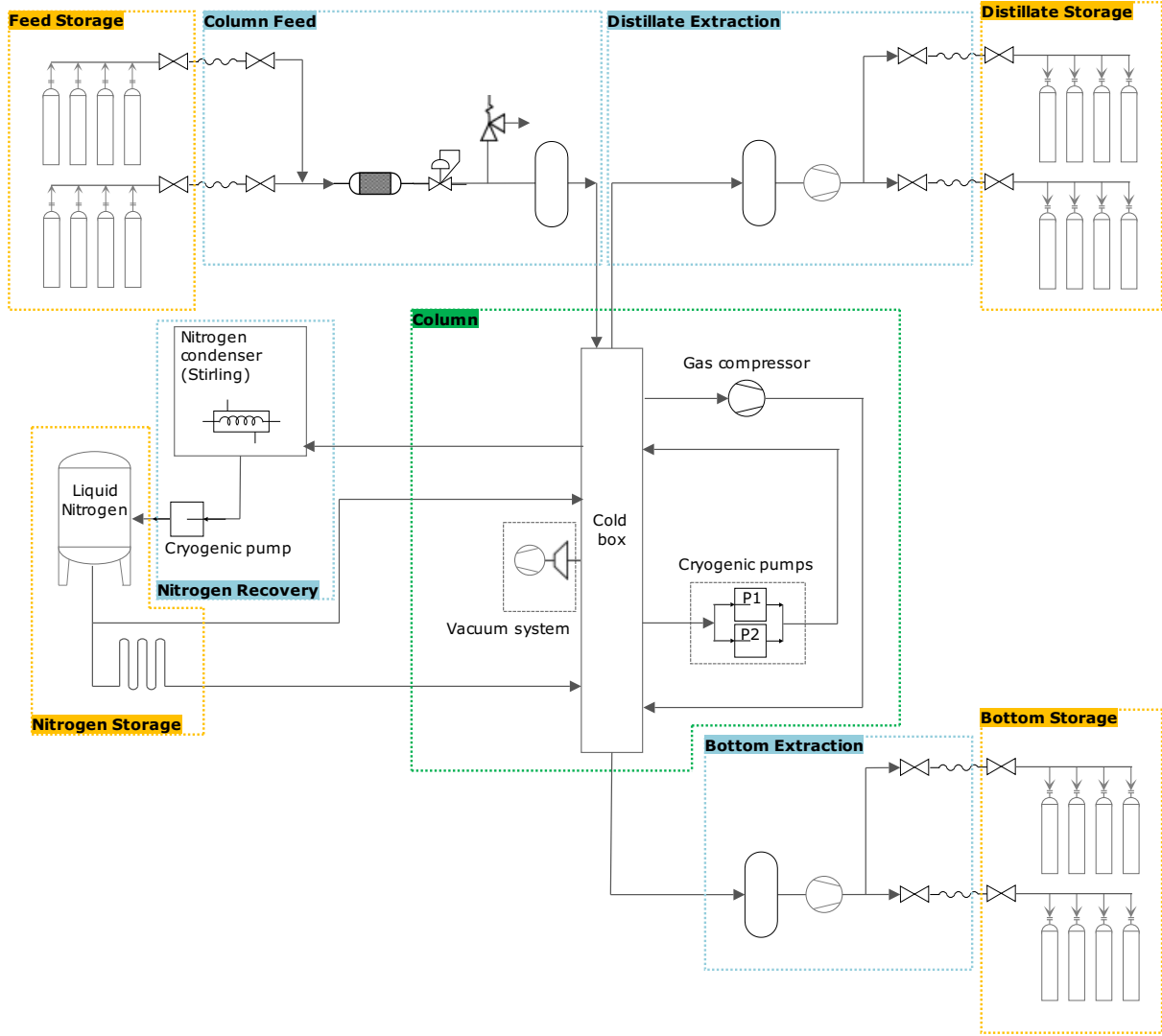


FIG. 36. Block diagram of the cryogenic system of the Aria plant.

Seruci-0 is a test column that is made with the Seruci-I top and bottom modules and a single central module. The goal of Seruci-0 is to confirm the proper operation of the three main components of the Seruci-I column, as well as to gain experience in operating the column on a smaller scale and to put in place the standard operating procedures. The three modules have been completely installed in a outdoor assembly hall at Nuraxi Figus, Italy, seen in Figure 37. During the last months, all the leak-check tests have been performed in order to guarantee the design tightness. Moreover, most of the plants have been installed and assembled in the area surrounding the column itself. Moreover, two concrete platforms were built: they currently host the liquid nitrogen dewar and the accessory plants, the cooling machine (chiller) and a control room to host people on shift and to organize the slow control. Test operations of Seruci-0 will start in summer of 2019.

Concerning the installation of Seruci-I, all the documents needed for the authorization request for installation were submitted in May 2018 to the competent authorities. During the first half of 2019, several meetings have been held, both with the fire brigade and with other local and county offices, entities and authorities. The authorization were eventually obtained. During 2018 a complete cleaning and preparation of the well at the Seruci site has been performed. A well-defined coring procedure was concluded in 2018. After the examination of the rocks samples, the design for

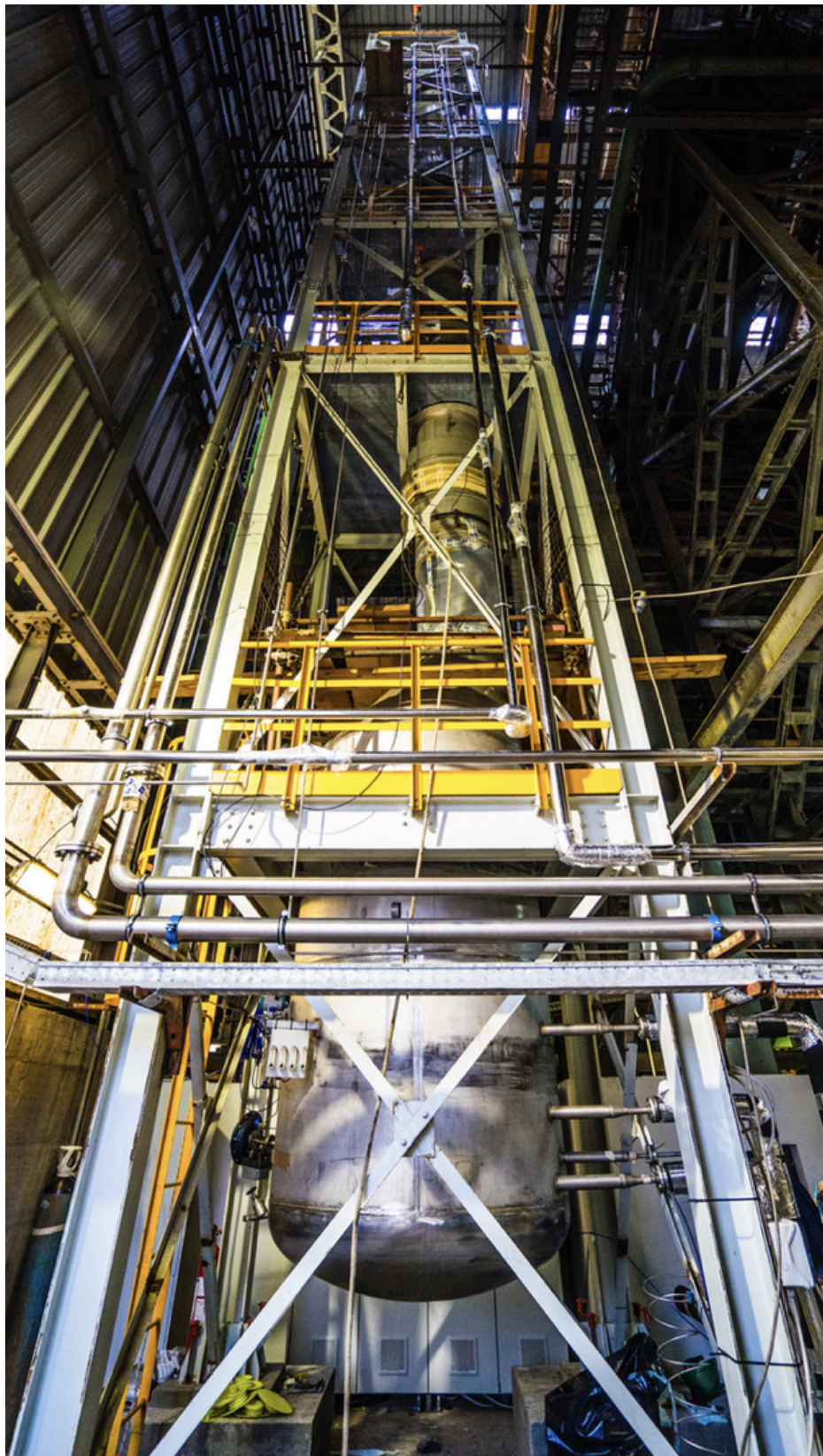


FIG. 37. The Seruci-0 cryogenic distillation column, installed in the *Laveria* building of Carbosulcis in Nuraxi Figus, Sardinia, Italy.

2180 the Seruci-I supporting structure was detailed. The tender was completed in Autumn 2018, and
2181 at the beginning of 2019 a carbon steel sample platform was delivered to the mine and installed in
2182 the Seruci well. The test was successful and was very useful in order to define all installation steps.
2183 The goal is to receive all of the platforms by the end of May 2019 and to install them inside the
2184 well by the end of 2019.

2185 **15.3. DArT**

2186 The DArT experiment will re-use the ArDM infrastructure with minimal modifications made
2187 and will consist of a radio-pure single-phase LAr detector with about one liter contained inside of
2188 its active volume. The DArT detector itself will be placed inside the middle of the ArDM vessel.
2189 DArT will be filled with argon to be tested in order to measure the content of ^{39}Ar . The detector
2190 will be readout by two cryogenic SiPMs each with a surface area of 1 cm^2 . The SiPMs and the
2191 readout electronics will come from the DS-20k production chain.

2192 The ArDM detector will act as an active veto against internal and external radiation. For this
2193 purpose, we are building a dedicated single phase setup with a new set of low-radioactive photo-
2194 multipliers (PMT). However, we will also retain the entire present double phase setup for later use,
2195 e.g. for measurements of large quantities of depleted argon.

2196 Extensive GEANT4-based simulations were performed using the Monte Carlo simulation package
2197 inherited from the DarkSide-50. These simulations show that DArT will achieve a sub-% measure-
2198 ment when operated inside the ArDM detector, for ^{39}Ar concentrations a factor of ten smaller
2199 than those of AAr, and in about a week of running. A 2% measurement could be made for ^{39}Ar
2200 concentrations as low as two orders of magnitude (statistical uncertainty only) smaller than those
2201 in AAr. This setup will also be useful to characterize the performance of Aria, which is expected
2202 to suppress the ^{39}Ar content by a factor of 10 per pass.

2203 A very important addition to the setup described above will consist of adding a 6 t lead belt
2204 about 140 cm tall around the ArDM vessel, at the mid-height position. This will suppress the
2205 impact of external photons that dominate the background budget and allow for the measurement
2206 of even larger ^{39}Ar depletion factors, corresponding to that of the UAr. If the depletion levels are
2207 those already measured in the past (i.e. of 1400), it will be possible, according to our simulations,
2208 to measure them with a 7% uncertainty in about a week of running. Upper limits can be set on
2209 depletion factors of order 25 200 (statistical uncertainty only), i.e. UAr with one distillation pass
2210 in Aria.

2211 The argon from Urania is expected to be available only after mid-2021. However, it is planned
2212 that after the run of DS-50 at LNGS, presumably at the end of 2019, its argon will be measured with
2213 DArT to cross-check the original measurement taken with DS-50 and to test the new setup. This
2214 DArT experiment is expected to become a useful facility within LSC for the years to come, since
2215 it will be needed to measure samples of the extracted argon from Urania over time. An Expression
2216 of Interest and a TDR were recently submitted to the LSC Directorate. Detector construction in
2217 all collaborating institutions has already started.

2218 **16. TECHNICAL DESIGN**

2219 **Viene descritto lo spazio richiesto presso le aree dei laboratori di superficie e sotter-
2220 ranei. In questa parte inoltre vengono descritte nel dettaglio tutte le scelte tecniche
2221 fatte, la loro implementazione e conseguentemente i sistemi e sottosistemi. In partico-
2222 lare si richiedono le specifiche funzionali e tecniche dell'infrastruttura, degli impianti
2223 e delle attrezzature in termini di:**

- 2224
 - 2225 • opere civili,
 - 2226 • impianti elettrici,
 - HVAC (riscaldamento, ventilazione e condizionamento dell'aria),

- acqua di raffreddamento/ deionizzata,
- aria compressa,
- attrezzature in pressione,
- sistemi da vuoto e criogenici,
- sistemi di sollevamento e trasporto,
- supervisione e controllo,
- sicurezza,
- IT,
- radioprotezione,
- meccanica,
- elettronica.

Si richiede di allegare i documenti tecnici al momento disponibili dalla Collaborazione (esempio: P&I, schede tecniche, elaborati tecnici, ...).

16.1. Installation Space and Services Needed

The complex installation procedures will be described in details in the following sections, here we give the general overall size of the needed spaces and services to be available in Hall C for a smooth, fast and successful construction of DS-20k.

- Total available surface in Hall C: 14m x 26m (or 2 x 14m x 14m). The surface needed for cryostat installation is 14m x 14m, and additional 14m x 14m for cryostat parts pre-assembly.
- Connections panels for construction phase (“quadri da cantiere”): Four 3-phases panels (32A each) for a simultaneous use of welding machines
- Mono-phase connection plugs of 230 VAC (16A each)
- Panel 24VAC for lighting inside the cryostat.
- Pressurized air: oil free, 6.3bar, 300 l/min with 3000 l/min peaks.
- Availability of Hall C cranes, in particular:
 - Use of the 20+20 tons arch crane for cryostat installation and cryostat roof operations
 - Use of the flat cranes for clean room mounting, test cryostat and TPC mounting operations.
 - Removal of the 5 ton cranes to optimize the operations of the 20+20 tons arch crane.
- Unloading Station availability in the TIR gallery.
- Gas detection systems (Oxygen detectors) and fire protection systems in Hall C.

16.2. Electrical Power for DS-20kOperation

A total power of 222 kW is needed for DS-20k:

- Cryostat (reference as in CERN NP04 cryostat) : 27KW
- DAQ (see Air Conditioning System)
- Ancillaries (Water Plant, Exhaust, Radon Abatement System, Lighting): 50KW
- Nitrogen Recovery System: 100KW (connection already there in Borex electric box)
- Air Conditioning System: 45KW

In addition a powerful UPS line is needed with a total capability of delivering 85 kW for the time needed to put in safe conditions all the delicate equipment:

- Cryostat and external cryogenics: 10KW
- DAQ: 45KW
- Gas Panel: 25KW
- Control System: 5KW

2271 **16.3. Nitrogen Argon and Water Services for DS-20kOperation**

2272 For cooling purposes the following water supply is needed:

- 2273 • Cryo-coolers and external cryogenics: TBD
- 2274 • Detector cryogenics: 1.0 mc/h
- 2275 • Air Conditioning System: 45KW (1.5 mc/h)
- 2276 • Fan-coil building : to be provided from LNGS services.
- 2277 • Radon Abatement System: 0.45 mc/h

2278 For Nitrogen and Argon the following is foreseen:

- 2279 • Use of the 20 m³ Nitrogen LINDE tank placed in the TIR gallery (currently in use by DarkSide-50 and Borexino)
- 2280 • Use of High Purity Nitrogen system
- 2281 • Use of the already existing Nitrogen recovery system. The system is ready to be used. It is instrumented with two Stirling engines, and with a distribution system for the recovered nitrogen in gaseous phase and for the disposal of the recovered liquid nitrogen in the 20 m³ LINDE tank.
- 2282 • Use of a 10 m³ buffer Argon tank for 5.0 Argon to be used for cryostat filling operations and to be located externally to Hall C, along the TIR gallery with a distribution line serving Hall C.

2289 **16.4. Underground Argon Storage and Transport**

- 2290 • The current DS-20k detector and cryogenic services layout implies the use of the TIR gallery for the storage of depleted underground argon (UAr) arriving from the ARIA plant in Sardinia.
- 2291 • The UAr transportation system and containers will also play the role of UAr recovery system, it is therefore foreseen that it is disposed in TIR gallery for the whole experiment lifetime.
- 2292 • The dimensions, volumes and operational working points of UAr shipping and storage system will be specified as soon as they will be defined.

2297 **16.5. IT Infrastructure**

2298 Data connection with external would need 2 fibers with 10 Gbps bandwidth (to be updated)

2299 **17. VALIDATION**

2300 **Sulla base della descrizione tecnica fornire i risultati degli studi, delle simulazioni e delle misure che dimostrano la congruità tecnica e la robustezza dell'implementazione proposta.**

2303 **18. INSTALLATION AND COMMISSIONING**

2304 **Descrizione delle differenti fasi e procedure dell'installazione e del commissioning delle infrastrutture e dell'apparato dettagliando la logistica (trasporti, procedure e stoccaggio) associata e le soluzioni trovate per risolvere le criticità.**

2305 In the following, we describe at first the main technical details of each key element of the entire DS-20k infrastructure in terms of services and detectors. At the end of the section, a step by step installation sequence proposal is described with the help of sketches of the making process of DS-20k

in LNGS Hall C. The planned activities in Hall C in terms of installation and commissioning are aimed at the construction of the cryostat and the attached cryogenics system, the construction of the metal structure supporting the cryogenics, the construction of the detector test radon free clean room, the assembly of the outer veto detector, and the final assembly and test of the inner TPC. The Cryostat, and its ancillary structures, is the main and larger element of the DS-20k infrastructure and will impact significantly Hall C environment in terms of space and needs especially during the installation and construction phase. As a consequence, particular focus is given to the cryostat technical description and installation sequence.

18.1. Cryostat Description and Construction

The design concept of this cryostat is based on the experience matured with the construction of similar vessels for the DUNE long baseline neutrino experiment. The adopted technique is the one of the LNG (Liquified Natural Gas) carriers and vessels, which has proven over many years its reliability. Main characteristics are the passive thermal insulation, and the inner wall with a corrugated layout designed to allow contraction and expansion of the main liquid volume. Two vessels of the same size as the one proposed here have been constructed at CERN. The experience gained there in the design, construction and operation will be fully translated to LNGS. The cryostat itself consists of two main parts: a warm and a cold structure. The main function of the warm structure is to deal with the hydrostatic pressure coming from the liquid. The internal cold structures insulate the vessel towards the outside and provide the containment of the liquid argon. All structural analysis are already available and updated with a new seismic analysis, taking into account the particular conditions of the Gran Sasso laboratory.

The warm structure. The warm structure is the outer vessel, which is kept at room temperature and will grant the structural integrity of the entire setup. It consists of an assembly of standard steel profiles. The overall outer dimensions are: width 11404 mm, length 11404 mm, height 10756 mm. The warm cryostat itself will be made of about 250t of hot rolled profiles and bolts. The steel structure consists of vertical beams alternated with a web of metal frames. Inside the steel structure, a skin of stainless steel plates is welded, such as to provide a gas barrier to the outside. This mechanical structure sits on top of the Hall C concrete floor. The top of the cryostat will be accessible for installation of the active inner detectors (TPC and veto counter), the electrical signal feedthroughs, the detector supports and other cryogenics services. The structural beams load-bearing elements consist of IPE V 600 and IPE O 270 standard profiles. Stainless steel plates, 10 mm thick, are welded to the web interlink structure to create a gas containment barrier to the inside and ensure even better support for the passive thermal insulation. The cryostat body will be fully electrically insulated from the building ground.

Insulation and inner membrane. The insulation consists of two layers of foam supported by plywood plates. The inner membrane is made out of stainless steel 1.2 mm thick. The main characteristic of this primary membrane, in contact with the cryogenic liquid, is to be capable to expand and shrink as a function of the temperature, thanks to a special corrugation configuration, which makes it acting like a bi-dimensional spring. The insulation consists of two layers of a foam especially developed for this purpose supported by plywood plates. The first insulation layer is attached to the 10 mm-thick outer Stainless Steel (SS) skin. The foam material is expanded polyurethane with a density of 90 kg/m³. Between the two layers of insulation there is a secondary containment system made out of a thin layer of a triplex Aluminum based fabric. In contact with the foam, on the cold side, there is the primary membrane made out of stainless steel (304L) 1.2 mm thick. The overall thickness of the insulation and membranes is 800mm. Thermal fluxes are to be controlled so that the unitary value calculated in unidirectional model is below 6.3 W/m² on the wall and floor in contact with the liquid. The tertiary membrane made of SS 10mm plate of the type 304L will account for 50t of material. The insulation foam will account for 35 t of polyurethane with an addition of about 20 t of plywood. The inner primary corrugated membrane will account for 7 t of SS 304L, for which the raw material batch can be selected according to the

2360 required radioactive contamination levels.

2361 **Cryostat construction and installation activities.** To ease the installation, it is proposed
2362 to have a square opening on the roof of the cryostat with dimensions of 4250×4250 mm². A top
2363 cap will close this opening with the inner detectors hanging from it. This top cap will host all the
2364 penetration necessary to support the active detector, all electrical and signal feedthroughs and the
2365 cryogenics services. Four large size penetration will be placed on the four corners of the roof of the
2366 cryostat with the purpose of allowing access to the inside, to bring clean air inside the vessel during
2367 installation and the necessary cryogenics service for the LAr bath. Particular attention will be
2368 given in all steps of the construction work to minimize the radio contamination of the materials, in
2369 particular for the the SS primary membrane closer to the detector. Cryostat installation sequence
2370 steps are described at the end of this section.

2371 **Cryostat construction schedule.** The thermal insulation and inner membrane are based on
2372 the LNG technology developed by the firm GTT (Gaztransport & Technigaz) and today imple-
2373 mented in about 80 % of all LNG transport ships. This is a proprietary technology, well protected
2374 by IP regulations. GTT is not directly constructing LNG carries, but has defined a network of
2375 firms which have the permission to use their technology and IP. In this framework GTT would do
2376 the full engineering of the cold vessel. In 2015 CERN has managed to establish a collaboration
2377 agreement with GTT. The full engineering design is part of the current integration work performed
2378 by the collaboration and driven by CERN. For the in situ assembly of the warm structure, previous
2379 experience shows that, once the modules are available, it takes 16 weeks for the full process. The
2380 assembly of the cold structure will be done in 35 weeks. For the moment we do not add a precise
2381 operation time to each step which are described in the following. This until we understand the
2382 entire logistic and the lab requirements.

2383 18.2. Metallic Structure

2384 The metallic structure proposed here will be used to allocate the Cryogenics System and part
2385 of the electronics for the DS-20k TPC and Veto detectors. The structure will be connected to the
2386 roof of the warm outer cryostat, where equipments for the calibration, the safety devices, and TPC
2387 leveling system will be also located. The construction of the metallic structure will begin once the
2388 warm outer structure of the cryostat will be finalized.

2389 18.3. Cryogenic System

2390 A cryogenic system has to be built in order to serve the DS-20k experiment cryostat filled
2391 with Atmospheric Argon (AAr). This system must be able to efficiently purify, recirculate and
2392 maintain 682 tons of AAr. It will include several subsystems: the liquid argon handling system, the
2393 liquid nitrogen reserve system, the purification system, the calibration source handling system, the
2394 condenser box, the gas circulation pump, and the near detector heat exchange system. The liquid
2395 nitrogen reverse system is basically a liquid nitrogen tank, which is connected to AAr cryogenic
2396 system, to provide its cooling source.

2397 The atmospheric argon cryogenic system serving the cryostat will be installed in LNGS Hall- C
2398 once the cryostat and the DS-20k metallic structure construction will be finalized. A second and
2399 separate cryogenic system to purify and recirculate the depleted Argon filling the TPC detector
2400 inner volume will also be installed on the roof of the warm structure.

2401 18.4. The Radon Free Clean Room

2402 A large radon free clean room close to the main cryostat is needed in order to perform final
2403 assembly and test of the acrylic TPC sealed vessel in a radon free environment. These operations

2404 includes TPC top and bottom acrylic panels bonding with lateral TPC panels, acrylic annealing,
2405 final TPC supporting structure assembly with PDM plates (instrumented with SiPMs) positioned
2406 and fixed on acrylic vessel top and bottom, and cryogenic test of the full inner TPC detector
2407 before insertion in its final position inside the outer veto in the cryostat. In order to perform this
2408 operations, a large test cryostat sufficient to host the full TPC, will be placed in the radon free clean
2409 room. The radon free clean room dimensions are designed to allow the handling and movement of
2410 the TPC vessel parts. Inside the clean room, a crane is foreseen. It will be possible to open the
2411 roof of the clean room for hanging to main Hall C crane the TPC and put it in its final position in
2412 the cryostat. The radon free clean room construction can start once the cryostat warm structure
2413 is completed.

2414 **18.5. TPC and Veto Detector Assembly and Installation**

2415 Once the radon free clean room will be built and ready to use, TPC final assembly and cryogenic
2416 test in the test cryostat can start. In parallel, once the cryostat inner membrane deposition,
2417 welding and testing is completed, the veto detector acrylic panel assembly and positioning inside
2418 the cryostat will start. A temporary floor inside the cryostat will be put in place to support veto
2419 assembly operations. When the veto detector bottom and lateral walls will be ready to host the
2420 inner detector, the TPC will be put in its final position through the top roof cryostat opening before
2421 the completion and closing of the veto detector top part. Once this is achieved the full veto and
2422 TPC detectors system will be hanged to the cryostat top cap and the false floor and veto supports
2423 removed. Veto and TPC detectors assembly and integration operations inside the cryostat will
2424 require the use of a temporary cleanroom structure on the cryostat roof opening, to allow working
2425 in a radon-free environment.

2426 **18.6. DS-20kProposed Installation Sequence**

2427 We provide here below a set of pictures which explain the sequence of main operation steps in the
2428 LNGS Hall C. For each step we describe the key operations impacting Hall C environment during
2429 the DS-20k installation phase.

- 2430 1. Floor preparation: install the survey network, survey the floor planarity, mark the floor for
2431 the imprint of the cryostat, position the shims and the rubber pads.
- 2432 2. Floor structure integration (I): 3 pre-assembled modules will be positioned on dedicated
2433 support structure.
- 2434 3. Floor structure integration (II): additional 5 pre-assembled elements will be positioned and
2435 interconnected. The metal plates will then be welded together, for gas tightness and a He
2436 leak test will be done to qualify the welds.
- 2437 4. Position the floor element: The entire floor quadrant will then be positioned on the prepared
2438 shims, after adding a layer of G10 electrical isolation. At this point a survey of the flatness
2439 will be done and if needed the process will be iterated.
- 2440 5. Second quadrant preparation: Similar activity as for 2.2 and 2.3. This element is the first
2441 wall.
- 2442 6. First wall installation (I) : first the wall structure will be rotated upside down. Stabilizers
2443 will be installed on the cavern wall.
- 2444 7. First wall installation (II) : With main crane the wall will be positioned vertically, bolted to
2445 the floor and bolted to the temporary wall stabilizers. Each of these steps requires detailed
2446 survey work to ensure perpendicularity.
- 2447 8. Second wall integration: same activity as in 2.3 and 2.3.
- 2448 9. Second wall installation: Ration and vertical installation. Stabilizers will be used to secure
2449 the vertical stability after bolting to the floor structure.

- 2450 10. Positioning of the stabilizers on the corners: this is to allow wall 3 and 4 to be positioned
2451 vertically.
- 2452 11. Third wall preparation: Same activity as for 2.2 and 2.3. This time the work is done on the
2453 left to ease the manipulations necessary for the vertical installation.
- 2454 12. Third wall installation: vertical positioning and bolting connection to the floor and to the
2455 stabilizers. Survey activity will follow and correct the process.
- 2456 13. Last wall installation: same process as 2.11 and 2.12. This time done on the right side.
- 2457 14. Corner elements installation: one by one the four corners pre-assembled will be installed in
2458 place. At this point geometrical corrections will be done with shims, if needed. Once done,
2459 all stabilizers will be removed.
- 2460 15. Preparation of the roof structure: Several preassembled components of the roof will be inter-
2461 connected by bolts and He tested after welding.
- 2462 16. Roof positioning : Then the roof is positioned. The critical step is the rotation upside down
2463 of the roof before positioning it.
- 2464 17. Metallic structure and Cold structure assembly : the metallic structure which will hold the
2465 cryogenics will be installed, with all stairs and egresses. The necessary pipes, which will bring
2466 air for the future radon-free clean room, will be installed on the wall of the cavern. The roof
2467 will be secured with a floor and hand rails to ease access, and a stair system will allow to
2468 enter the interior of the cryostat. The cold insulation and membrane from GTT can start to
2469 be installed. This will be a several months process.
- 2470 18. Detector clean room assembly : on the right side, starting with metallic structures and later
2471 the walls and the doors. This includes the material and personnel SAS.
- 2472 19. Test cryostat : Once the clean room is operational, the test cryostat is positioned and ready
2473 to receive the DS-20k detector parts: the inner TPC and the outer neutron veto acrylic
2474 structures.
- 2475 20. The acrylic TPC vessel arrives to the clean room : ready to be inserted in the test cryostat
2476 once the active TPC elements are inserted. In the mean time on top of the main cryostat a
2477 temporary cleanroom structure is mounted, to allow working in a radon-free environment.
- 2478 21. Ready TPC inserted in the test cryostat : once this is done, the TPC can be tested and
2479 qualified at cold, before insertion in the main cryostat.
- 2480 22. The TPC tested is inserted inside the main cryostat : after the veto counter bottom and
2481 lateral walls are in position and ready to accomodate TPC inside.
- 2482 23. All detector components are inserted and positioned : in particular the veto counter top and
2483 all active probes. All services and cables are routed and the front-end electronics is first
2484 tested in situ
- 2485 24. The cryostat top cap is inserted and the detector is closed, ready for cryogenic commissioning.
- 2486 25. DS-20k is ready for commissioning.

2487 **19. HEALTH, SAFETY AND ENVIRONMENTAL ISSUES**

2488 **Vengono presentati e discussi i punti specifici riguardanti la salute, sicurezza e am-
2489 biente nella PRA (Quantity Risk Assessment) che include ERA (Environmental Risk
2490 Assessment) e il OHRA (Occupational Health Risk Assessment). Descrivere inoltre:**

- 2491 • **la tipologia e la quantità delle sostanze chimiche che saranno utilizzate nel corso
2492 delle fasi dell'esperimento includendo le modalità di utilizzo, le schede tecniche
2493 e di sicurezza,**
- 2494 • **la tipologia, la quantità e le modalità di utilizzo dei materiali**
- 2495 • **tipologia e quantità di rifiuti che saranno prodotti nel corso delle fasi dell'esperimento,
2496 al fine di verificare se soddisfano i requisiti di sicurezza e antincendio**

2497 A full PRA analysis is in preparation with the help and support of an external company, and
2498 will be attached to the TDR when ready.

20. RADIATION PROTECTION ISSUES

2500 **Vengono presentati e discussi i punti specifici che riguardano la radioprotezione
 2501 presentando i risultati delle eventuali simulazioni delle radiazioni e la descrizione dei
 2502 sistemi di rivelazione e delle schermature. Si richiede di integrare queste considerazioni
 2503 con le valutazioni ambientali, operative e di sicurezza già validate e da personale
 2504 esperto.**

2505 Detailed simulation results on the shieldings and on the active devices of the DarkSide-20k
 2506 detector and infrastructure layout including calibration system and source storing, will be added
 2507 as soon as they will be available.

2508 Detailed reports and operative procedures will be developed in accordance with the European
 2509 and Italian regulation and LNGS rules in matter of radio protection (D.Lgs. 230/95 and further
 2510 modifications).

21. PROJECT MANAGEMENT

2512 **Si richiede di descrivere la strategia di progetto attraverso gli strumenti di Project
 2513 Management come per esempio il Project Management Plan e si richiede inoltre di
 2514 presentare uno schema riassuntivo sulle tipologie delle gare d'appalto necessarie per
 2515 la realizzazione dell'Esperimento (LNGS tender, INFN tender, European tender) in-
 2516 cludendo tempi e risorse stimate per il suo espletamento.**

2517 A detailed Project Execution Plan, prepared for the NSF Mid Scale funding Request in May
 2518 is attached to this document. In that document all the project organization and management
 2519 tools are described as well as the current Work Breakdown Structure and gantt chart. Details on
 2520 the funding scheme and institution responsibility and cost sharing is also reported there. We refer
 2521 to the attached document for all aspect mentioned before. In the following only relevant additions
 2522 are reported:

- 2523 1. Updated general Gantt chart and relevant discussions
 - 2524 2. Compilation of the risk register (example below from LNGS template
 - 2525 3. tbc
-

- 2526 [1] CERN, CERN Yell. Rep. Mon. (2017).
- 2527 [2] P. A. Amaudruz et al. (The DEAP-3600 Collaboration), Phys. Rev. Lett. **121**, 071801 (2018).
- 2528 [3] R. Ajaj et al., arXiv:1902.04048v1 (2019).
- 2529 [4] P. Agnes et al. (The DarkSide Collaboration), Phys. Lett. B **743**, 456 (2015).
- 2530 [5] P. Agnes et al. (The DarkSide Collaboration), Phys. Rev. D **93**, 081101 (2016).
- 2531 [6] P. Agnes et al. (The DarkSide Collaboration), Phys. Rev. D **98**, 102006 (2018).
- 2532 [7] P. Agnes et al. (The DarkSide Collaboration), Phys. Rev. Lett. **121**, 081307 (2018).
- 2533 [8] P. Agnes et al. (The DarkSide Collaboration), Phys. Rev. Lett. **121**, 111303 (2018).
- 2534 [9] B. Abi et al. (The DUNE Collaboration), arXiv:1706.07081v2 (2017).
- 2535 [10] R. Acciarri et al. (The DUNE Collaboration), arXiv:1601.05471v1 (2016).
- 2536 [11] Heraeus Deutschland GmbH & CO. Kg, *CLEVIOS™ PEDOT* (2019).
- 2537 [12] G. Angloher et al. (The CRESST Collaboration), Eur. Phys. J. C **72**, 1971 (2012).
- 2538 [13] D. S. Akerib et al. (The LUX Collaboration), Phys. Rev. Lett. **118**, 021303 (2017).
- 2539 [14] X. Cui et al. (The PandaX-II Collaboration), Phys. Rev. Lett. **119**, 181302 (2017).
- 2540 [15] E. Aprile et al. (The XENON Collaboration), Phys. Rev. Lett. **121**, 111302 (2018).
- 2541 [16] T. A. Collaboration, *CERN Doc. Serv.* (2018).
- 2542 [17] H. Nelson (For The LZ Collaboration), Presentation at DM 2014 (2014).
- 2543 [18] V. A. Kudryavtsev (The LZ Collaboration), AIP Conf. Proc. **1672**, 060003 (2015).
- 2544 [19] E. Aprile (For The XENON Collaboration), Presentation at LNGS Sci. Comm. Apr. 2015 (2015).
- 2545 [20] M. G. Boulay (For the DarkSide Collaboration), Presentation at New Ideas DM 2017 (2017).
- 2546 [21] R. Agnese et al. (The SuperCDMS Collaboration), Phys. Rev. D **95**, 215 (2017).

Risk Register

Project name: Common project risks

ID	Date raised	Risk description	Likelihood of the risk occurring	Impact if the risk occurs	Severity Rating based on impact & likelihood.	Owner Person who will manage the risk.	Mitigating action Actions to mitigate the risk e.g. reduce the likelihood.
1	[enter date]	Project purpose and need is not well-defined.	Medium	High	High	Project Sponsor	Complete a business case if not already provided and ensure purpose is well defined on Project Charter and PID.
2	[enter date]	Project design and deliverable definition is incomplete.	Low	High	High	Project Sponsor	Define the scope in detail via design workshops with input from subject matter experts.
3	[enter date]	Project schedule is not clearly defined or understood	Low	Medium	Medium	Project Manager	Hold scheduling workshops with the project team so they understand the plan and likelihood fo missed tasks is reduced.

FIG. 38. Preliminary Risk Registry Table

- 2547 [22] J. Billard, E. Figueroa-Feliciano, and L. Strigari, *Phys. Rev. D* **89**, 023524 (2014).
 2548 [23] D. Abercrombie et al., *arXiv:1507.00966v1* (2015).
 2549 [24] C. E. Aalseth et al. (The DarkSide Collaboration), *Eur. Phys. J. Plus* **133**, 131 (2018).
 2550 [25] M. D'Incecco et al., *IEEE Trans. Nucl. Sci.* **65**, 1005 (2018).
 2551 [26] M. D'Incecco et al., *IEEE Trans. Nucl. Sci.* **65**, 591 (2018).
 2552 [27] D. Franco et al., *JCAP* **2016**, 017 (2016).
 2553 [28] J. Evans et al., *Phys. Rev. D* **95**, 1180 (2017).
 2554 [29] M. Honda, T. Kajita, K. Kasahara, and S. Midorikawa, *Phys. Rev. D* **83**, 123001 (2011).
 2555 [30] G. D. Barr, S. Robbins, T. K. Gaisser, and T. Stanev, *Phys. Rev. D* **74**, 323 (2006).
 2556 [31] R. Tayloe, *JINST* **13**, C04005 (2018).
 2557 [32] D. Akimov et al. (The COHERENT Collaboration), *Science* **357**, 1123 (2017).
 2558 [33] H. Cao et al. (The SCENE Collaboration), *Phys. Rev. D* **91**, 092007 (2015).
 2559 [34] T. Alexander et al. (The SCENE Collaboration), *Phys. Rev. D* **88**, 092006 (2013).
 2560 [35] P. Agnes et al. (The ARIS Collaboration), *Phys. Rev. D* **97**, 10 (2018).
 2561 [36] J. Dobson (For the LZ Collaboration), Presentation at DM 2018 (2018).
 2562 [37] I. Ostrovskiy et al., *IEEE Trans. Nucl. Sci.* **62**, 1825 (2015).
 2563 [38] S. Cebrián et al. (The NEXT Collaboration), *JINST* **12**, T08003 (2017).
 2564 [39] J. J. Gómez Cadenas, J. M. Benlloch-Rodriguez, and P. Ferrario, *Spectrochim. Acta B* **118**, 6 (2016).
 2565 [40] S. Cebrián et al., *JINST* **10**, P05006 (2015).
 2566 [41] M. G. Boulay (For The DEAP Collaboration), *J. Phys. Conf. Ser.* **375**, 012027 (2012).
 2567 [42] C. M. Nantais, B. T. Cleveland, and M. G. Boulay, *AIP Conf. Proc.* pp. 185–188 (2013).
 2568 [43] P. Agnes et al. (The DarkSide Collaboration), *JINST* **11**, P12007 (2016).
 2569 [44] P. Agnes et al. (The DarkSide collaboration), *JINST* **11**, P03016 (2016).
 2570 [45] P. Agnes (Université Paris Diderot), Ph.D. thesis, Université Paris Diderot (2016), URL <https://tel.archives-ouvertes.fr/tel-01497505v1>.
 2571 [46] P. Agnes et al. (The DarkSide Collaboration), *JINST* **12**, P12011 (2017).
 2572 [47] P. Agnes et al. (The DarkSide Collaboration), *JINST* **12**, P01021 (2017).
 2573 [48] P. Agnes et al. (The DarkSide Collaboration), *JINST* **12**, P10015 (2017).
 2574 [49] P. Agnes et al. (The DarkSide Collaboration), *JINST* **12**, T12004 (2017).
 2575 [50] P. Agnes et al. (The DarkSide Collaboration), *Nucl. Inst. Meth. A* **904**, 23 (2018).
 2576 [51] W. J. Willis and V. Radeka, *Nucl. Inst. Meth.* **120**, 221 (1974).
 2577 [52] V. Radeka, *IEEE Trans. Nucl. Sci.* **21**, 51 (1974).
 2578 [53] V. Radeka and S. Rescia, *Nucl. Inst. Meth. A* **265**, 228 (1988).
 2579 [54] R. L. Chase, C. de La Taille, S. Rescia, and N. Seguin, *Nucl. Inst. Meth. A* **330**, 228 (1993).

- 2581 [55] R. L. Chase and S. Rescia, *IEEE Trans. Nucl. Sci.* **44**, 1028 (1997).
2582 [56] W. Ootani, *Nucl. Inst. Meth. A* **732**, 146 (2013).
2583 [57] P. W. Cattaneo et al., *Nucl. Inst. Meth. A* **828**, 191 (2016).
2584 [58] I. Ostrovskiy (The University of Alabama), (2012).
2585 [59] A. S. Barabash et al., *Nucl. Inst. Meth. A* **868**, 98 (2017).
2586 [60] L. Mapelli et al., *CERN EDMS* **1837551** (2017).
2587 [61] F. A. Lindemann, *Phil. Mag.* **38**, 173 (1919).
2588 [62] H. C. Urey, F. G. Brickwedde, and G. M. Murphy, *Phys. Rev.* **40**, 1 (1932).
2589 [63] J. de Boer and R. J. Lunbeck, *Physica* **14**, 520 (1948).
2590 [64] J. de Boer, *Physica* **14**, 139 (1948).
2591 [65] J. de Boer and A. Michels, *Physica* **6**, 97 (1939).
2592 [66] J. Bigeleisen, *J. Chem. Phys.* **34**, 1485 (1961).
2593 [67] G. Boato, G. Scoles, and M. E. Vallauri, *Nuovo Cim.* **23**, 1041 (1962).
2594 [68] G. Boato, G. Casanova, G. Scoles, and M. E. Vallauri, *Nuovo Cim.* **20**, 87 (1961).
2595 [69] G. Boato, G. Scoles, and M. E. Vallauri, *Nuovo Cim.* **14**, 735 (1959).
2596 [70] G. Casanova, A. Levi, and N. Terzi, *Physica* **30**, 937 (1964).
2597 [71] C. Casanova, R. Fieschi, and N. Terzi, *Nuovo Cim.* **18**, 837 (1960).
2598 [72] R. Fieschi and N. Terzi, *Physica* **27**, 453 (1961).
2599 [73] J. N. Canongia Lopes, A. A. H. Pádua, L. P. N. Rebelo, and J. Bigeleisen, *J. Chem. Phys.* **118**, 5028
2600 (2003).
2601 [74] J. C. G. Calado, F. A. Dias, J. N. C. Lopes, and L. P. N. Rebelo, *J. Phys. Chem. B* **104**, 8735 (2000).
2602 [75] W. L. McCabe and E. W. Thiele, *Ind. Eng. Chem.* **17**, 605 (1925).
2603 [76] A. J. V. Underwood, *Ind. Eng. Chem.* **41**, 2844 (1949).
2604 [77] E. R. Gilliland, *Ind. Eng. Chem.* **32**, 1220 (1940).
2605 [78] M. R. Fenske, *Ind. Eng. Chem.* **24**, 482 (1932).
2606 [79] Aspen Technology, Inc., *Aspen Plus®* (2015).